Vortices in Hyperbolic Funnels as Aeration Systems

A Numerical Study

Teja Donepudi

Master of Science Thesis

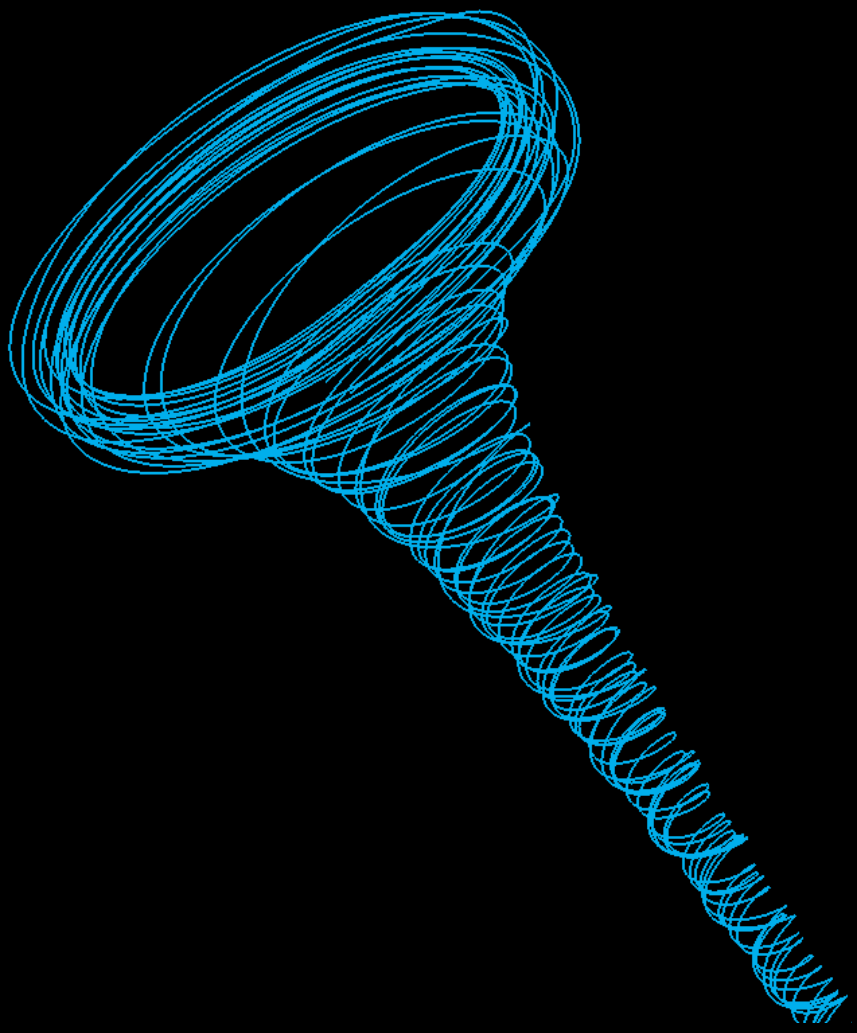

TU Delft Delft University of Technology

Energy, Flow and Process Technology

Vortices in Hyperbolic Funnels as Aeration Systems

A Numerical Study

by

Teja Donepudi
Student number: 5008247

in partial fulfillment of the requirements for the degree of

Master of Science
in Mechanical Engineering

at the Delft University of Technology,
to be defended publicly on Friday August 27, 2021 at 14:00 hrs.

Daily supervisor:	M. V. van de Griend, Wetsus
Thesis Committee:	Dr. R. Pecnik, TU Delft, Chairman
	Dr. E. C. Fuchs, Wetsus
	Dr. M. J. B. M. Pourquie, TU Delft
	Prof. Dr. J. Woisetschläger, TU Graz

Faculty of Mechanical, Maritime and Materials Engineering (3mE) · Delft University of Technology

The work in this thesis was supported by Wetsus, European Centre of Excellence for Sustainable Water Technology, The Netherlands. Their cooperation is hereby gratefully acknowledged.

‘Endarō mahānubhāvulu andarīki vandanamulu’

(There are so many great people! My salutations to all of them!)

Saint Tyagaraja
(1767 - 1847)

Acknowledgements

The nine months duration of this thesis has been the most challenging period of my life so far. I am genuinely humbled by the support I have received through the ups and downs of this journey.

Firstly, I would like to express my sincere gratitude to my supervisors Dr. Pecnik and Dr. Fuchs, for their continuous guidance and support throughout this project. It was a real privilege to work under both of them. The questions posed by Dr. Pecnik during our review meetings have helped me to push the limits of my thinking and analyse the physical mechanisms better. It was this satisfaction that kept me motivated every single day. I will forever be grateful to Dr. Fuchs for giving me this opportunity to work as a thesis student at Wetsus and providing me with a platform to make my humble contribution to the ongoing research.

I admire Maarten's method of reasoning everything from fundamentals. Our discussions have helped me realise how important it is to get the basics right. Time and again, I have benefited from the comprehensive explanations by Dr. Agostinho, which has helped me to understand the system better. I appreciate the inputs given by Esther to help me understand the experimental data.

I am very thankful to Stephan for being kind enough to answer all my queries regarding meshing in a simple yet insightful manner. Special thanks to Dr. Pourquie for helping me to get acquainted with the cluster. His depth of understanding of CFD is something that truly inspires me. My interest in the field of fluid sciences was sparked by Dr. Tam. His ability to teach seemingly complex concepts with such ease and elegance is truly spellbinding.

I would also like to acknowledge the contributions of Dr. Yadav and Dr. Maniyeri from my undergraduate studies. Their passion for science has inspired me to pursue higher studies. I am humbled by the constant support and guidance I have received from Bhargav, not just on the academic side of things but also on a personal front.

No words will ever be able to describe the contribution and sacrifices my parents have been making to turn every wish of mine into a reality. It is due to them that I have had the privilege to pursue a masters. And to all my friends here in Delft and back in India, I will forever be indebted to all of you for sustaining me. Many others have helped me reach this far in life. Today, I bow my head in respect to all of you.

Teja Donepudi
August 27, 2021

Abstract

Experiments to characterise vortices in hyperbolic shaped funnels are being conducted at the Water Application Centre (WAC) in Wetsus. These have demonstrated their higher gas transfer rates in comparison to the conventional aeration systems presently in use. Depending on the imposed flow conditions, different regimes of vortices are formed, among which the *Twisted* vortical structure is observed to have the highest gas dissolution rates. This has probed several questions on the physical mechanisms responsible on both micro-and macroscopic scales. The present research aims to numerically analyse the flow field organisation in these vortices to reason the observed high gas transfer rates using Computational Fluid Dynamics (CFD).

Transient simulations were performed on a three-dimensional radially structured hexahedral mesh. Multi-phase modelling was done using the Euler-Euler approach-based Volume-of-Fluid (VOF) method, while the turbulent flow was modelled using Shear Stress Transport (SST) based on k - ω equations with curvature correction. The choice of boundary conditions and their location is crucial for forming a stable vortex in the hyperbolic funnels. The position of the air-water interface from experimental results was used to validate the obtained numerical results. Two regimes of the vortex, namely the *Twisted* and *Straight* vortical structures, were evaluated for their gas transfer capabilities in terms of Hydraulic Retention Time (HRT), interfacial area and mixing in the bulk.

Instabilities arise in the secondary flow field of these vortical structures analogous to the Taylor-vortices that develop in the well known Taylor-Couette flow systems. In hyperbolic funnels, these instabilities aid in advecting the bulk of liquid to the air-water interfacial region and also enhance mixing within the bulk of water. The former enhances the gas transfer rates while the latter promotes uniform mixing. The strength of these instabilities is qualitatively analysed in terms of average vorticity per unit mass of water. This is found to be higher in the *Twisted* regime in comparison to other regimes. This is augmented by high air-water interfacial area making this regime possess superior gas transfer rates.

Although the gas transfer rates are high, water exiting the funnel is undersaturated at the given operating conditions. In order to further enhance the amount of gas dissolved few possibilities are qualitatively discussed at the end of this study.

Keywords: *Aeration systems, Hyperbolic funnels, Vortex flows, Computational fluid dynamics, Multi-phase simulations, Turbulence modelling, Instabilities.*

Nomenclature

Abbreviations

CFD	Computational Fluid Dynamics
DNS	Direct Numerical Simulations
DO	Dissolved Oxygen
FSV	Free Surface Vortex
HRT	Hydraulic Retention Time
KE	Kinetic Energy
LES	Large Eddy Simulations
RANS	Reynolds Averaged Navier Stokes Equations
RGT	Rate of Gas Transfer
RNG	Re-Normalisation Group
SAE	Standard Aeration Efficiency
SST	Shear Stress Transport
TC	Taylor-Couette
UDF	User Defined Function
VOF	Volume of Fluid

Physical constants

g	Acceleration due to gravity	$9.81\,\mathrm{m\,s^{-2}}$

Variables

a	Interfacial area
C	Closed curve
c	Species concentration
D	Diffusion coefficient
d	Annular width
H	Henry's constant
K	Mass transfer coefficient
k	Turbulent kinetic energy

m	Mass
P	Pressure
R	Resistance
s	Strain rate tensor
t	Time
u	Velocity component
V	Volume

Greek variables

δ	Dirac delta function
ϵ	Turbulent dissipation rate
Γ	Circulation
μ	Dynamic viscosity
∇	Nabla operator
ν	Kinetic viscosity
ω	Specific dissipation rate
ϕ	Volume fraction
ρ	Density
Σ	Sigma operator
σ	Molecular viscosity stress
τ	Sub-grid scale reynolds stress

Superscripts

$'$	Perturbation
$-$	Averaged value
$\cdot$	Time rate
$\sim$	Filtered value
$\star$	Equilibrium condition
$\wedge$	Unit vector

Vectors

$\mathbf{\Omega}$	Vorticity
$\mathbf{u}$	Velocity

Subscripts

(i, j, k)	Mutually perpendicular cartesian directions
inf	Far field region
θ	Tangential component
avg	Average
c	Air-core
exp	Experiment
i	Inner
int	Interface
k	Cell number

lam	Laminar
o	Outer
out	Outlet
s	Static
sim	Simulation
t	Turbulent
G	Gas phase
L	Liquid phase
r	Radial component
z	Axial component

Non dimensional numbers

η	Radius ratio
θ	Non-dimensional time
ξ	Non-dimensional height
ζ	Aspect ratio
a	Rotation ratio
Nu	Nusselt number
Re	Reynolds number
Ta	Taylor number
Ro	Rossby number

Table of Contents

List of Figures

List of Tables

Chapter 1

Introduction

1-1 Background

Viktor Schauberger, an Austrian naturalist and inventor, based his inventions on observations from nature. He was also referred to as the *Water Wizard* in his ability to mimic nature. One of his many nature-inspired works were the experiments conducted in 1952 to separate hydrophobic materials by creating a *vortex* flow in pipes made of different materials and designs. During these studies, it was observed that frictional force on the fluid was least when spiralling, and conical pipes were used [21].

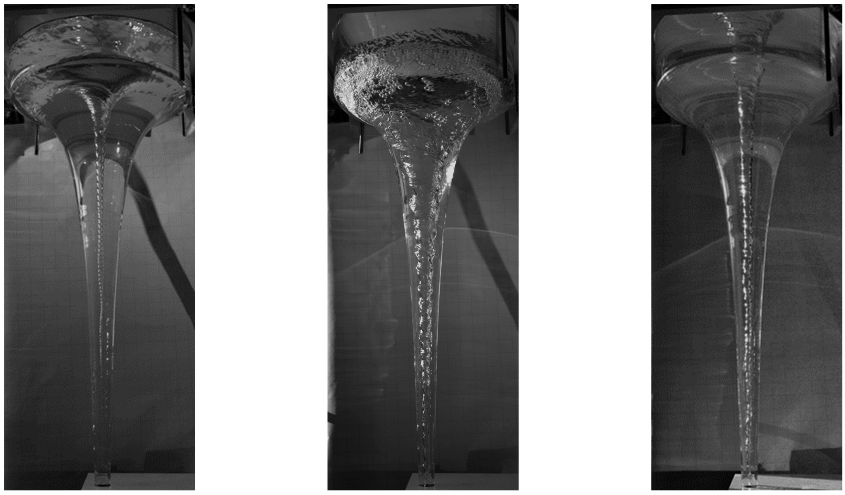

(a) Restricted (14.7 L/min) (b) Twisted (20.4 L/min) (c) Straight (22.5 L/min)

Figure 1-1: Vortex regimes in hyperbolic funnel [1].

Experiments on pilot test facilities of hyperbolic funnels using groundwater are being conducted at the Water Application Center (WAC) in *Wetsus*, European Centre of Excellence for Sustainable Water Technology situated in the Netherlands. A schematic of the experimental

setup is given in Appendix A. Depending on the inlet mass flow rate, three different flow regimes, namely Restricted, Twisted and Straight vortical structures, are observed as seen in Figure 1-1. Measuring the dissolved oxygen (DO) levels of water entering and exiting the hyperbolic funnel revealed their superior gas transfer rates (K_La) as high as 65.13 h^{-1} for the Twisted regime [1]. Standard Aeration Efficiency (SAE) is a metric used to gauge the aeration[1] efficiency of a system and it indicates how much power is consumed by the system in order to dissolve one kilogram of oxygen in one hour per unit mass of the fluid. The SAE's corresponding to each of these regimes are calculated at steady-state and are compared with other commonly used aeration systems as shown in Figure 1-2.

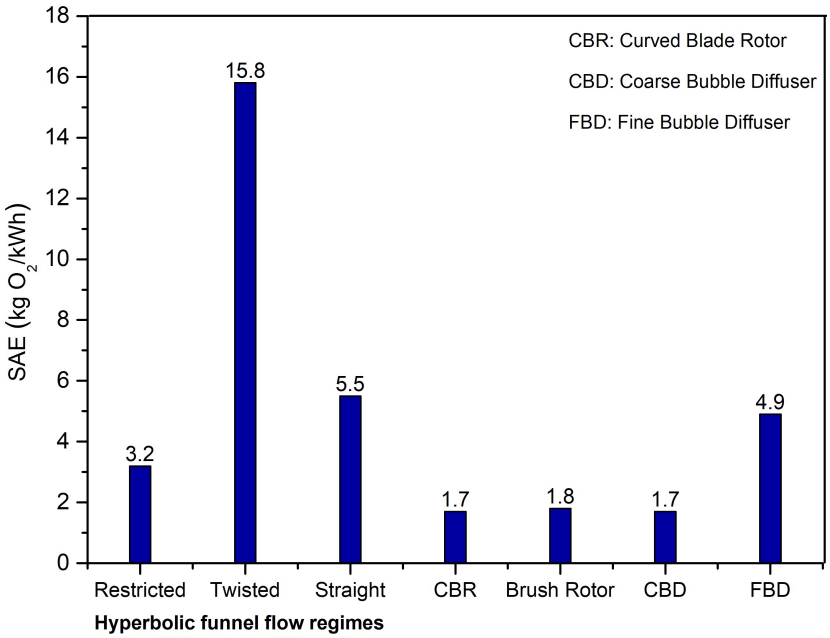

Figure 1-2: Comparison of SAE of vortices in hyperbolic funnels with other commonly used aeration systems [1].

As opposed to other water treatment methods that use chemicals, aeration is an eco-friendly method. In addition to being an essential step in wastewater treatment, it is also one of the most energy-intensive processes consuming 15% to 90% of total electricity [22], and up to 40% of the operating budget [23]. This has lead to a need to make aeration processes more sustainable and economical. With their high gas transfer rates and low energy consumption, vortices generated in hyperbolic funnels might be a promising alternative to the conventional aeration systems presently in use. Hence, a comprehensive study is needed to understand the underlying physical mechanisms that make these systems have such high gas dissolution rates from both a fundamental and industrial perspective.

[1] *Aeration* is the process of dissolving or circulating gases through the water. This aids in the aerobic biodegradation of pollutants by supplying gases (in particular oxygen and ozone) to the micro-organisms present in it.

1-2 Literature study

1-2-1 Aeration Systems

The dissolution of gases in water is relevant in engineering systems for domestic purposes and industrial settings. A system in which gas transfer (in particular but not just limited to oxygen) takes place is commonly referred to as an *aeration system*. This aids in wastewater treatment by inactivating viruses and disinfecting bacteria, removing algae by acting as a biocide, oxidising inorganic compounds like iron and other harmful cyanides/nitrites if present. Engineering gas-transfer systems are broadly classified into:

- **Gas-in-Liquid systems:**

  In these systems, species to be dissolved (i.e. volatile species) is distributed as discrete bubbles into a continuous solvent phase which occupies almost 90% of the systems volume. Diffused aerators fall under this category. In these systems, the volatile species is forced through the holes present in submerged devices (diffusers), and as the bubbles of volatile species rise through the solvent, gas transfer takes place, as shown in Figure 1-3. Depending on the size of bubbles formed, these are further classified into coarse or fine bubble diffusers. The choice of either depends on the application for which they are being used. The desired gas transfer rate dictates both the volume and number of diffusers to be used, ranging from low capacity devices in household aquariums to multiple high flow rate diffusers in case of activated sludge treatment. Other examples of gas-in-liquid systems include anaerobic digesters and venturi-aerators [4].

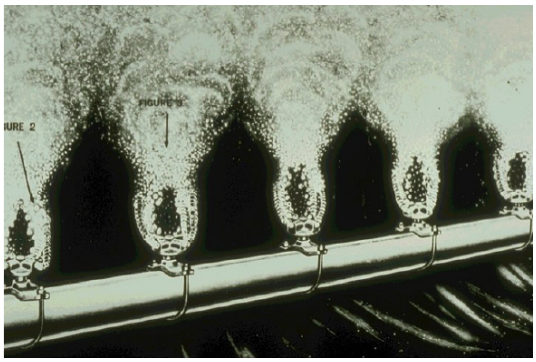

Figure 1-3: Subsurface diffused aeration systems [2]

- **Liquid-in-Gas systems:**

  Droplets of solvent are distributed in a continuous gas phase of volatile species. In these systems, it is the gas phase that accounts for up to 90% of systems volume. The most common example of such a system is the packed tower stripping aerators (Figure 1-4). The tower consists of volatile species and vertically stacked media that provides a large interfacial area for gas transfer. The solvent is sprayed through diffusers, and it being denser, flows downward in an atmosphere of volatile gaseous species. The volatile species are replenished by a supply tube at the bottom.

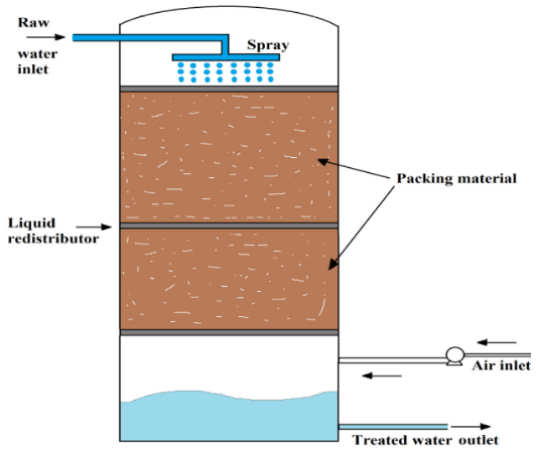

Figure 1-4: Schematic of a packed tower stripping aerator [3].

In the case of vortices in hyperbolic funnels, the phases are in contact at the vortex air-core interface. Hence, they cannot be purely described by either of these classifications and are referred to as *hybrid systems*.

1-2-1-1 Gas transfer

The exchange of molecules of a particular species between gas and liquid phases that are in contact via an interfacial region is referred to as *gas transfer*. This is driven by a tendency to attain equilibrium with respect to the concentration of the species in that region. The molecules of the species that undergo transfer are referred to as the *volatile* species, and the liquid into which they dissolve is known as *solvent*. Transfer of volatile species into liquid phase is referred to *absorption*, while the reverse process is *stripping*. For the sake of relevance to the present study, the gas transfer is discussed only in terms of absorption, but the theory and mathematical relations remain the same for the stripping process also.

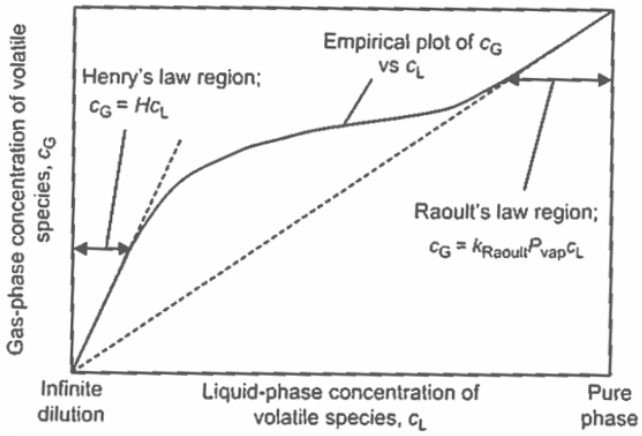

Figure 1-5: Gas-Liquid equilibrium curve [4].

Although the process could be classified as a purely chemical or physical process, it is best to view it as a *physio-chemical* process. The conversion from gas to the liquid phase at the interfacial region is a chemical process, while the movement of species in the bulk of either phase is a physical process. The equilibrium condition at which there is no net gas transfer is characterised by a fixed concentration of gas (c_G) and liquid (c_L) phases of the volatile species. A graph of the same assuming the system contains only a single volatile species of interest and solvent is shown in Figure 1-5.

The extreme regions of the plot Figure 1-5 are characterised by a linear relationship between gas and liquid phase concentrations. The region at infinite dilution, i.e. when volatile species concentration is much lower than the solvent's concentration, is referred to as the *Henry's law* region. The other extreme, i.e. pure phase region, is characterised by a high concentration of volatile species and is referred to as the *Raoult's law region.* Most engineering systems of interest, including the system under investigation, are characterised by the *Henry's law* region. Henry's law in terms of solubility can be stated as

> *At a constant temperature, the amount of a given gas dissolved in a solvent is directly proportional to the partial pressure of that gas in equilibrium with that solvent.*

The constant of proportionality is given by the Henry's constant H

$$H = \frac{c_G}{c_L} \tag{1-1}$$

At a given temperature, a system that is in equilibrium with respect to gas transfer can be characterised by a specific set of concentrations of volatile species in gas and liquid phases (c_G, c_L). This is governed by Henry's constant (equation 1-1). Depending on the actual concentration of volatile species in the solvent (c_L^*) at a given instant, the solvent can be categorized into *undersaturated* ($c_L^* < c_L$) and *supersaturated* ($c_L^* > c_L$) which leads to absorption and stripping of species into and off the solvent respectively. When the concentration is equal to the equilibrium concentration ($c_L^* = c_L$), the solvent is said to be *saturated* with respect to the gas at that temperature resulting in no net gas transfer. At a given temperature, the solvent must be undersaturated in order to dissolve the gas or, in other words, to undergo the process of aeration.

1-2-1-2 Mathematical modelling: Two-film theory

The well known *Two-Film Theory* developed by Walter G. Whitman [24] is used to understand and mathematically model the mechanism of gas transfer. A schematic representation of this is shown in Figure 1-6. Although the transfer happens simultaneously in both directions, we assume that the net transfer is happening from gas to liquid phases, i.e. *absorption* into an undersaturated solvent. At a given instant, the concentration of volatile species is represented in the phases by c_G^* and c_L^* respectively.

The system can be subdivided into three zones through which a species travels namely the *bulk*, *interfacial region* and the *interface* itself. Interfacial regions are of finite thickness in between the bulk and the gas-liquid interface. In this zone, the molecules of the species are surrounded by gas-phase on one side, and liquid phase on the other and hence the forces

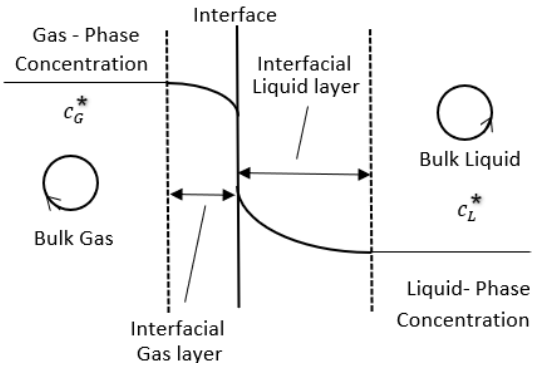

Figure 1-6: Schematic representation of the Two-film theory gas transfer model.

acting on them are different from that of the bulk phase where a single-phase surrounds these molecules. The interface is the boundary region the species has to cross to transfer into the other phase. It is assumed that interfacial regions are in a laminar flow state, and turbulence (if it exists) is only present in the bulk regions.

When the species is being transferred, the overall resistance can be represented as a sum of resistances offered by these individual zones (equation 1-2)

$$R = R_{bulk} + R_{interfacial-region} + R_{interface} \tag{1-2}$$

The step which offers the most resistance to mass transfer is referred to as the *rate-limiting step* of the process. It is experimentally observed that, among several volatile species dissolving into the liquid from the gas phase, the rate of gas transfer is directly proportional to their molecular diffusivities [4]. As molecular diffusion is dominant in a laminar flow region, transfer through the gas/liquid phase interfacial regions must be offering the highest resistance. In the case of ozone dissolution into water, the liquid side interfacial region is the rate-limiting step as observed by Berry et al. [25].

The rate at which a volatile species enters solution from a gas phase ($\mathrm{RGT_L}$) is directly proportional to the extent of disequilibrium, i.e. the difference between equilibrium (c_G) and actual concentrations (c_G^*). The constant of proportionality is given by a product of overall gas transfer rate (K_L) and amount of interfacial area per unit volume (a_L).

$$RGT_L = [K_L a_L][c_G - c_G^*] \tag{1-3}$$

Each term in this rate equation 1-3 is briefly analysed below, and an in-depth analysis of the same can be found in [4].

- **Rate Constant:**
  1. Liquid side mass transfer coefficient (K_L)
     (a) Increasing temperature of the system increases K_L. However, this increase is less than the decrease in driving force ($c_G - c_G^*$) of the gas transfer process leading to an overall decrease in the amount of gas transferred, as seen in Figure 1-7. Hence increasing the temperature of the system is not an appropriate choice to increase gas transfer rates.

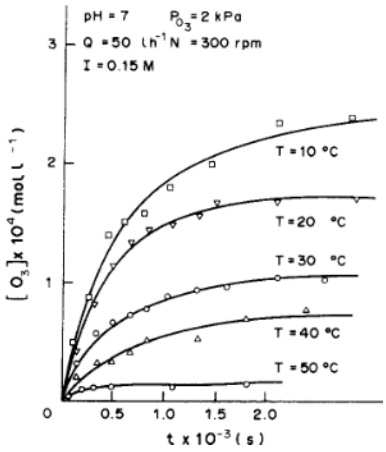

Figure 1-7: Influence of temperature on ozone dissolution in water [5].

(b) Increasing mixing intensity in the phase that offers maximum resistance i.e. liquid side in case of ozone transfer enhances K_L.

2. Interfacial area per unit volume (a_L)
   (a) Gas transfer rate increases with increase in area available for gas dissolution.

- **Driving Force** $c_G - c_G^*$:
  1. By increasing the amount of ozone concentration in the gas supplied would reduce the concentrations of oxygen and other gases leading to higher dissolution rates of ozone.
  2. Increasing the pressure of gas supply also enhances aeration efficiency as gas species travels through the interfacial layer with a greater momentum. However, it should be noted that the system has to remain undersaturated (or saturated at the limiting case) with respect to atmospheric conditions, else the gas would transfer out of the liquid in working conditions.

In summary, molecules from the bulk of the liquid phase need to be transported to the interfacial region where volatile species in the gas phase diffuses into it. Then these molecules need to be transported back into the bulk, thereby making space for other undersaturated molecules to fill the interfacial region leading to a continuous cycle of transport and diffusion. Intense mixing in the bulk and higher surface area for gas transfer further enhances gas transfer rates.

1-2-2 Vortices

Vortex motions have been one of the heavily researched topics in the field of fluid sciences. Due to the broad-scale spectrum ranging from few millimetres (bath-tub vortex) to hundreds of kilometres (cyclone) and the driving forces responsible for their formation, the definition of a vortex is not unique. Before understanding them from a fundamental and mathematical perspective, discussing a few examples of commonly observed vortical motions would be worthwhile.

Studies on vortices date back to a 15th century's sketch by Leonardo da Vinci in which he described vortex motions that he had observed in water. Water draining through the outlet of a sink or bathtub due to gravitational forces generates a vortex flow structure, namely, the *plug-hole vortex*. *Cyclone* formation is also an example of vortex flow and is temperature driven. Vortices are also formed in water bodies when two opposing currents meet, or if an obstacle is encountered in the path of a current, these are commonly referred to as *whirlpools*. These vortices are shown in Figure 1-8. Vortices are also formed by an aeroplane's wings, rotating PET bottles, intakes of hydraulic power plants.

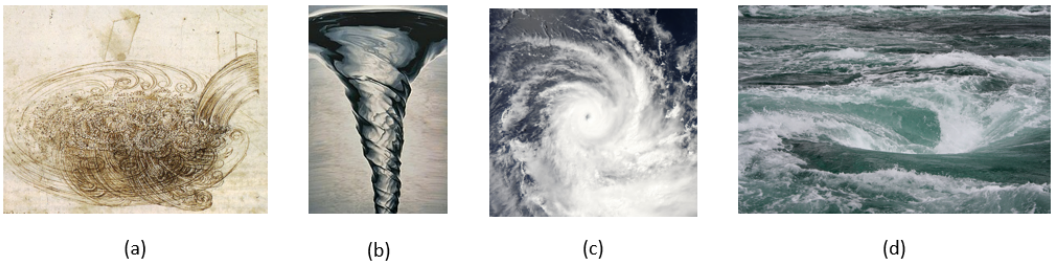

Figure 1-8: Vortex flow structures (a) Sketch by Leonardo da Vinci [6] (b) Plug-hole vortex [7] (c)Tropical cyclone Gillian [8] (d) Naruto whirlpools [9].

A definition of a vortex relevant to the present study was given by Lugt [10] as

Rotating motion of a multitude of material particles around a common center.

Another insightful description was given by Sean Mulligan [11] from the work of Johansson et al. [26], in which a vortex motion is described as

Ordered, self-organised structures of fluid motion which nature prefers over chaos and thus have been an impetus for deep scientific inquiry for centuries.

1-2-2-1 Fundamentals

In this section, basic definitions and theorems relating to fluid motion and vortices will be discussed. For mathematical convenience, as a vortex core aligns with a cylindrical coordinate system (Figure 1-9), it is used in the present study. At a given location, a vector field like velocity field[2] ($\boldsymbol{u}$), is specified by the vector sum of its components in radial, axial

[2]In this report variables in bold denote vectors like velocity vector ($\mathbf{u}$), vorticity vector ($\mathbf{\Omega}$).

and azimuthal/tangential directions (u_r, u_z, u_θ), while $(\hat{e}_r, \hat{e}_z, \hat{e}_\theta)$ represent unit vectors along those directions.

$$\boldsymbol{u} = u_r\hat{e}_r + u_z\hat{e}_z + u_\theta\hat{e}_\theta \tag{1-4}$$

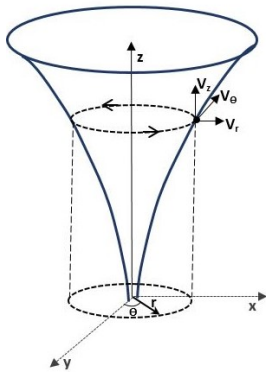

Figure 1-9: Cylindrical coordinate system with vortex core aligned with z-axis.

Vorticity ($\boldsymbol{\Omega}$) represents how a fluid element would spin locally and is a vector quantity defined at every location in the flow field. It is numerically equal to the curl of velocity field and can be expressed as:

$$\boldsymbol{\Omega} = \operatorname{curl} \boldsymbol{u} = \boldsymbol{\nabla} \times \boldsymbol{u} = [\Omega_r, \Omega_\theta, \Omega_z] = \left[\frac{1}{r}\frac{\partial u_z}{\partial \theta} - \frac{\partial u_\theta}{\partial z}, \frac{\partial u_r}{\partial z} - \frac{\partial u_z}{\partial r}, \frac{1}{r}\frac{\partial r u_\theta}{\partial r} - \frac{1}{r}\frac{\partial u_r}{\partial \theta}\right] \tag{1-5}$$

Its components quantify the average deformation rates of a fluid element in two mutually perpendicular planes due to which the fluid element would rotate. Vorticity differs from rotation of fluid; the former denotes local spinning of fluid element, while the latter describes how a fluid element follows curved trajectories around an axis with certain angular velocity. Considering two velocity field distributions that have only radial components

1. $u_\theta \propto 1/r$
2. $u_\theta \propto r$

In both these flows the fluid rotates around an axis (following curved streamlines) with certain angular velocity. For the first distribution, vorticity is zero (substituting velocity field into equation 1-5) and hence, fluid elements do not spin locally. Such flows are known as *irrotational flows*. In the second case, the vorticity field is non-zero and hence, such flows are classified as *rotational flows*. This is also referred to as solid body rotation and it can be shown that in such a flow, vorticity of a fluid element is equal to twice the angular velocity of the fluid.

A fluid need not essentially follow curved streamline paths or rotate with a certain angular velocity around an axis to be rotational. The flow between two plates in which velocity varies linearly (linear Couette flow) is also a rotational flow. In this case, shearing action causes the fluid elements to rotate locally. However, the terms *irrotational* or *rotational* flows used in

literature are based on vorticity being zero or non-zero and thus refer to a tendency of fluid elements to spin locally.

Circulation (Γ) is a scalar quantity which is used to characterize the strength of a vortex. It is the line integral of the tangential component of velocity around a closed curve. Using Stokes theorem, circulation can be defined as the flux of vorticity field across a unit normal area ($\boldsymbol{dA}$).

$$\Gamma = \oint_C \boldsymbol{u}.\boldsymbol{dl} = \int_A \boldsymbol{\Omega}.\boldsymbol{dA} \tag{1-6}$$

Here $\boldsymbol{dl}$ represents the differential displacement along the closed curve C.

1-2-2-2 Formation mechanism

The formation of a vortex structure can be explained based on the principle of conservation of angular momentum, which states that:

When the net external torque acting on a closed system about a given axis is zero, then total angular momentum about that axis remains constant.

Based on this, it can be shown that for such a system, the tangential velocity component of a fluid particle varies inversely with the radial distance from the axis of rotation.

$$\begin{aligned} L = \left(mr^2\right)\left({}^{u_\theta}/_{r}\right) &= \text{ const} \\ u_\theta &= \text{ const } /(mr) \\ u_\theta &\propto 1/r \end{aligned} \tag{1-7}$$

Here, L represents angular momentum and m denoted mass of the fluid parcel. The term mr^2 represents the mass moment of inertia, while u_θ/r represents the angular velocity of the fluid parcel.

Assume an elemental fluid particle is approaching an axis (directed along $\hat{e}_z$) with a radial velocity u_r. If by some means the fluid particle is given a swirl that generates a tangential velocity component u_θ, it begins to rotate around that axis in the $r-\theta$ plane. The fluid-particle might also be having a velocity component parallel to the axis (i.e. axial velocity u_z) caused by pressure gradients (gravitational forces in case of the hyperbolic funnel) which makes it follow a spiralling path downwards. A multitude of such fluid particles generates a three-dimensional swirling flow, i.e. a *vortex*. In order to conserve angular momentum, the tangential velocity component of the fluid increases (leading to decreasing pressure) with decreasing radial distance from the axis. This results in a free surface dip and air entrainment into the vortex. A comprehensive analysis of the mechanisms behind a free surface dip and air entrainment can be found in the works of Lubin and Springer [27], and Möller [28] respectively.

The formation of a vortex structure is based on how the swirl or vorticity is imparted to the fluid. This can be done in the following three ways:

1. **Coriolis Effect:** This is the deflection of objects in motion due to earth rotation. In small scales systems (vortices in hyperbolic funnels or vortices formed at hydraulic intakes), the inertial forces dominate rotational Coriolis forces, and hence this is not an influencing parameter [28]. However, in large scale systems like the formation of cyclones, Coriolis forces determine the direction of rotation.

2. **Flow conditions:** Vorticity generated in the fluid due to flow separations or velocity gradients might generate local vorticity in the fluid. These may accumulate farther downstream, leading to a point vortex.

3. **Induced vorticity:** As opposed to the previous cases in which there is an unsteady supply of vorticity, approach flow geometries may be designed to generate strong vortices in which air-core extends till the outlet. An inlet tube tangential to the upper cylindrical portion induces the necessary swirl in the case of hyperbolic funnels (Appendix A) and are therefore referred to induced vortices.

1-2-2-3 Classification

Based on the pathlines followed by the rotating fluid elements, Lugt [10] classified vortices as shown in Figure 1-10. If the pathlines are closed, a planar vortex is formed, which can again be classified into a symmetrical planar vortex (concentric circular) or an asymmetrical planar vortex. If the pathlines are not closed and form a spatial structure, they are referred to as a spiral vortex. If the diameter to length ratio is low, a disk-like structure of spiral vortex is formed; on the other hand, a columnar vortex is formed if the ratio is high.

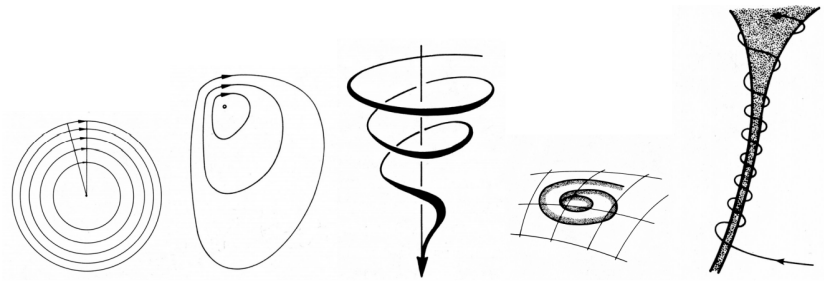

Figure 1-10: Classification of vortices [10].

Depending on the location where a vortex forms, they can be classified into surface or a sub-surface vortex (at pump-intakes in case of underground pumping stations). The stability of a free-surface vortex, can be determined by the relative ratio of inertial and circulatory forces. A non-dimensional parameter governing stability was proposed by Klimenko [29] in the form of Rossby number (Ro) in both axial and radial directions

$$Ro_r = \frac{u_r}{\sqrt{\Gamma\Omega_z}} \quad \& \quad Ro_z = \frac{u_z}{\sqrt{\Gamma\Omega_z}} \tag{1-8}$$

If Ro is large, a surface dip develops, the depth of which increases with the increasing rotation rate of the fluid. Beyond a certain value of rotation rate, this tends to be unstable shedding air bubbles [30]. Such a vortex is said to be in a *weak-state*. As the rotation rate further increases (Ro decreases), the air core extends along the full vortex length, developing a fully stable air-core that extends along the whole length of the circulating fluid. Then the vortex is said to be in a *strong-state*. In summary, axial forces dominate in a weak vortex, and rotational forces dominate in a strong vortex. Experimental work on the transition from a

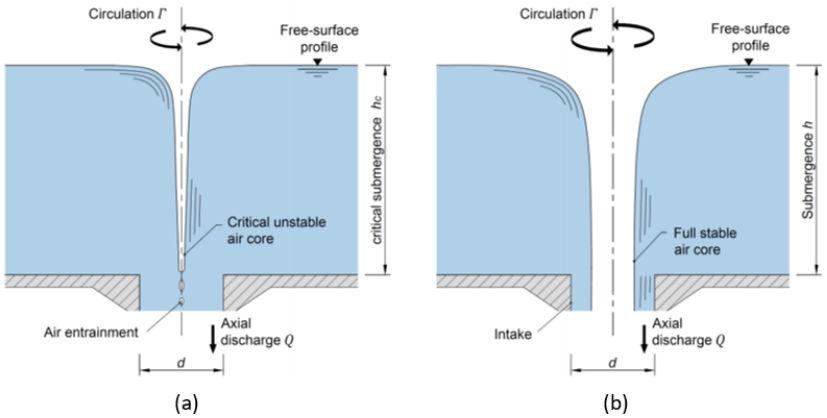

Figure 1-11: Schematic of a (a) weak-vortex and (b) strong-vortex [11].

weak vortex to a strong vortex can be found in the work of Knauss [31]. A schematic of a vortex in both these states is shown in Figure 1-11.

A vortex can be classified into a Free-vortex or a Forced-vortex. Free-vortex develops due to swirling motion already present in the fluid (or induced by forces of nature), and no external torque is needed to maintain the vortex. In such a case, tangential velocity varies inversely with radial distance from the centre. Cyclones, bath-tub vortices, whirlpools fall under this category. A vortex might also be generated artificially (rotating a vessel containing the fluid), in which an external force is required to sustain the vortex. In this case, the fluid behaves as a rigid body rotation with tangential velocity increasing linearly with radial distance. This is known as a Forced vortex, and vortices generated in PET bottles fall under this category.

Vortices formed in hyperbolic funnels are generated due to induced vorticity, and they behave as a free surface vortex. Also, the air-core extends all through the length of the funnel as seen in Figure 1-1 and hence further discussion is limited to Induced Strong Free-Surface Vortex (FSV) only.

1-2-2-4 Equations of motion and Rankine vortex

In hyperbolic funnels, water is the working fluid, which under the given working conditions can be assumed to be a Newtonian fluid, i.e. incompressible fluid (ρ = const) of contact viscosity, (μ = const). The flow governing equations are given by the well known Naiver-Stokes Equations.

Continuity Equation:

$$\frac{1}{r}\frac{\partial\left(ru_r\right)}{\partial r}+\frac{1}{r}\frac{\partial u_\theta}{\partial\theta}+\frac{\partial u_z}{\partial z}=0 \tag{1-9}$$

Momentum equations:

- Radial:

$$\rho\left(\frac{\partial u_r}{\partial t}+u_r\frac{\partial u_r}{\partial r}+\frac{u_\theta}{r}\frac{\partial u_r}{\partial \theta}-\frac{u_\theta^2}{r}+u_z\frac{\partial u_r}{\partial z}\right)=-\frac{\partial p}{\partial r}+ \mu\left[\frac{1}{r}\frac{\partial}{\partial r}\left(r\frac{\partial u_r}{\partial r}\right)-\frac{u_r}{r^2}+\frac{1}{r^2}\frac{\partial^2 u_r}{\partial \theta^2}-\frac{2}{r^2}\frac{\partial u_\theta}{\partial \theta}+\frac{\partial^2 u_r}{\partial z^2}\right] \tag{1-10}$$

- Tangential:

$$\rho\left(\frac{\partial u_\theta}{\partial t}+u_r\frac{\partial u_\theta}{\partial r}+\frac{u_\theta}{r}\frac{\partial u_\theta}{\partial \theta}+\frac{u_\theta u_r}{r}+u_z\frac{\partial u_\theta}{\partial z}\right)=-\frac{1}{r}\frac{\partial p}{\partial \theta}+ \mu\left[\frac{1}{r}\frac{\partial}{\partial r}\left(r\frac{\partial u_\theta}{\partial r}\right)-\frac{u_\theta}{r^2}+\frac{1}{r^2}\frac{\partial^2 u_\theta}{\partial \theta^2}-\frac{2}{r^2}\frac{\partial u_r}{\partial \theta}+\frac{\partial^2 u_\theta}{\partial z^2}\right] \tag{1-11}$$

- Axial:

$$\rho\left(\frac{\partial u_z}{\partial t}+u_r\frac{\partial u_z}{\partial r}+\frac{u_\theta}{r}\frac{\partial u_z}{\partial \theta}+u_z\frac{\partial u_z}{\partial z}\right)=-\frac{\partial p}{\partial z}+ \mu\left[\frac{1}{r}\frac{\partial}{\partial r}\left(r\frac{\partial u_z}{\partial r}\right)+\frac{1}{r^2}\frac{\partial^2 u_z}{\partial \theta^2}+\frac{\partial^2 u_z}{\partial z^2}\right]+\rho g \tag{1-12}$$

These coupled non-linear partial differential equations need to be solved to get the velocity and pressure in a vortex across space and time. In order to get a basic understanding of the flow fields in a vortex, Einstein and Li [32] made use of the quasi-cylindrical approximation [33] in which

1. Fluid is ideal ($\mu = 0$).
2. Flow is steady and axisymmetric.
3. Negligible gradients in axial directions as compared to the radial direction.

Solving the tangential and radial momentum equations for tangential velocity and pressure distribution leads to [11]

$$v_\theta r = constant \tag{1-13}$$

$$p_\infty - p = \frac{\rho\Gamma^2}{8\pi^2 r^2} \tag{1-14}$$

This is referred to as *ideal irrotational vortex*. In its present form, it is suitable to predict flow fields away from the origin. However, both pressure and velocity approach infinity at the origin (as $r \to 0$). It is also experimentally observed that the constant in equation 1-13 is proportional to the circulation (Γ) of the flow field. However, for a velocity profile given by equation 1-13, the flow is expected to be irrotational as its vorticity is zero as discussed in Section 1-2-2-1 and hence mathematically, its circulation should also be equal to zero. This anomaly happens as the velocity field has a singularity at the origin ($r = 0$). At the origin, the velocity field approaches positive infinity from one side and negative infinity from the other and hence the fluid experiences an enormous shearing force. For such a vortex, it is

assumed that the vorticity is concentrated only at the origin and is zero everywhere else in the flow field. This is referred to as a *free* or *potential vortex*. So circulation is present around a closed loop around the origin where vorticity is concentrated. However, this is a theoretical model and cannot exist physically.

This issue is resolved by assuming a core of radius r_c surrounding the origin where the flow is modelled as a forced vortex with linearly increasing velocity field (simulating the rapidly spinning air core), and this core is surrounded by the irrotational vortex (modelling the spiralling free vortex flow) with the same amount of circulation (Γ_∞) for both regions. This is referred to as a *Rankine vortex* The velocity and pressure fields are shown in Figure 1-12.

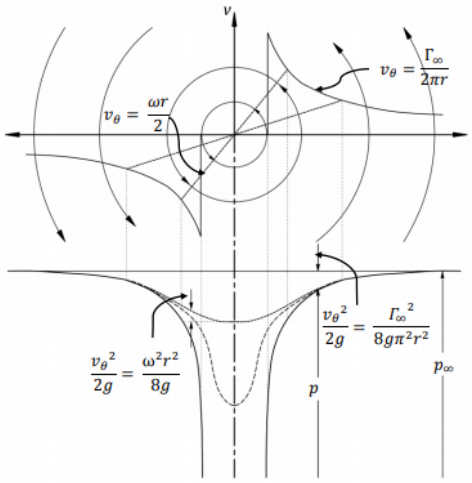

Figure 1-12: Velocity and pressure fields in a rankine vortex [12].

$$u_\theta(r) = \begin{cases} \frac{\Gamma_\infty r}{2\pi r_c^2}, & 0 \leq r \leq r_c \\ \frac{\Gamma_\infty}{2\pi r}, & r_c \leq r \leq \infty \end{cases}, u_r = 0, u_z = 0 \tag{1-15}$$

$$p_\infty - p = \begin{cases} \frac{\rho\omega^2 r^2}{8}, & 0 \leq r \leq r_c \\ \frac{\rho\Gamma_\infty^2}{8\pi^2 r^2}, & r_c \leq r \leq \infty \end{cases} \tag{1-16}$$

There is a discontinuity in pressure and velocity field even for this model at the interface ($r = r_c$) which cannot exist in reality due to viscous forces. A large number of models have been developed to resolve this issue and a comprehensive review can be found in [11]. This is used as a basis model to solve many vortex systems. Vortex flow near to the air-core region is referred to as the *near-field region* while farther away is the *far-field region.*

1-2-2-5 Flow organisation

The velocity field in a free surface vortex can be categorised into

1. Primary flow field: Represents circulation (tangential velocity, u_θ).
2. Secondary flow field: responsible for mixing in the bulk of a vortex and ensuring continuity of flow through the system (axial, u_z & radial velocities, u_r).

In their experimental studies on free surface vortices, Daggett and Keulegan [13] observed that at a given radial distance from the air core, the tangential velocity component (u_θ) is nearly a constant value along the depth of cylindrical tank as shown in Figure 1-13. The deviations observed at the bottom are due to the formation of a boundary layer close to the tank's bottom boundary wall (i.e. Ekman layer, to be explained later).

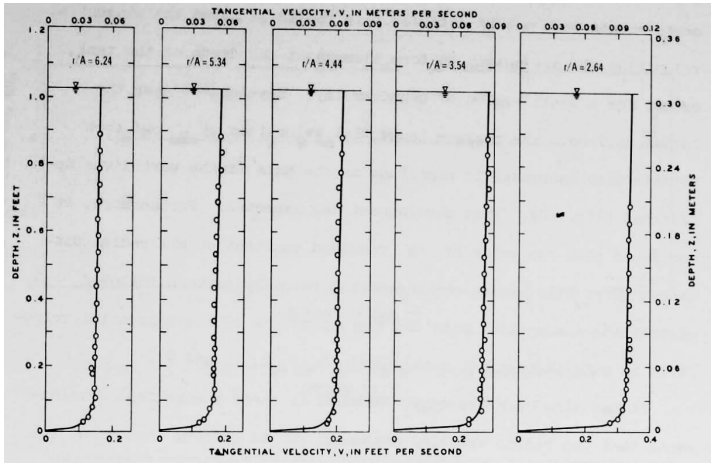

Figure 1-13: Tangential velocity distribution (horizontal axis) with increasing depth from free surface (vertical axis) at various non-dimensional radial distances [13].

It is in general agreed that axial velocities are confined near to the air core region as show in Figure 1-14 and gradients do exist with varying height in contrast to the quasi-cylindrical approach. In the far-field region away from the boundaries, axial velocities have negligible influence on flow organisation.

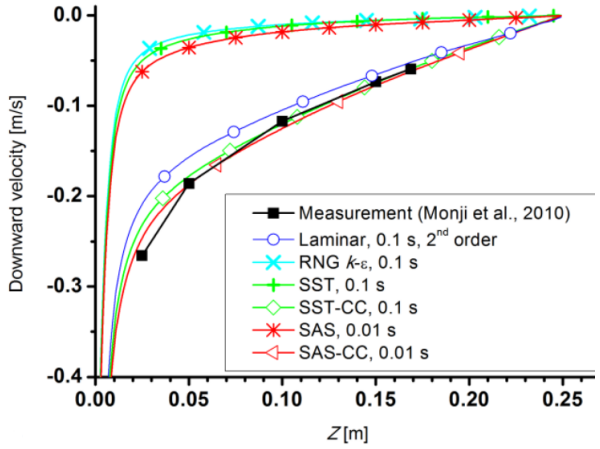

Figure 1-14: Axial velocity distribution (vertical axis) with radial distance (horizontal axis) [14].

In many of the earlier developed theoretical models for vortices, it was assumed radial velocity (u_r) had a uniform distribution throughout the depth of the fluid. In contrast to this, experimental studies [11] on confined vortices revealed the radial velocity vary with depths

as seen in Figure 1-15. The sudden decrease observed near the air core was due to the strong influence of axial velocities (u_z) in that region as stated by Anwar H. O. [34].

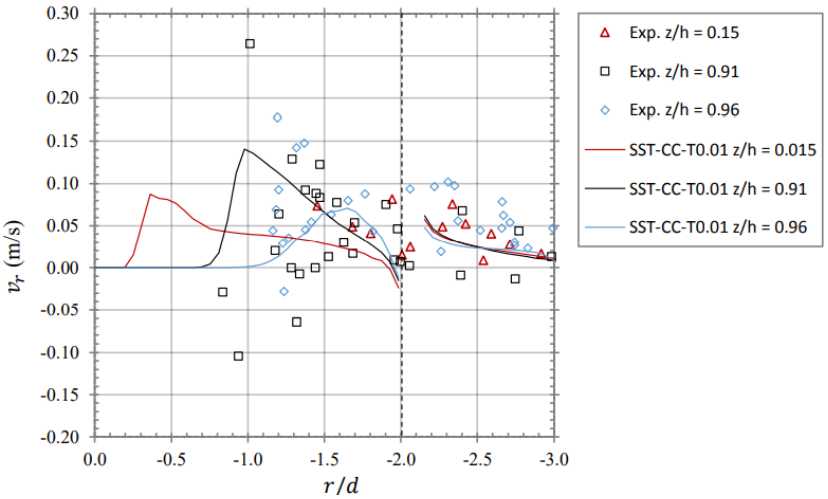

Figure 1-15: Radial velocity distribution (vertical axis) with increasing radial distance (horizontal axis) at various non-dimensional sub-surface depths [11].

Boundary layers (also referred to as the shear layers) develop in the flow when fluid comes in contact with a solid boundary. The viscosity in the fluid tends to nullify the relative motion between the fluid and the wall, which is also commonly referred to as the no-slip boundary condition. In rotating systems, two different shear layers are usually observed

1. **Ekman Layer**: In their analysis on vortices generated by fluid draining via a bottom hole in rotating a cylindrical Andersen et al. [30] observed an Ekman layer at the bottom boundary. This leads to a localised upward movement of fluid at the bottom near the exit. i.e. Ekman pumping. Such layers also form on the top of the container if completely filled.

2. **Stewartson layer**: These are the vertical shear layers developed in a rotating container near the sidewalls and were first observed by Stewartson [35]. The fluid flowing radially towards the wall due to the centrifugal force would be transported through the Stewartson layer downwards to the bottom Ekman layer and then transported radially inwards to the drain hole and discharged out of the rotating container.

The funnel under consideration is such that the flow exits the bottom of the funnel into a pipe whose inner diameter is equal to the funnel outer diameter with no bottom boundary wall. So Ekman layer is not expected to develop in our case.

Efficient aeration capabilities of hyperbolic funnel vortices might lie in the intense mixing of the diffused gas inside the bulk of fluid, and hence it is essential to understand the secondary flow field patterns and the instabilities arising in them for various flow regimes. A fluid motion is stable if any perturbations do not grow in time as viscous forces dampen them out. If, on the other hand, these perturbations lead to either development of another laminar flow or turbulent state, the flow is said to be unstable [36].

As mentioned before, the term vortices covers an extensive range of flows, and it is common practice in hydrodynamic systems to analyse one system by drawing analogies with the other. Flow generated in between two-coaxial independently rotating cylinders is one of the simplest examples of a rotating flow, and such systems are referred to as the *Couette flow* systems which are one of the classical systems in the physics of fluids. They are mathematically well-defined by the Navier-Stokes equation, and also their flow organisation is well understood. The stability analysis of the Couette flow system is used to analyse many rotating flow systems, including a strong free-surface vortex. In the sub-sections to follow, the Couette flow systems are briefly introduced, and an analogy of its instabilities between Couette flow systems and strong FSV are discussed.

1-2-2-6 Couette flow

Flow-induced in a viscous, incompressible fluid confined between two co-axially placed independently rotating cylinders is termed as Couette Flow. This is schematically represented in Figure 1-16, where $r_i(r_o)$ and $\omega_i(\omega_o)$ are the radii and angular velocity respectively of inner(outer) cylinder. L represents the length, and d is the annular width occupied by the fluid.

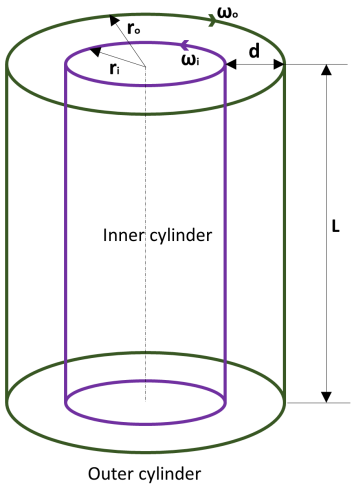

Figure 1-16: Schematic of a Couette flow system.

The geometric parameters of a Couette system are non-dimensionalized in the form of radius ratio (η) and Aspect Ratio (ζ), which are defined as:

$$\eta = \frac{r_i}{r_o} \quad \& \quad \zeta = \frac{L}{d} \tag{1-17}$$

Rotation of inner and outer cylinders are quantified in terms of their respective Reynolds numbers (Re_i and Re_o). It indicates the relative strengths of inertial to viscous forces.

$$Re_i = \frac{r_i \omega_i d}{v} \quad \& \quad Re_o = \frac{r_o \omega_o d}{v} \tag{1-18}$$

Here, ν is the kinematic viscosity of the fluid. The rotation ratio a is defined as $a = \omega_o/\omega_i$. Assuming the rotation direction of inner cylinder as positive i.e. $\omega_i > 0$, positive value of a

denotes co-rotation while negative corresponds to counter-rotating cylinders. The difference in angular velocities of inner and outer cylinder drives the flow, and this is non-dimensionalised in the form of Taylor number (Ta)

$$Ta = \frac{(1+\eta)^4}{64\eta^2} \frac{d^2 \left(r_\mathrm{i} + r_\mathrm{o}\right)^2 \left(\omega_\mathrm{i} - \omega_\mathrm{o}\right)^2}{v^2} \tag{1-19}$$

Taylor number is always a positive quantity. Quasi-Nusselt number (Nu^ω) is the ratio of torque (τ) necessary to maintain the constant angular velocity of cylinders to the torque that would be necessary if the flow was laminar (τ_{lam})

$$Nu^\omega = \tau / \tau_{lam} \tag{1-20}$$

One of the flow regimes of Couette flow, namely the Taylor-Couette flow (TC) field, bears close resemblance with Rayleigh-Bénard flow (buoyancy-driven flow of a fluid heated from below and cooled from above) as highlighted by Eckhardt et al. [37]. Hence, the Taylor Number (equation 1-19) and Quasi-Nusselt Number (equation 1-20) have been defined analogously to the Rayleigh number and Nusselt number in a Rayleigh-Bénard flow.

Flow regimes

The flow is purely circular for low angular velocities of the inner cylinder. This flow is referred to as the circular Couette flow (CCF), for which the tangential velocity profile as a function of radii is given by

$$v_r(\theta) = Ar + \frac{B}{r} \tag{1-21}$$

Where the constants A and B can be determined by no-slip boundary condition

$$A = \omega_i \frac{(a - \eta^2)}{1 - \eta^2}, \ \mathrm{B} = \omega_i \frac{r_i^2 (1 - a)}{1 - \eta^2} \tag{1-22}$$

The necessary and sufficient condition for stability of an inviscid Couette flow was given by Rayleigh et al. [38]. This states that the flow would be stable only if the momentum per unit mass is monotonically increasing as one moves from the inner towards the outer cylinder.

$$\frac{d}{dr} \left(r v_\theta\right)^2 \geq 0 \tag{1-23}$$

This suggests that if the momentum of a fluid parcel at the inner cylinder, $r_i v_\theta(r_i)$ is more than that closer to the outer cylinder, $r_o v_\theta(r_o)$ instabilities begin to develop in the flow. However, in a real fluid, viscous forces tend to stabilise the flow by dampening the perturbations.

Taylor [39] recognised that above a certain angular velocity of the inner cylinder, viscous forces could no longer dampen these instabilities. The flow does not become turbulent immediately but transitions into an intermediate laminar state that consists of toroidal vortex cells periodic in the axial direction referred to as the Taylor-Couette (TC) regime. Across a section of these toroidal vortexes, cells counter-rotating vortices are present, and these are referred to as the Taylor vortices, which are axisymmetric. As the rotation of the inner cylinder increases,

(a) Taylor-Couette flow (b) Wavy vortex flow (c) Fully turbulent flow

Figure 1-17: Experimental images of Couette flow regimes [15].

these toroidal waves become periodic in both axial and circumferential directions forming a Wavy-vortex flow. This transitions into a Fully-turbulent regime where it loses its symmetric nature leading to chaos in the system. Experimental images of these regimes are shown in Figure 1-17.

Further understanding of the velocity profiles for different regimes was obtained from the direct numerical simulations of Ostilla-Monico et al. [16] as shown in Figure 1-18 in which the left-most part is the rotating inner cylinder while the right side represents fixed outer cylinder. With respect to flow in their boundary and laminar layers, these are classified into

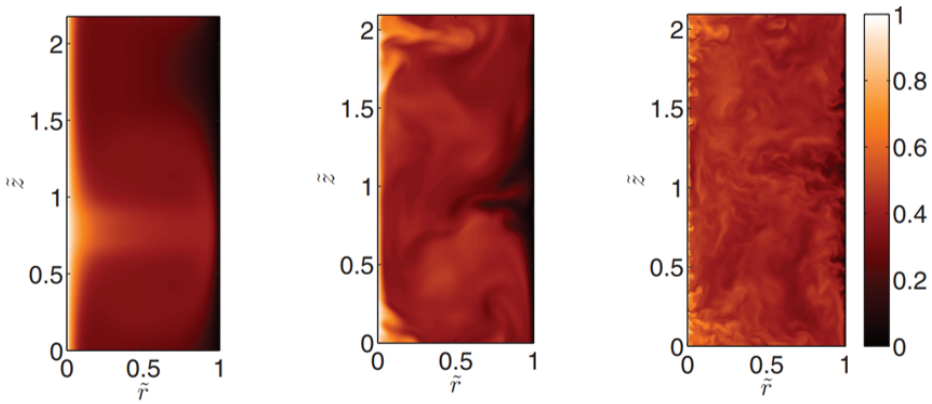

(a) Laminar Regime (b) Classical Turbulent Regime (c) Ultimate Turbulent Regime

Figure 1-18: DNS of Couette flow for pure inner cylinder (left boundary) rotation [16].

1. **Laminar regime:** Corresponds to Taylor-Couette flow regime. In this, both the boundary layer and the bulk are laminar. Coherent structures, i.e. Taylor rolls, are seen.
2. **Classical Turbulent regime:** Corresponds to Wavy-Vortex flow regime. Boundary layers are still laminar while the bulk is mostly turbulent, and Taylor rolls are close to the inner cylinder if they exist. The boundary layer and the bulk are laminar. Coherent structures, i.e. Taylor rolls, are seen.
3. **Ultimate Turbulent regime:** Corresponds to Fully turbulent flow regime. In this, both the boundary layer and the bulk are turbulent.

The terms Couette flow and Taylor-Couette are sometimes used interchangeably in the literature. These, in general, refer to the flow regimes of Couette flow after its initial laminar Circular Couette flow regime, i.e. the regimes represented in Figure 1-18. A comprehensive review on Couette flow done by Grossmann et al. [17] quantifies the occurrence of these regimes for pure inner cylinder rotation with respect to Taylor number as seen in Figure 1-19.

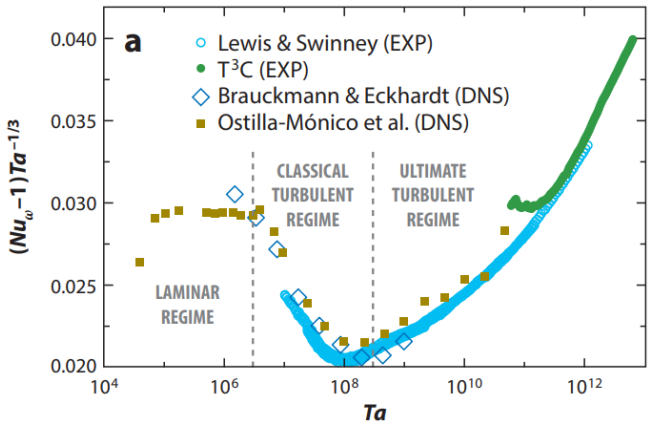

Figure 1-19: Flow regimes in a Taylor-Couette system as a function of Taylor number [17].

1-2-2-7 FSV and TC flow

- **Stability:** Dunst [40] performed experiments to understand the flow stability in a Couette system in which he defined *friction zone* as a stabilisation region in which the angular momentum is exchanged between the inner and outer cylinders due to their relative rotation rates. For the inner cylinder acting as a source of angular momentum (i.e. $\omega_i > \omega_o$), if the outer cylinder rotation drops to zero, he states that *"turbulent fluxes become more and more dominant as compared to the mean fluxes which are laminar in nature"*. Using Rayleigh stability criterion he also showed that, in such a case *"no friction zone exists"*. Hence for sufficient rotation rates of the inner cylinder, a Couette system can develop instabilities for a fixed outer cylinder.

  A Couette flow system for a fixed outer cylinder has a monotonically decreasing tangential velocity profile (equation 1-21 with $B = 0$), and this is similar to tangential velocity profile in the far-field region as discussed in Section 1-2-2-5. Using the stability criterion (equation 1-23), Mulligan et al. [19] showed that the *"secondary flow fled of the FSV with an outer stationary wall can become unstable to axisymmetric perturbations in an analogous manner to the TCF"*. Hence, regarding the onset of instabilities in the secondary flow fields, a Free surface vortex is analogous to a Taylor-Couette system.

- **Secondary flow field:** While performing a three-dimensional numerical simulation of liquid draining from a tank in the form of a vortex Son et al. [18] observed counter-rotating flow structures in the secondary flow field stacked along the axial direction. Comparing these to the Taylor-vortices generated in the Taylor-Couette flow regime (Figure 1-18(a)), these look similar, and hence these were termed as *toroidal Taylor vortex rings*, and the same is represented in Figure 1-20.

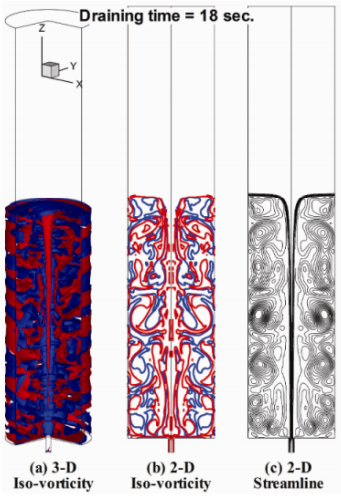

Figure 1-20: Vortex streamlines in a fluid draining out of a tank showing Taylor-Like vortices [18].

In their recent experimental studies, Mulligan et al. [19] constructed a two-dimensional secondary flow structure velocity vector fields for strong free-surface vortices, in which counter-rotating cellular cells were observed similar to Taylor rolls as seen in Figure 1-21. It was also observed from their numerical modelling results that as the aspect ratio of the system increases, the number of Taylor-like vortices also increased.

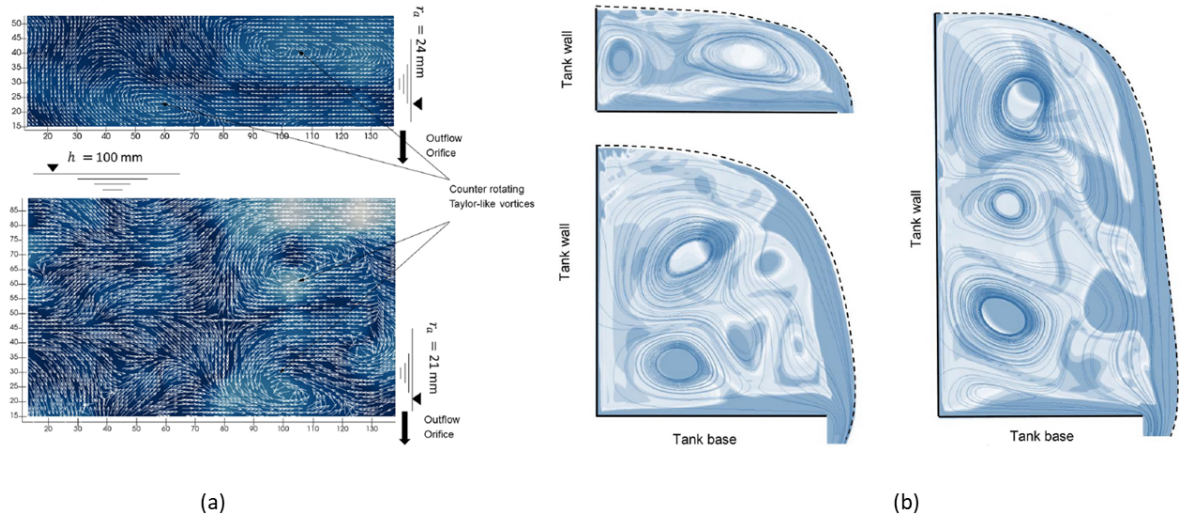

Figure 1-21: Two-dimensional secondary flow fields in a Strong Free-Surface Vortex (a) experimental data and (b) numerical modelling [19].

Hence, a Strong Free-Surface Vortex (FSV) can be treated analogously to a Taylor-Couette (TC) flow. As mentioned before, the rotating central air-core is considered a virtual inner cylinder. As the rotation rate of this virtual cylinder increases, Taylor-like vortices are seen in its secondary flow field. Both these systems differ in the way the flow is sustained. In a TC flow, energy is supplied externally to rotate the inner cylinder against the viscous friction

generated by the fluid. In FSV, fluid circulation in the domain generates a rapidly rotating central air core dissipating the energy by viscous forces, ensuring continuity by outflow. This was put forward by Sean Mulligan [11] and a schematic of an FSV imagined as a TC is shown in Figure 1-22.

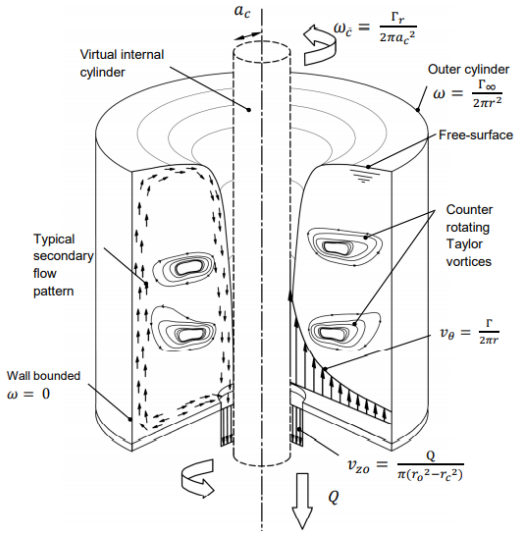

Figure 1-22: Analogy between a FSV and TC flow [19].

1-3 Summary of literature study

For achieving higher gas dissolution rates in a system, molecules from the bulk of the liquid phase need to be transported to the interfacial region where the volatile species in the gas phase diffuses into it. These molecules then need to be transported back into the bulk, making space for other undersaturated molecules to fill the interfacial region. This leads to a continuous cycle of transport and diffusion.

From equation 1-3, it can be concluded that for a given fluid and thermodynamic conditions (i.e. fixed c_G and c_G^*), this process can be enhanced by increasing the intensity of mixing in bulk (K_L) and ensuring as high interfacial area for dissolution as possible (a_L). Experiments on vortices in hyperbolic funnels have demonstrated their capabilities for high gas dissolution rates. It can be hypothesised that this performance is due to its interfacial area and the role of Taylor-like vortices in its secondary flow field. However, the reason behind this phenomenon is still not known with certainty.

In order to validate this hypothesis, detailed information of flow fields is needed. Using techniques like Particle Image Velocimetry (PIV) might aid in analysing the flow field behaviour and understanding the underlying physical mechanisms. However, experimental analysis has limitations regarding measurement errors incurred, constraints of extracting desired physical variables, effects of scaling, etc. On the other hand, modelling the systems using their flow governing equations with suitable numerical techniques eliminates these drawbacks and provides a deeper understanding of the fluid flow phenomenon. Hence a numerical approach is

chosen for this study in which the vortices in the hyperbolic funnel are numerically analysed using commercially available Computational Fluid Dynamics (CFD) package ANSYS Fluent.

1-4 Thesis objectives

Based on the experimental observations and literature study, the following are the objectives of this study:

1. Numerically simulate the vortex regimes to gains insights into the flow field distribution.
2. Validate the obtained results with experimental data.
3. Analyse the regimes of the vortex based on factors that enhance gas transfer rates and thereby reason their superior aeration capabilities.
4. Deduce non-dimensional numbers that characterise different regimes of the vortex.
5. Involve mass transfer effects into the simulations to simulate gas transfer.

Chapter 2

Numerical modelling

2-1 Setup

2-1-1 Experiment

The experimental setup is divided into two sections, (Figure 2-1) namely the *funnel*, which includes the water inlet, the hyperbolic funnel and the cylindrical part with an air vent on the top; and the *extension*, which includes the portion beneath the hyperbolic funnel with the bend and the outlet tubes. The flow in the experiments is divided into two outlet tubes to reduce the back pressure to increase the system's operating range.

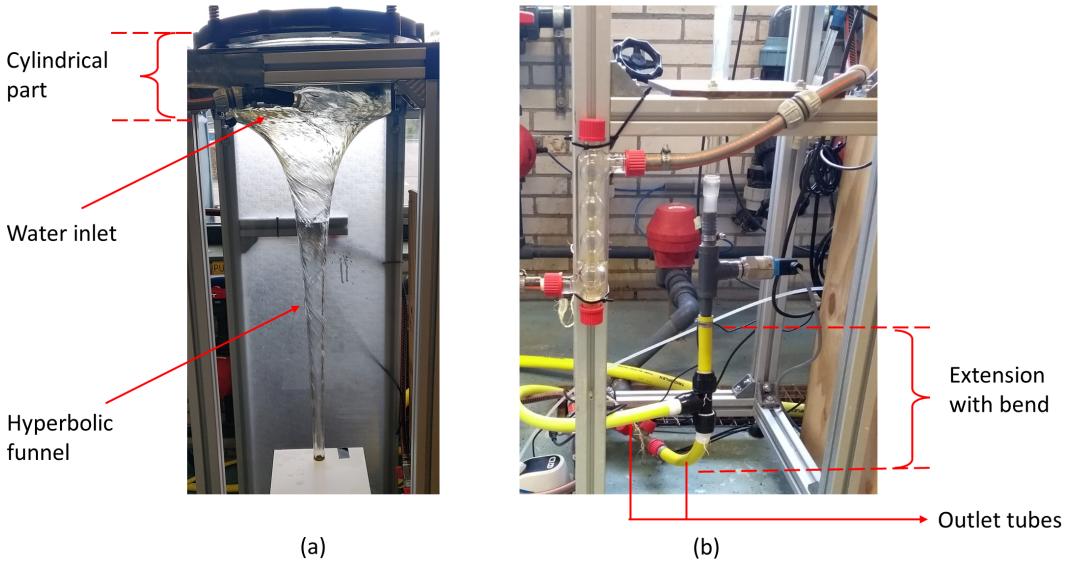

Figure 2-1: Experimental setup divided into (a) *funnel* and (b) *extension* parts.

2-1-2 Computational domain

The computational domain can be modelled either in two-dimensions (2D) or three-dimensions (3D). The former has the advantage of being less computationally expensive. However, the air-core interface formed has a helical structure (which is more pronounced in the Twisted regime as compared to the other two regimes as seen in Figure 1-1), and this interface is not axisymmetric (about $\hat{e_z}$) which rules out the possibility of using a 2D domain. Moreover, the instabilities that arise in the secondary flow field of the vortex are expected to have a 3D organisation [11]. Hence, a 3D computational domain is chosen for the present study.

Since the present study is focused on the hydrodynamics of the vortex formed inside the hyperbolic funnel, in order to save computational time, initially, only the *funnel* section was modelled. However, this did not yield physically valid results, and the reasons for this are explained in Section 2-5-3. In order to get the hydrodynamics of the vortex right, it was necessary to include the *extension* part also. The complete 3D model integrating both these sections is shown in Figure 2-2 (a), and its dimensions on a 2D projection plane are shown in Figure 2-2 (b).

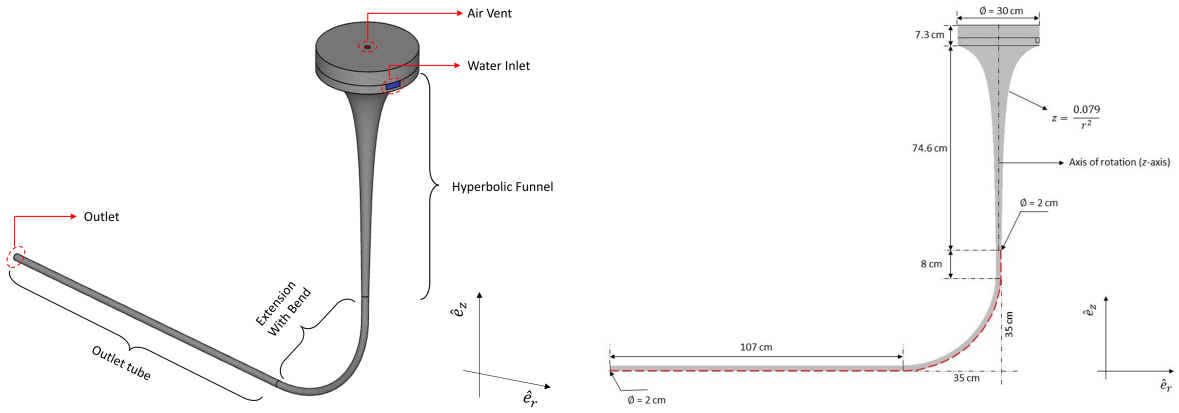

Figure 2-2: Computational domain in (a) 3D and (d) 2D sectional plane with dimensions.

The main differences between the experimental setup (Figure 2-1) and the computational domain (Figure 2-2) are:

- The water inlet tube is not modelled, but instead, its intersection with the cylindrical part is defined as a region on the cylindrical portion.
- The two outlet tubes used in experiments are replaced by a single tube in the computational domain.

The reasons for this will be explained in the subsection on mesh strategy (Section 2-2-1).

2-2 Meshing

In CFD, a given computational domain is sub-divided into several elements/cells (*mesh*) in which the flow governing equations are numerically solved. In the present study, the

commercial software Pointwise V18.4 is used for meshing.

2-2-1 Mesh strategy

Meshes can be broadly classified into

- **Structured mesh**
    1. Cells are topologically similar.
    2. Better convergence and less numerical diffusion.
    3. Difficult to set-up for complex geometries and computationally expensive.
- **Unstructured mesh**
    1. Cells are not topologically similar.
    2. Risk of false numerical diffusion.
    3. Easier to generate for complex geometries.

False numerical diffusion effects are more pronounced in convection dominated flows [41] if the flow is not aligned with the mesh type used, as in the case of unstructured meshes. A radially structured mesh is preferred in order to avoid these effects. Also, for vortex flows, the flow field resolution is more accurate in structured meshes [11]. The simplicity of the present computational domain (Figure 2-2) allows using a block-structured mesh. Hence, a radially structured hexahedral mesh is used in the present study.

The axis of rotation of this radially structured mesh for the *funnel* section is along the axial direction ($\hat{e_z}$) as shown in Figure 2-2 (b). If the water inlet tube were to be included, its axis of rotation would have to be defined separately. By doing so, a structured mesh can be generated for both the *funnel* section and the water inlet tube, but in order to join these two, an unstructured mesh would have to be used at the interface. In order to avoid this, a region on the cylindrical part is defined (Figure 2-2 (a)) such that its surface area is as close to the intersection area of the water inlet and cylindrical part in the experiments (Figure 2-1 (a)).

Once the *funnel* section is modelled using $\hat{e_z}$ as an axis of rotation for the radial mesh, it is then extruded along a path represented in red in Figure 2-2 (b) to generate the outlet tube. In order to generate two outlet tubes as in experiments (Figure 2-1) they would have to be generated with two different axes of rotation and then joined via an unstructured mesh at the interface to the *funnel* section. This is also avoided, and instead, a single outlet tube is modelled. The use of a single outlet tube generates issues relating to back-pressure in the end part of *funnel* section, and this is one of the drawbacks in the present study, as will be further discussed in Section 3-2.

Hernandez-Perez et al. [20] investigated turbulent two-phase flows in pipes using three different 3D structured meshes as shown in Figure 2-3. These are the

1. Cylindrical mesh: These are referred to as the O-mesh grid as the mesh is in the form of concentric circles around the central axis.

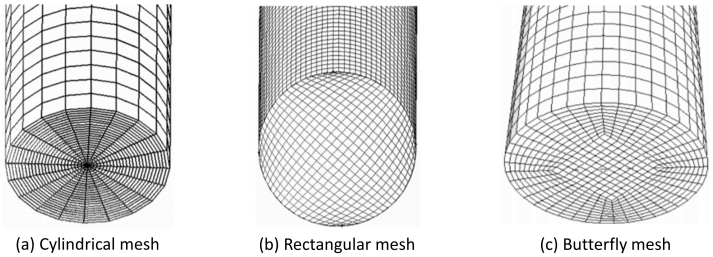

Figure 2-3: 3D structured meshes used in simulating turbulent two-phase flows [20].

2. Rectangular mesh: The entire mesh adopts the form of a repeating H-grid structure.

3. Butterfly mesh: Rectangular/cartesian mesh in the centre surrounded by a cylindrical mesh.

It was observed that although the mesh density increased, a Cylindrical mesh did not produce reliable results. Rectangular meshes lead to skewness in cells at the corners as mesh density was increased. The best results were obtained when a Butterfly structured mesh was used, as this allowed for the mesh to be refined at the cylindrical walls to resolve the boundary layer and prevent a singularity at the origin. This approach was also used by Lim-Chi Ho [42] in his work on simulating vortices in PET bottles.

2-2-2 Methodology

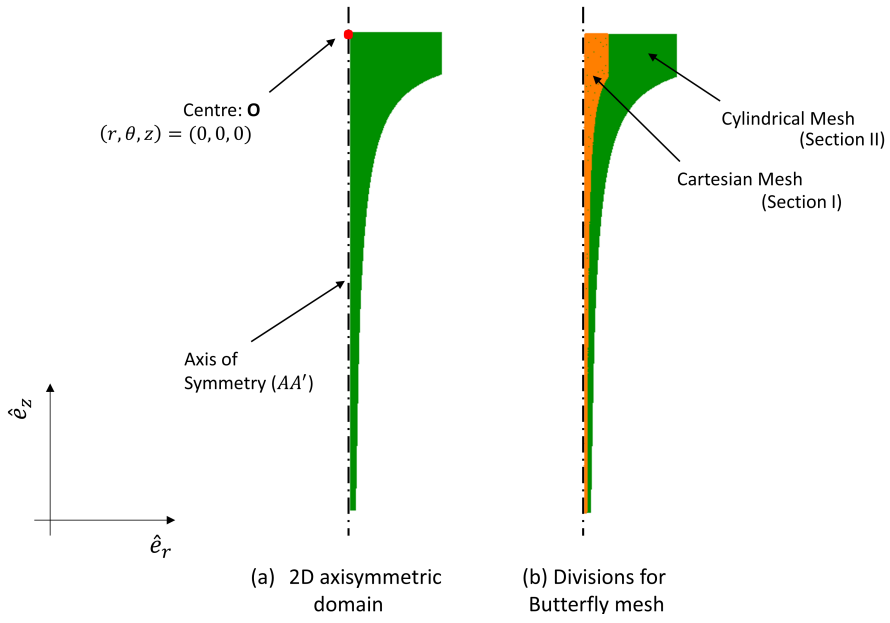

Figure 2-4: 2D axisymmetric representation of the *funnel* section.

The *funnel* section is symmetric about the $z - axis$ and hence can be constructed from a 2D domain lying in the $r - z$ plane. This is shown in Figure 2-4 (a) with its axis of symmetry

($AA^{'}$) directed along $\hat{e}_z$ and passing through the origin of cylindrical axis O. In order to form a cartesian mesh in the centre surrounded by cylindrical mesh (i.e. Butterfly mesh structure), the 2D domain is split into two parts as shown in Figure 2-4 (b) marked as Section I and II. The domain is split such that Section II (radial mesh) has a larger area than Section I (cartesian mesh) as the flow is expected to be predominantly in the tangential direction.

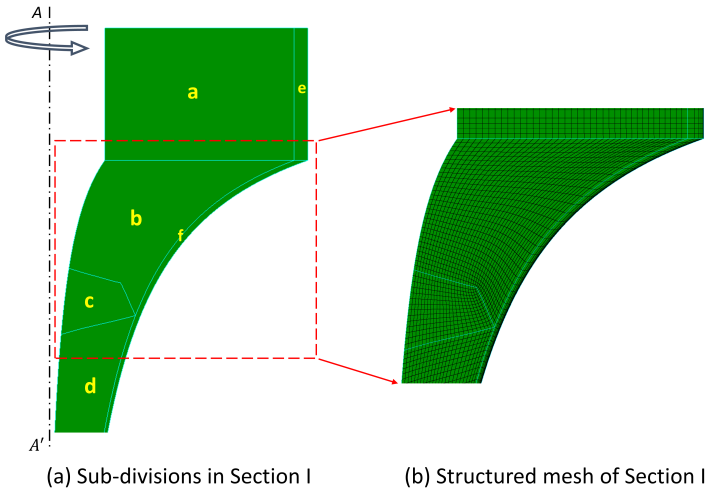

Figure 2-5: 2D structured meshing of Section I.

Section II is subdivided into 6 zones/blocks (Figure 2-5 (a)). This is referred to as *multi-block grid* approach using which structured meshes can be generated for 2D domains that have non-orthogonal boundaries, such as in the present case, which contains both linear and hyperbolic shaped boundaries. After generating a structured mesh in each of these zones, the Steger-Sorenson [43] smoothening function (built-in function in Pointwise V18.4) is used at the interface between blocks b and c in order to make the cells orthogonal to the boundaries. This also generates a smoother transition between the blocks, as seen in Figure 2-5 (b).

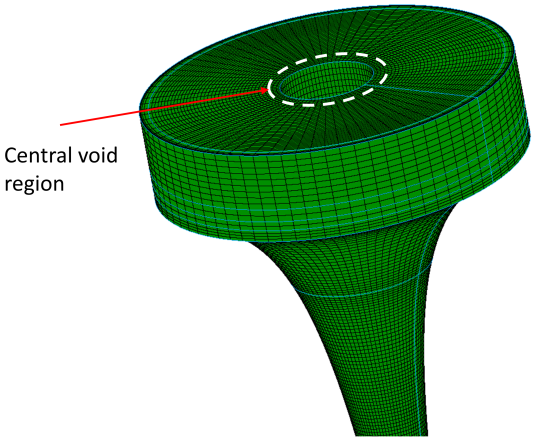

Figure 2-6: 3D radial mesh of Section I.

After generating the 2D mesh of Section I, it is swept around $AA^{'}$ as indicated by the arrow in the Figure 2-4 (a). This results in a radially structured mesh with a void in the central

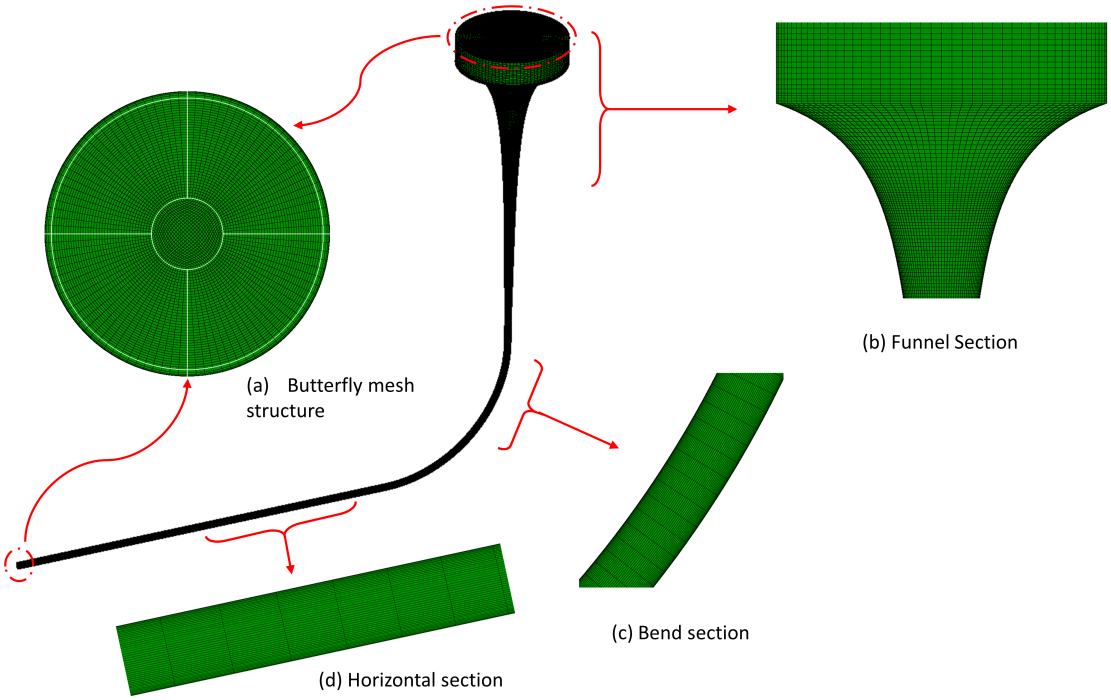

Figure 2-7: 3D structured mesh of the computational domain.

region as shown in Figure 2-6 (the image is zoomed to the upper portion of *funnel*).

The 3D mesh of Section II is divided into four equal volumes, generating corresponding four internal faces in the central void region. Using these faces as boundaries, a 3D cartesian mesh can be generated for Section I. Once the mesh for *funnel* section is generated, it can be extruded along the defined path (marked in red in Figure 2-2 (b)) to generate the complete mesh. Detailed views of the whole mesh are shown in Figure 2-7.

The main aim of the present study is to analyse the hydrodynamics of the vortex formed in the *funnel* section. The *extension* part is created in order to be able to define appropriate boundary conditions for the system. Resolving the flow field accurately in this region is not necessary. Accordingly, the meshing in the *extension* section is coarser (in other words, contains fewer number of cells) than the rest of the computational domain.

Using more nodes allows for better resolution of the flow field, but this comes at the cost of an increase in computational time. One of the primary requirements of a CFD study is to ensure that the results obtained are independent of the mesh used. In order to do that, the general practice is to simulate similar flow inputs (boundary conditions) on meshes of varying density. These different meshes are then compared based on specific physical parameters of interest and their associated computational times. Then a choice is made as to which mesh can be considered optimal for a particular study. In the present study, four different meshes are analysed for this purpose, and their details are given in Table 2-1.

Table 2-1: Meshes used for mesh independence study

S. No	Mesh name	Node count	Cell count
1	500k	495,000	507,620
2	1mil	1,085,440	1,105,716
3	2mil	1,994,675	2,023,896
4	3mil	3,020,440	3,057,147

2-3 Multiphase modelling

Vortices in hyperbolic funnels can be classified as a *free-surface flow* regime under gas-liquid flows of multiphase systems. The first step to numerical model these flows would be to choose in between the two approaches currently used for multiphase flows [41]:

- **Euler-Lagrangian approach:** In this model, the fluid is treated as a continuum while the secondary dispersed phase is solved by tracking each particle/bubble. The time-averaged Navier-Stokes equation solves the flow fields of the continuum phase and its interaction with the dispersed phase via mass, momentum and energy transfers. The main assumption made in this approach is that the volume occupied by the secondary /dispersed phase is much less than that of the continuum.
- **Euler-Euler approach:** Each phase is treated as a continuum whose flow fields are solved using conservation laws, and constitutive relations determine their interaction with each other. Their phasic volume fraction denotes the phases, and its overall sum for all phases in a given cell is equal to unity.

In the case of the present system, though in Restricted/Straight vortical regimes, the vortex core is less in volume than the surrounding vortex (Figure 1-1), it cannot be considered negligible. Moreover, tracking each particle of the secondary phase (i.e. air) throughout the domain is not practical, especially in the air core region that exists as a continuous phase. The Euler-Euler approach methodology is extensively used in simulating free-surface vortices, and aeration systems [44, 45, 46].

Based on how the interaction between phases is treated and the flow-regime under consideration, three different Euler-Euler methodologies are used: *Volume of Fluid (VOF), Mixture and Eulerian models.*

1. **Volume of Fluid model**
    - A technique for two or more immiscible fluids when determining the position of interface is of prime importance.
    - *Single-fluid approach* i.e. single momentum equation is solved for all the phases and volume fraction of each fluid is tracked throughout space and time.
    - Preferred for stratified/ free surface flows.

2. **Mixture model**

   - Suitable when phases mix/separate.
   - Solves momentum equation for the mixture, including relative velocities between the phases.
   - Preferred for simulating sedimentation, cyclone separators etc.

3. **Eulerian model**

   - Suitable when phases mix/separate.
   - Solves conservation laws for each phase in the domain, coupled through the pressure and interphase exchange coefficients. Computationally most expensive model.
   - Preferred for simulating bubble columns, risers, particle suspension etc.

Based on these guidelines, the VOF approach, which is capable of capturing the interface, is used in the present study and the same is also recommended in the works of [11, 47, 48, 42]. This approach is generally used for a time-dependent, or a transient system [41] in which each phase is represented by its phasic volume fraction (ϕ). The interface between the phases is tracked through space and time by a continuity equation.

$$\frac{\partial}{\partial t}\left(\phi_i \rho_i\right) + \boldsymbol{\nabla} \cdot \left(\phi_i \rho_i \boldsymbol{u}_i\right) = 0 \tag{2-1}$$

Here, i refers to the phases. Representing the liquid and gas phases by subscripts (l, g) the sum of phasic volume fractions can be written as

$$\sum_{k=1}^{n} \left(\phi_{l,k} + \phi_{g,k}\right) = 1 \tag{2-2}$$

Where n denotes the number of cells in the computational domain. A cell is completely filled with liquid if $\phi_L = 1$ or with gas if $\phi_L = 0$. An intermediate value of ϕ_L for a cell implies that it is an interfacial region between the phases.

An implicit volume formulation is used since the transient evolution of vortex is not of importance in the present study [49]. This approach allows the use of a larger time step as compared to the explicit formulation. The implicit discretization of continuity equation 2-1 is given by

$$\frac{\phi_g^{t+\Delta t}\rho_g^{t+\Delta t} - \phi_g^t \rho_g^t}{\Delta t} V + \sum_{k=1}^{t+\Delta t} \left(\rho_g \boldsymbol{u}_l^{t+\Delta t} \phi_{g,k}^{t+\Delta t}\right) = 0 \tag{2-3}$$

Here V refers to the volume of each cell. The VOF model allows for using a Pressure-based solver only. This is suitable for vortices in hyperbolic funnels with flow being nearly incompressible at the operating conditions.

The effects of surface tension are neglected in the present simulation based on Weber number criteria [41]. Also, its effect on strong free surfaces is negligible [13, 42]. Moreover, a single working fluid is used in the present study, and hence the dependence of the vortex structure on this fluid property is not analysed.

2-4 Turbulence modelling

The Navier-Stokes equations 1-9 to 1-12 can be represented in the general coordinate system as

$$\frac{\partial u_i}{\partial x_i} = 0 \tag{2-4}$$

$$\frac{\partial u_i}{\partial t} + \frac{\partial}{\partial x_j}\left(u_j u_i\right) = -\frac{1}{\rho}\frac{\partial p}{\partial x_i} + \frac{\partial}{\partial x_j}\left(2\upsilon s_{ij}\right) \tag{2-5}$$

Here, u_i's refer to velocity in each of the three mutually perpendicular coordinates, and $s_{i,j}$ refers to the strain rate tensor.

$$s_{ij} = \frac{1}{2}\left(\frac{\partial u_i}{\partial x_j} + \frac{\partial u_j}{\partial x_i}\right) \tag{2-6}$$

Turbulence develops due to instabilities in a laminar flow and is characterised by velocity fluctuations. This, in turn, results in fluctuations of transported quantities (momentum, species transport, energy etc.) across space and time. Fluctuations in flow fields occur at very small scales and high frequencies. The difficulties associated with modelling turbulent flow fields arise due to the broad length spectrum and associated time scales that these turbulent motions encompass. Stability in numerical modelling of curving turbulent flows (like vortices) is highly dependent on the choice of turbulence model.

2-4-1 Direct Numerical Simulations (DNS)

The Navier-Stokes equations could be directly used to compute the flow fields by resolving the domain at every spatial (i.e., the Kolmogorov scale to the integral length scale) and temporal scale. This approach is referred to as Direct Numerical Simulation (DNS). The computational time scales with Re^3 [50], and hence for most engineering problems, including the present system, this approach would be computationally costly. Use of DNS is limited for flows with low to moderate Re.

2-4-2 Reynolds Averaged Navier Stokes Equation (RANS)

In this approach, using the using Reynolds decomposition [51] the flow variables are viewed as a superimposition of their mean $(\boldsymbol{U}, P)$ and fluctuating values $(\boldsymbol{u'}, p')$.

$$\boldsymbol{u} = \boldsymbol{U} + \boldsymbol{u'} \tag{2-7}$$

$$p = P + p' \tag{2-8}$$

Substituting these into equations 2-4 and 2-5 results in a set of equations referred to as the RANS equations

$$\frac{\partial U_i}{\partial x_i} = 0 \tag{2-9}$$

$$\frac{\partial U_i}{\partial t} + \frac{\partial}{\partial x_j}\left(U_j U_i\right) = -\frac{1}{\rho}\frac{\partial P}{\partial x_i} + \frac{\partial}{\partial x_j}\left(2\upsilon s_{ij}\right) - \frac{\partial}{\partial x_j}\left(\overline{u'_j u'_i}\right) \tag{2-10}$$

The reynolds averaging process leads to an additional stress term ($\overline{u_j' u_i'}$) namely, the *reynolds stress tensor*.

$$\overline{u_j' u_i'} = -\begin{pmatrix} \overline{u'u'} & \overline{u'v'} & \overline{u'w'} \\ \overline{v'u'} & \overline{v'v'} & \overline{v'w'} \\ \overline{w'u'} & \overline{w'v'} & \overline{w'w'} \end{pmatrix} \tag{2-11}$$

This is a symmetric tensor with six unknowns. This, along with the unknown flow parameters (three components of velocity and pressure), results in ten unknowns. In the RANS equations, the fluctuations in velocity ($\boldsymbol{u'}$) are represented in terms of the mean velocity profile ($\boldsymbol{U}$). Hence, RANS equations need additional closure modelling for which a suitable turbulence closure model is used.

As opposed to multiphase modelling, where guidelines for choosing a suitable model are available, choosing a turbulence closure model is highly problem-specific. These are broadly divided into

2-4-2-1 Eddy-Viscosity Models

These are first order models in which the role of turbulence is to increase the effective viscosity by addition of eddy/turbulent viscosity (μ_t). Boussinesq [52] hypothesised that Reynolds stress is proportional mean velocity gradients (derivation in Appendix D).

$$-\rho\overline{u_i' u_j'} = 2\mu_t\left(S_{ij} - \frac{1}{3}\frac{\partial U_k}{\partial x_k}\delta_{ij}\right) - \frac{2}{3}\rho k\delta_{ij} \tag{2-12}$$

Here k is the turbulent kinetic energy per unit mass and μ_t represents eddy viscosity. The Eddy-viscosity models in increasing order of computational costs are

1. Spalart-Allmaras model
2. k- ϵ model
    - Standard k- ϵ model
    - RNG k- ϵ model
    - Realizable k- ϵ model
3. k- ω model
    - Standard k- ω model
    - SST k- ω model

In the Spalart-Allmaras model, one additional transport equation representing μ_t is solved. However, being relatively new, the stability of this model for complex flows is not well established. The realisable k- ϵ model produces non-physical turbulent viscosity in situations when the computational domain contains both rotating and stationary fluid zones [49]. Hence both these methods are not used in the present study.

Standard k- ϵ or k- ω models solve two additional equations each for turbulent kinetic energy (k) and turbulence dissipation rate (ϵ) or the specific dissipation rate (ω). The turbulent

viscosity (μ_t) is expressed as their function. Although this approach is computationally less expensive, it does not account for the dependence of Reynolds stresses on the rotation rate in the flow, leading to overestimation of turbulence in the vortex core as observed [53]. It considers μ_t as an isotropic scalar quantity and hence in its present form, is not suitable for vortex simulations as also stated in the works of Rajendran et al. [54] and Sean Mulligan [11]. The RNG k- ϵ is an improvement over the standard k- ϵ model in which the effect of swirl on turbulence is taken into account. It performs better in accuracy than the standard k- ϵ model for simulating flows with high strain rates. This model is recommended over the standard k- ϵ turbulence model [53].

The Shear Stress Transport (SST) based k- ω model uses a blending function to simulate near-wall region using k- ω model and the k- ϵ model far away from it. This eliminates the need for extra damping functions in the near-wall region. It incorporates modifications in the turbulent viscosity (μ_t) to account for transport effects of turbulent shear stress. Curvature corrections can be applied to these models to account for rotational effects and increase the rate of dissipation in regions of curved streamlines. In simulating vortices with curvature correction enabled, Škerlava et al. [14] observed that the diameter of vortex cores formed were more realistic when curvature correction was used. Sean Mulligan [11] also noted a better tangential velocity profile using the k- ω based SST model with curvature corrections. The flow governing equations using k- ω SST model are given in Appendix B.

2-4-2-2 Reynolds Stress Models (RSM)

These are second-order models that solve individual transport equations for all the six Reynolds stress components and an additional equation for dissipation rate. It has better simulation capabilities for complex flows as it inherently considers the effects of rotation, streamlines curvature and rapid changes in strain rate. However, the increase in accuracy as compared to an appropriate eddy viscosity model like SST based k- ω was small and not justified in comparison to the increase in computational cost [11].

2-4-2-3 Large Eddy Simulations (LES)

Turbulent flows are characterised by eddies spanning over a large spectrum of length and time scales. The large scales eddies transport a significant portion of momentum, mass and energy while the turbulent kinetic energy (k) is mainly dissipated at the smaller scales, which are nearly isotropic. In LES simulations, as the name suggests, large scale eddies are resolved directly while small scale eddies, also referred to as the sub-grid scales are modelled using the subgrid-scale model to obtain closure. In this way, the error introduced by turbulence modelling is relatively reduced. LES simulations are computationally more expensive than the RANS simulations.

A variable (φ) is filtered ($\tilde{\varphi}$) based on the length scale of eddies as represented by equation 2-13, where D is the fluid domain and G is the filter function

$$\tilde{\varphi}(x) = \int_D \varphi\left(x'\right) G\left(x, x'\right) dx' \tag{2-13}$$

The variables are decomposed into their large (above the filter length scales) and small scale features (below the filter length scales)

$$u_i = \tilde{u}_i + u_i' \tag{2-14}$$

$$p = \tilde{p} + p' \tag{2-15}$$

These, when substituted into the Navier Stokes equations 2-4 and 2-5), leads to filtered continuity and momentum equations.

$$\frac{\partial \tilde{u}_i}{\partial x_i} = 0 \tag{2-16}$$

$$\frac{\partial}{\partial x_j}\left(\rho \bar{u}_i \bar{u}_j\right) = \frac{\partial}{\partial x_j}\left(\sigma_{ij}\right) - \frac{\partial \bar{p}}{\partial x_i} - \frac{\partial \tau_{ij}}{\partial x_j} \tag{2-17}$$

The term τ_{ij} is referred to as the subgrid-scale Reynolds stress, and σ_{ij} is the molecular viscosity induced stress tensor defined by

$$\tau_{ij} = \left(\widetilde{u_i u_j} - \tilde{u}_i \tilde{u}_j\right) \tag{2-18}$$

$$\sigma_{ij} \equiv \left[\mu\left(\frac{\partial \bar{u}_i}{\partial x_j} + \frac{\partial \bar{u}_j}{\partial x_i}\right)\right] - \frac{2}{3}\mu \frac{\partial \bar{u}_l}{\partial x_l}\delta_{ij} \tag{2-19}$$

Fluent adopts the Boussinesq hypothesis [55] to model the subgrid scale reynolds stress term

$$\tau_{ij} - \frac{1}{3}\tau_{kk}\delta_{ij} = -2\mu_t \tilde{S}_{ij} \tag{2-20}$$

Here, μ_t is the subgrid-scale turbulent viscosity and $\tilde{S}_{ij}$ is the rate of strain tensor at the filtered length scale.

While simulating 3D vortical structures, Tokyay et al. [56] used the LES approach and compared the results obtained with those from the SST based k- ω model. It was observed that although both SST and LES generated qualitatively similar results, the ones obtained from LES were quantitatively more accurate. However, the SST models take a fraction of the computational time needed for LES simulations. Considering the time duration of the present study, the computational cost associated with performing an LES simulation did not seem justifiable. Hence, the SST based $k - \omega$ model with curvature correction is used.

2-5 Boundary conditions

There are three BCs for the present system as indicated in Figure 2-2, i.e. the *Water Inlet*, the *Air Vent* and the *Outlet*. Water enters the system through the *Water Inlet* on the top cylindrical portion and exits via the *Outlet* face. Initially, the system is in a transient state during which the vortex is not sustained due to the rapid draining of water. As water (and its associated circulation) continuously enters the system, a stable vortex structure forms, which is statically steady[1]. *Air vent* on the top of the cylindrical portion facilitates atmospheric air to enter into the system due to the sub-pressures created in the central region of the vortex.

[1]The terms steady and statistically steady are used interchangeably in the present study. Both these terms refer to the statistical steady state of the vortex formed in the hyperbolic funnel.

2-5-1 Water inlet

Different configurations of *Water inlet* were analysed in this study. The reason for modelling water inlet as a patch on the cylindrical portion instead of an inlet tube as in experiments (Figure 2-8 (a)) was explained in Section 2-2-1. As the vortex formation is essentially independent of the exact location of the water inlet and primarily depends on the inlet flow rate of water, the *Water inlet* can be modelled as a region all along the circumference of the cylindrical portion (Figure 2-8 (b)). This would lead to a symmetric inflow BC which is preferred in CFD.

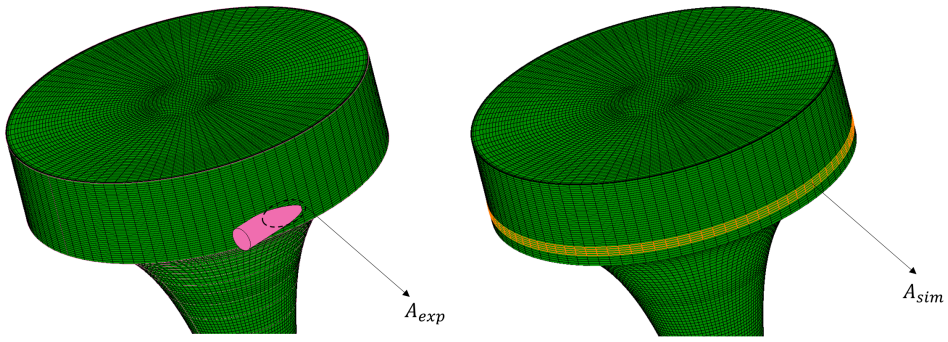

(a) Water Inlet tube as in experiments

(b) Water Inlet modelled along the cylindrical portion

Figure 2-8: Modelling of *Water Inlet*.

An essential requirement to model the experimental conditions would be to ensure that the rate of kinetic energy ($\dot{KE}$) entering the system should be the same in both the experiments and the simulations performed. For experiments (exp) the inlet kinetic energy rate can be written as

$$\dot{KE}_{exp} = \frac{1}{2}\dot{m}_{exp}|\boldsymbol{u}|^2 \tag{2-21}$$

Where $\dot{m}_{\text{exp}}$ represents the experimental inlet mass flow rate and $|\boldsymbol{u}|$ denotes the magnitude of inlet velocity for water. Considering the area of intersection of the inlet tube with the cylindrical portion of the funnel as A_{exp}, from mass conservation the magnitude of inlet velocity can be determined ($|\boldsymbol{u}| = \dot{m}_{exp}/\rho A_{exp}$). Substituting this into equation 2-21 yields

$$\dot{KE}_{exp} = \frac{1}{2}\frac{\dot{m}_{exp}^3}{(\rho A_{exp})^2} \tag{2-22}$$

Similarly for simulation considering the area of circumferential inlet (Figure 2-8 (b)) as A_{sim} and water inlet flow rate as $\dot{m}_{sim}$, the rate of inlet kinetic energy is

$$\dot{KE}_{sim} = \frac{1}{2}\frac{\dot{m}_{sim}^3}{(\rho A_{sim})^2} \tag{2-23}$$

Equating equation 2-22 and 2-23 yields

$$\dot{m}_{\text{sim}} = \dot{m}_{\text{exp}}\left[\frac{A_{\text{sim}}}{A_{exp}}\right]^{2/3} \tag{2-24}$$

In order to make A_{sim} equal to A_{exp} height of each cell in that region needs to be 8e-04 m which is around five times smaller than the minimum mesh height in the *500k* mesh. Even if the corresponding mass flow rate ($\dot{m}_{sim}$ from equation 2-24) were given as an input in the simulations, this would create artificial mass to be present in the system.

In order to be able to replicate the experimental inlet conditions, the *Water inlet* is modelled as *Mass Flow Inlet* in a region on the cylindrical portion. This has an area which is approximately equal to A_{exp} ensuring that $\dot{KE}_{sim}$ is equal to $\dot{KE}_{exp}$. Also, the direction of the water inlet is specified to be 30% along the radially inward direction and 70% along the tangential direction (anti-clockwise direction as viewed from the top of *funnel*). These angles are obtained from CAD models (Figure 2-8 (a)).

2-5-2 Air vent

The *Air vent* is modelled as a rectangular region on the top of the cylindrical portion as shown in Figure 2-9 (a). In this study, the size of the air-vent was varied (Figure 2-9 (b)), and it is observed that the surface area of the air vent does not affect the vortex structure formed. Its area would influence only the initial velocity with which the air enters the system. However, this influence is limited to a small volume near the *Air vent*, and the velocity of air travelling downwards via the air-core is dependent on sub-pressures created by the circulatory forces of water.

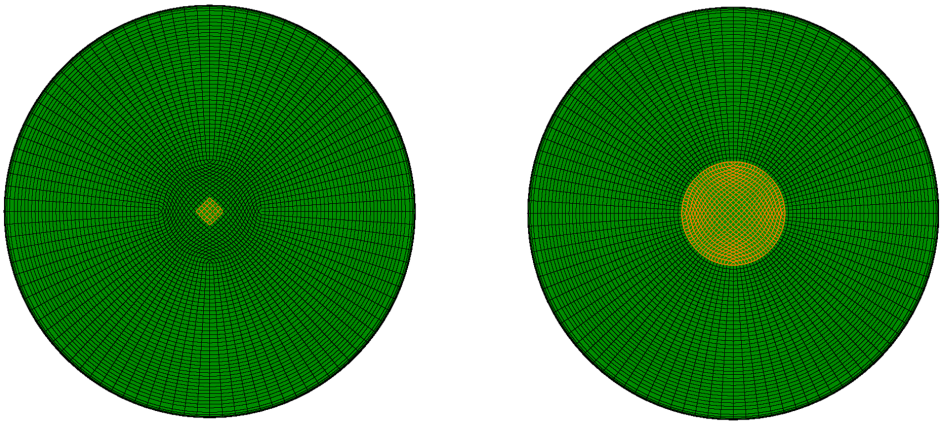

(a) Rectangular (2 cm^2) (b) Circular (44 cm^2)

Figure 2-9: *Air vent* geometries.

Intuitively, *Air vent* would be defined as a Pressure Inlet boundary condition [41] whose input is the gauge total pressure (P_o) defined as

$$P_0 = P_s + \frac{1}{2}\rho|\boldsymbol{u}|^2 \tag{2-25}$$

Here P_s is the static gauge pressure at that location whose value is 0 Pa (i.e. atmospheric pressure of 101325 Pa). The velocity ($|\boldsymbol{u}|$) with which it enters is dependent on sub-pressures created by the vortex formation and hence its dynamic pressure ($1/2\rho|\boldsymbol{u}|^2$) at this location is not known. So the *pressure inlet* boundary condition is not an appropriate choice. On the

other hand, a Pressure Outlet boundary condition requires only P_s as its input. It must be noted that the CFD solver displays a warning message upon detecting *reversed flow* at this BC since flow is entering the system through it. However, this does not affect the stability of the numerical scheme, and physically correct flow is simulated.

2-5-3 Outlet

This is the exit BC of the computational domain, where a mixture of water and air leaves the system. Different boundary conditions in Fluent [41] and two different locations for this BC (indicated by Location I and Location II in Figure 2-10) were investigated in order to make an appropriate choice for this BC.

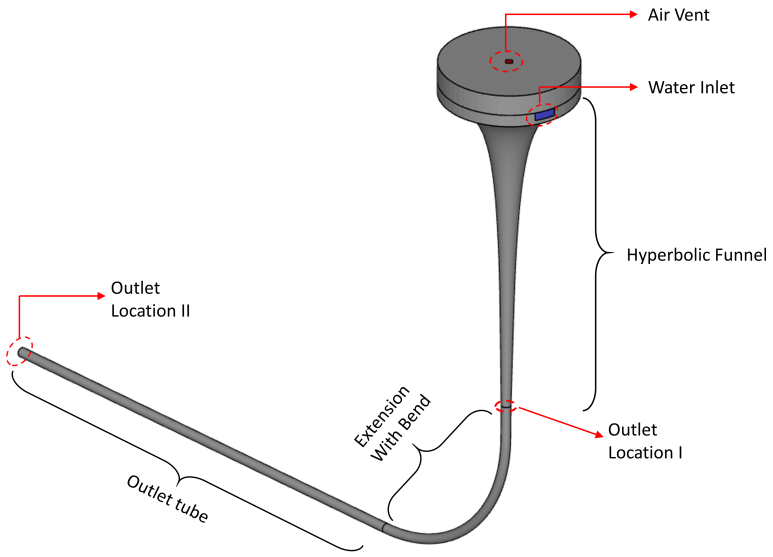

Figure 2-10: Locations for *Outlet* BC.

2-5-3-1 Pressure outlet

From experimental measurements, the pressure sensor beneath the funnel (Figure A-1), i.e. at Location II in Figure 2-10 gives the average value of static pressure (P_s) at this location. Using this, Location I was assigned as Pressure Outlet BC. The volume fraction contour at steady-state obtained with flow conditions corresponding to Twisted regime (flow rate of 20.4 L/min and static pressure value of 118 Pa [1]) is shown in Figure 2-11. The region in blue represents water, while the region in red indicates the 3D iso-surface of the air-water interface.

It can be clearly seen that the amount of water is present in the system is quite low in comparison to the experimental observations (Figure 1-1 (b)). Also, the interface lacks the helical structure, which is a typical characteristic of the Twisted vortical regime. The reason for this anomaly is because the static pressure (P_s) is defined as a constant value across the cross-sectional area of Location I.

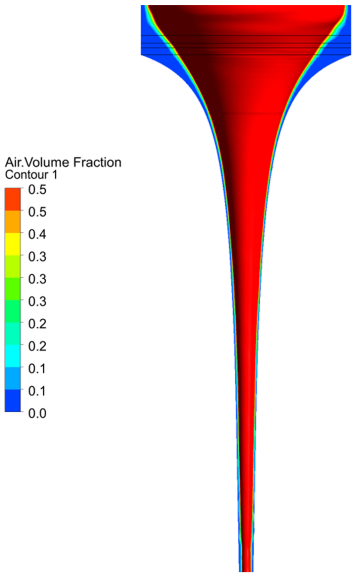

Figure 2-11: Volume fraction contour of air for the Twisted regime with Pressure Outlet BC at Location I.

The *Eulers equation* normal ($\hat{n}$) to the streamwise coordinates is given by (derivation in Appendix C)

$$\rho \frac{\boldsymbol{u}^2(s)}{R(s)} \hat{n} = -\frac{dP}{dn} \tag{2-26}$$

Here s represent the velocity component along the streamwise direction, and R represents the radius of curvature of streamlines. This equation implies that at a given sectional plane, that is normal to the streamwise direction, only when the streamlines are parallel to each other (i.e. the radius of curvature is infinity making LHS tend to zero) will the gradients of pressure along the normal direction (i.e. along the cross-section) be zero. This then leads to a uniform static pressure distribution across that face.

Using a Pressure Outlet BC at Location I would imply that the streamlines are artificially forced to be parallel to that face, i.e. velocity along with the radial and tangential directions (u_r and u_θ) are forced to be zero. However, as it can be seen in the experimental images of the Twisted and the Straight regimes (Figure 1-1), the air core is extending beyond the Location I. This implies that the circulatory forces still exist in the fluid at this location, i.e. u_θ is a non-zero value.

The static pressure at Location I is expected to have radial distribution with a minimum at the centre of the cross-section due to the sub-pressure induced by the circulatory forces of water. Moreover, the air-core vortex with its asymmetric 3D shape exhibits a statically steady behaviour. Implementing a user-defined function (UDF) for static pressure at this location is difficult as it varies as a function of both space and time.

Hence assigning a Pressure Outlet BC at Location I is not appropriate, and its applicability at Location II will be discussed in Section 2-5-3-3.

2-5-3-2 Mass-flow outlet

This boundary condition requires the net mass leaving the computational domain as an input. Although the inlet flow rate of water through *Water Inlet* BC is known, the mass of air entering the system via *Air vent* is unknown. A UDF can be specified such that the mass of air leaving the system via the *Outlet* be equal to the mass of air entering the system via *Air vent*. Mass-flow outlet BCs in Fluent is modelled by dividing the mass flow rate by the area of the face resulting in a uniform mass flux leaving that face. In order to use a Mass-flow outlet BC either at Location I or II, these faces would have to be split into two divisions for each phase. However, the precise shape and area of these divisions are unknown, and hence this is not an appropriate boundary condition for the system at both these locations.

2-5-3-3 Outflow

The flow field distribution (velocity and pressure) is not known at both Locations I and II. This results in assigning a boundary condition at this face challenging compared to the other two BCs. In Fluent, the Outflow BC is used in such situations. This BC makes certain assumptions [49]:

1. No Pressure inlet BC in the system.
2. Flow is incompressible.
3. Zero diffusion fluxes for all flow variables in the direction normal to exit face.

Conditions 1 and 2 are inherently satisfied in the present case. Condition 3 implies that gradients of velocity along the direction normal to the *Outlet* face are zero (region of fully developed flow), and the flow is strictly exiting the domain through this face (no reversed flow). Since the gradients of velocity normal to the face are assumed to be zero, the flow variables are calculated based on this criterion from interior cells satisfying mass conservation. This can also be used at a location where such a fully developed flow assumption would not significantly affect the physics in the domain of interest, i.e. *funnel* section in the present study.

The applicability of Outflow BC were analysed at both Locations I and II. When used at Location I, it causes the system to be numerically unstable, leading to divergence. The reason for this is that at Location I, the flow is accelerating due to gravity (along negative $\hat{e}_z$) and also due to the change in radius of the funnel along this direction (by conservation of angular momentum). Hence the gradients of velocity at Location I along $\hat{e}_z$ are not zero.

At Location II the effects of gravity are not present. Also, since the cross-section area of the tube is constant, there are no gradients in velocity due to this factor as well. However, the difference in pressure between the point after the bend and Location II might cause the flow to accelerate. If the tube is made sufficiently large such that the changes in gradients of pressure along the flow direction are minimal after a given length, then gradients in velocity are also negligible. The longer the horizontal section, the more valid is this assumption and consequently the applicability of Outflow BC at Location II.

Although the flow is not fully developed at Location II and this assumption would lead to few discrepancies at the exit face, this would not affect the vortex that is formed in the *funnel* section. The validity of this assumption will be discussed further in Section 2-7. An Outflow BC does not lead to constant static pressure (P_s) at a given face since gradients normal to the streamlines (i.e. along the face) might still exist even in a fully (or nearly) fully developed flow field. This is the reason that assigning a constant static pressure using a Pressure Outlet BC at Location II is not valid.

The assumption of flow being nearly fully developed at Location II is valid only when the system reaches its steady state. This assumption is invalid during the transient phase when the vortex is still forming. Hence the *Outlet* BC is initially defined as a Pressure outlet (increasing the magnitude of P_s as the vortex develops), and as the flow field reaches a fully developed condition at the exit, it is switched to an Outflow BC. The procedure for this will be dealt in the subsequent section. The BCs are summarised in Table 2-2 along with their respective inputs.

Table 2-2: Boundary conditions

Boundary	Type	Variables	Symbol
Water inlet	Mass flow inlet	Flow rate (water)	$\dot{m}_{water,in}$
		Tangential component	t
		Radial component	r
Air vent	Pressure outlet	Static gauge pressure	$P_{s,a}$
Outlet	Pressure outlet	Static gauge pressure	$P_{s,w}$
	Outflow	-	-

2-6 Solution methods

Simulations are performed using a Pressure-based solver since the density of both the phases is assumed to be constant at the operating conditions. The velocity ($\boldsymbol{u}$) and the pressure field (P) are solved numerically using equations 1-9 and 1-12. This is referred to as Pressure-Velocity Coupling in CFD. It can be achieved in a segregate manner (SIMPLE, SIMPLEC, PISO) in which they are updated sequentially or simultaneously, as in Coupled schemes. PISO and Coupled schemes are recommended for swirling flows. The Coupled algorithm is used in the present study since it tends to be more robust while using a larger time step.

Lease squares cell-based method is used for Gradient Spatial Discretization since it is less computationally expensive in comparison to the Node-based gradients. Although the Green-Gauss Cell-Based method is the least expensive method, it is prone to false numerical diffusion. The PRESTO scheme is used for Pressure interpolation at cell faces due to the presence of strongly curved domain (*funnel*) and tangential velocities.

A second-order upwind scheme is used for Momentum discretisation as the flow is not entirely aligned with the mesh and the use of a first-order method leads to an increase in numerical diffusion in such cases. An implicit scheme is used for VOF, and the interface is modelled as sharp/dispersed. The reason for choosing this over a sharp interface modelling is that at the

end of the funnel section air-core abruptly ends, and the interface is not sharp (to be further discussed in Section 3-2). A compressive advective scheme is used for volume fraction spatial discretisation. First-Order Upwind methods are used for both Turbulent Kinetic Energy and Specific Dissipation Rates.

The transient formulation is done using the Bounded Second-Order Implicit scheme to improve the numerical stability while using larger time steps due to the boundedness of variables (like turbulent kinetic energy) in the domain. Also, its accuracy is comparable to the second-order central differencing schemes.

Comprehensive mathematical treatment of these methods can be found in [41]. All the Fluent settings are summarised in Appendix D.

2-7 Simulation strategy

Once the system is initialised using the *Hybrid initialisation* method, it is completely filled with water by the *patch function* (in-built function in Fluent). This sets the phase fraction of the water phase at 1 in all the cells. In case water is not present in the system at the start of the simulation, it leads to numerical instabilities. The reason for this is that in such a case, initially, the water entering the computational domain through the *Water inlet* accelerates (both due to changing radius of curvature and gravity). The interface between air and water does not behave like a free surface or stratified flow, and such interfaces are not accurately tracked by the VOF approach [41]. On the other hand, when water is initially present in the system, the incoming water (and its associated circulation) transfers its kinetic energy to the already present water in the system, creating a rotating flow field in the top cylindrical part. As the water starts draining out via the *Outlet* face (which is initially a Pressure Outlet), this rotating fluid slowly begins to spiral down, creating a vortex structure.

The initial inputs to the system are (for Twisted regime):

1. $\dot{m}_{water,in} = 21.5$ L/min ($t = 0.7$, $r = 0.3$).
2. $P_{s,a} = 0$ Pa.
3. $P_{s,out} = 0$ Pa.

Considering the whole system as a control volume, the mass conservation (equation 1-9) can be re-written as

$$\dot{m}_{net} = \dot{m}_{in} - \dot{m}_{out} = (\dot{m}_{\text{water,in}} + \dot{m}_{\text{air,in}}) - (\dot{m}_{\text{water,out}} + \dot{m}_{\text{air,out}}) \tag{2-27}$$

Here, $\dot{m}_{net}$ refers to the net mass flow rate through the computational domain which is equal to the difference between mass of air (via *Air vent*) and water (via *Water inlet*) entering and leaving (via *Outlet*) the system. This is monitored with time as shown in Figure 2-12. As $\dot{m}_{net}$ approaches zero, it implies that the system has reached its statistically steady state. As the whole domain is entirely filled with water, hydrostatic forces are higher than the circulatory forces, making the water drain rapidly at the start of the simulation. This is evident from the high negative value of $\dot{m}_{net}$ at the start of the simulation. As more mass of water enters into

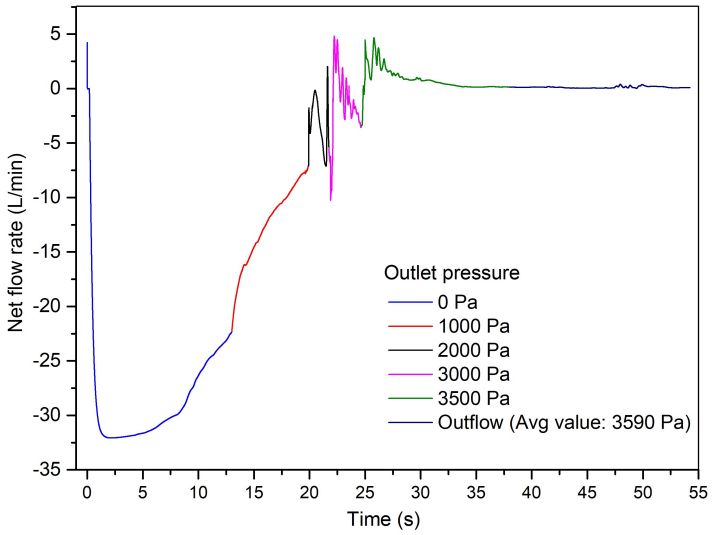

Figure 2-12: Net mass flow rate through the computational domain.

the system, the net outflow decreases in magnitude due to an increase in rotational energy of the fluid.

Figure 2-12 shows the contours of volume fraction on a 2D section defined in r - z plane in the top portion of *funnel* section with time. Air enters the system due to two reasons

1. Initial excessive draining of water due to high $\dot{m}_{water,out}$ which is compensated by $\dot{m}_{air,in}$ since $\dot{m}_{water,in}$ is a fixed value.

2. The sub-pressures created as the vortical structure forms in the domain.

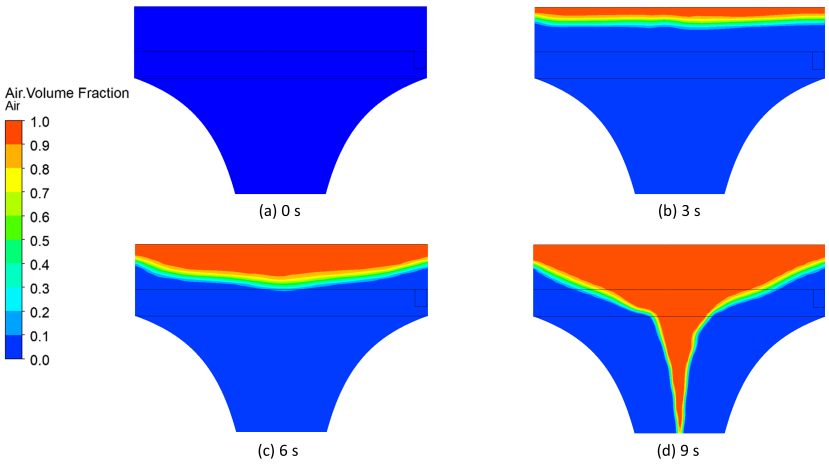

Figure 2-13: Transient evolution of vortex on a 2D sectional plane ($r - z$).

These two factors increase the amount of air that enters the system initially. As the system reaches its statistically steady state, the net water flow rate approaches zero, making the contribution from factor 1 also zero. At this condition, air entering the system is purely due

to factor 2. With time as the fluid spirals down, the air core vortex increases in volume, as seen at different time instants in Figure 2-13.

In Figure 2-12 after around 1s (with $P_{s,out}$ - 0 Pa), there is an increase in the net flow rate through the system. However, if left at that value of $P_{s,out}$, the system diverges after around 13s. This is because mass conservation is not satisfied in the horizontal part of the *extension* section. After the *funnel* section, the fluid travels through the extension with the bend, the outlet tubes and exits via the Outlet face (Figure 2-10). The presence of a bend increases the pressure locally in that region; let this be denoted by P_{bend} and the static pressure at the *Outlet* face is defined as $P_{s,out}$. The difference of pressure in the horizontal section is proportional to its length (L_{tube}) in addition its radius and mass flow rate

$$\Delta P = P_{\text{bend}} - P_{s,\text{ out}} \propto L_{\text{tube}} \tag{2-28}$$

Therefore $P_{s,out}$ is a unique value depending on the flow conditions in the system and system dimensions. Setting this to that unique value is essential to satisfy mass conservation in the system. Less than the unique value causes draining of the fluid, and more than the unique value leads to the build of mass in the system. In either way, it causes numerical instabilities and leads to divergence.

The outlet pressure is iteratively increased in the simulation (from 0 Pa to 3500) Pa as seen in Figure 2-12. At 3500 Pa, the system achieves a statistical steady state (no net flow rate through the system). However, there is tangential velocity still present in the flow field at the Outlet face, and hence for reasons discussed in Section 2-5-3-1 a constant pressure condition would lead to physical inaccuracies in this region. Hence, after the system reaches its steady-state, the *Outlet* BC is switched from Pressure Outlet to Outflow. Although the flow is not entirely fully developed at this point, such an assumption does not to cause any changes in the vortex structure that is formed inside the *funnel*. This is verified by monitoring the air-volume fraction, interfacial area and the maximum tangential velocities in the *funnel* section before and after the BC is switched to Outflow. This only difference observed is in the region near to the Outlet face as seen in Figure 2-14.

(a) Pressure Outlet BC (3500 Pa)

(b) Outflow Boundary condition

Figure 2-14: Streamlines in the outlet tube (*Outlet* BC is on the left).

It can be seen that when the *Outlet* is defined as a Pressure outlet BC, the streamlines near to the Outlet face (left end of Figure 2-14) are artificially forced to be parallel to this face. This is consistent with the reasoning in Section 2-5-3-1. On the other hand, when an *Outflow* BC is used, the streamlines are curving, which is indicative of the presence of tangential velocities at this location, and this is physically expected. On average, the pressure across the face increases by around 390 Pa upon switching to *Outflow* BC to accommodate for the presence of these tangential velocities. The tangential velocity in the form of vectors of the system at

this face is represented in Figure 2-15. It can be seen that when a constant pressure boundary condition is used, the flow seems to be un-physical with more than the one axis around which there this circulation, whereas an Outflow BC keeps the axis of rotation of the fluid consistent with the flow field behaviour.

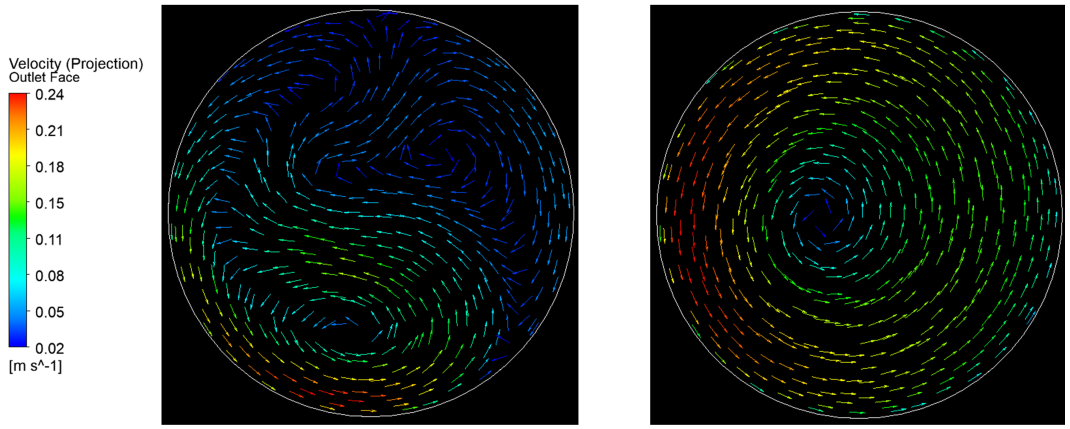

(a) Pressure Outlet BC (b) Outflow BC

Figure 2-15: Tangential velocity vectors at the *Outlet* face.

Chapter 3

Results and discussion

The CFD simulations are performed on ANSYS-Fluent 19R3 using the computational resources of the Process & Energy department, TU Delft.

3-1 Mesh independence study

For the mesh independence study, a particular flow rate of water corresponding to the Twisted regime (21.5 L/min) was chosen to form a vortex structure on the four different meshes in Table 2-1. In order to save time, the flow variables are extrapolated from the steady-state condition of one mesh to the next higher mesh, i.e. from *500k* to the *1mil* mesh and so on. Also, for every 40000 cells, one core was used to make the parallel computation process efficient. Table 3-1 shows the number of cores used for each mesh and their respective computational times.

Table 3-1: Computation time for different meshes

Mesh	Cores	Nodes	Computational time (days)
500k	13	1	2.4
1mil	28	1	4.8
2mil	56	2	7.4
3mil	56	2	14.3

Figure 3-1 shows the tangential velocity plotted on a 2D sectional plane (r-z) of the hyperbolic funnel and 3D iso-surface of the air-water interface. These meshes primarily differ in the resolution of the interface. In the case of *500k* mesh, the interface looks relatively flat on the bottom with no helical profile as seen in the experiments (Figure 1-1 (b)). As the mesh is made finer, the resolution of this interface improves. The reason for this is that the VOF approach uses a piecewise linear interface calculation (PLIC) technique [41] for continuity equation (equation 2-1) to reconstruct the interface in each cell. This models the interface as

a plane in each 3D cell. Hence, capturing a highly curved interface requires that a sufficient number of cells be present in the computational domain [57] in order to reconstruct the helical profile as a combination of linear parts.

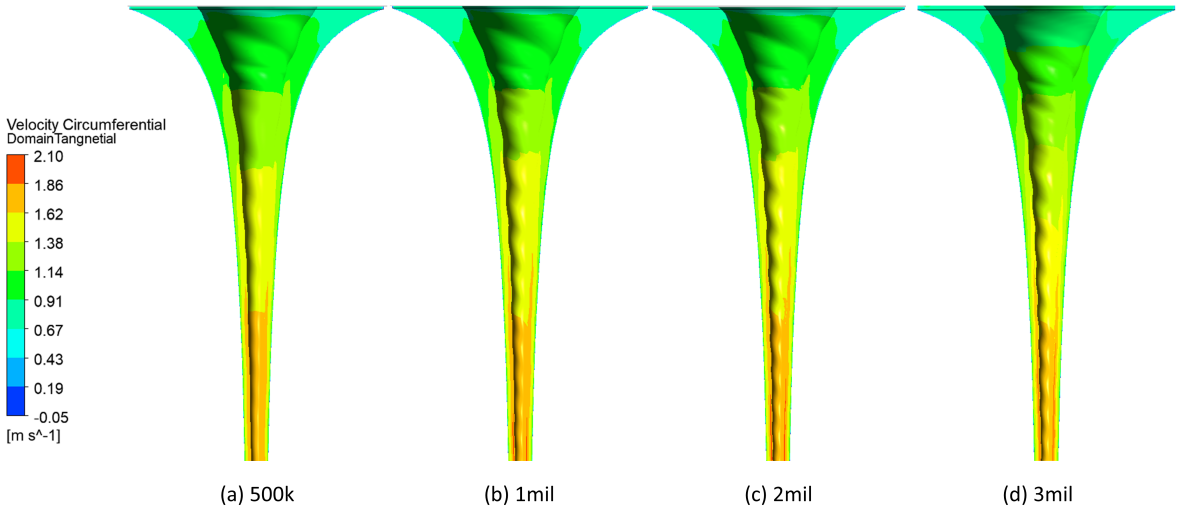

Figure 3-1: Tangential velocity on a 2D sectional plane and 3D iso-surface of air-water interface.

The parameters of interest are measured in the *funnel* section since its hydrodynamics is of importance in the present study. The chosen parameters are:

1. **Air-fraction** (V_{air}): The volume fraction of air in the *funnel* section is one of the distinguishing features of different regimes as seen in Figure 1-1.
2. **Air-water interfacial area** (A_{int}): This parameter is important since it directly influences the rate of gas-transfer into the system (equation 1-3).
3. **Average exit static pressure** ($P_{exit,avg}$): This is measured at the end face of the *funnel* section and quantifies the pressure differential (with *Air vent* at atmospheric conditions) created in the *funnel* due to the vortex formation.

Table 3-2: Parameters of interest on different meshes

Mesh	V_{air}(%)	Change (%)	$A_{int}(cm^2)$	Change (%)	$P_{exit,avg}$ (Pa)	Change (%)
500k	53.93		1551.83		1397.31	
1mil	50.27	6.78	1470.67	5.23	1458.21	4.36
2mil	49.19	2.15	1415.08	3.78	1493.1	2.39
3mil	48.31	1.79	1384.8	2.14	1508.62	1.04

Table 3-2 compares the steady-state values of these parameters for each mesh. The change in values between *1mil* and *2mil* meshes is less than 5% for all the variables, and this difference reduces further on going to the *3mil* mesh. However, considering the computational time of around 14 days for *3mil* mesh (Table 3-1) and the time available for the present study, the *2mil* mesh is used for simulations and analysis. In the present study, the Restricted regime is not simulated since it is formed by constricting the outlet tubes beneath the *funnel* in experiments. The quantitative reduction in the area was not known with certainty.

3-2 Validation

Simulations are performed for flow rates corresponding to Twisted[1] (20.9 L/min and 21.5 L/min) and Straight (22.5 L/min) regimes on the *2mil* mesh. The obtained vortical structures are shown in Figures 3-2 and 3-3. The experimental images are also represented on the left of each figure in which the vortical structure on the top cylindrical portion is not properly captured since the glass is highly curving at this section leading to reflection.

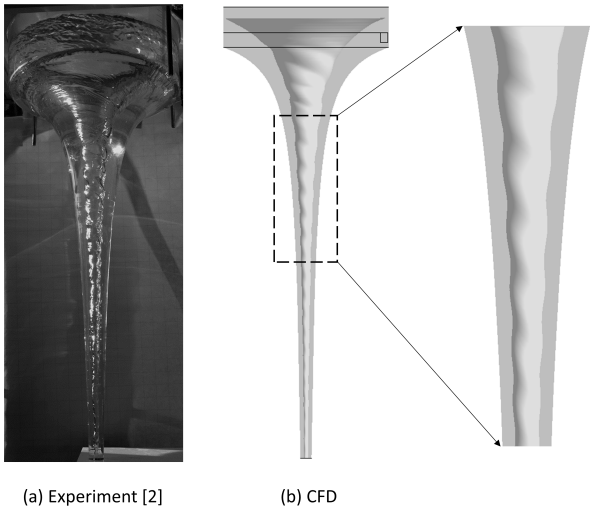

Figure 3-2: Comparison of vortical structure for the Twisted regime (20.9 L/min).

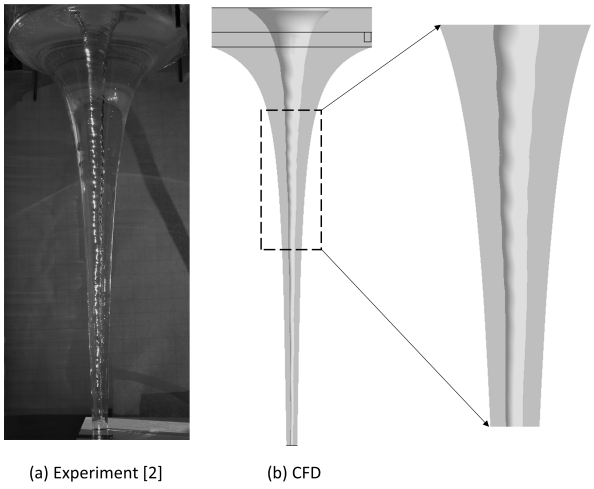

Figure 3-3: Comparison of vortical structure for the Straight regime (22.5 L/min).

Qualitatively, the CFD results can reproduce the experimental vortical structures well, as seen in these figures by the shape of the air-water interface and the volume of the air core formed. The wavy profile on the interface is also well captured in the CFD results.

[1] 20.9 L/min is used for validation with experimental data while 21.5 L/min is used for further analysis and comparison with Straight regimes. PIV data from experiments were available for 21.5 L/min, but this was not completed due to the time available for the present study.

In order to validate the numerical results obtained, the radial position of the air-water interface along the axial distance of *funnel* was compared with experimental data. The average interfacial position at a given axial height from the experimental images was manually extracted using an open-source software [58]. The comparison for both regimes is shown in Figures 3-4 and 3-5.

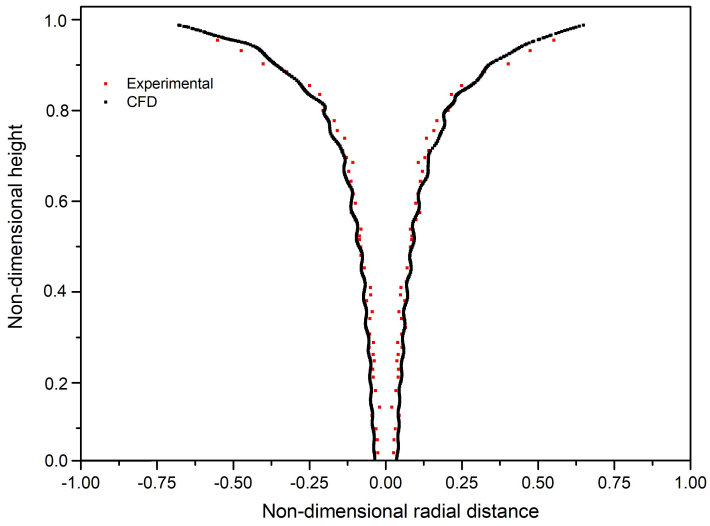

Figure 3-4: Comparison of the air-water interface position between experiments and CFD for the Twisted regime (20.9 L/min).

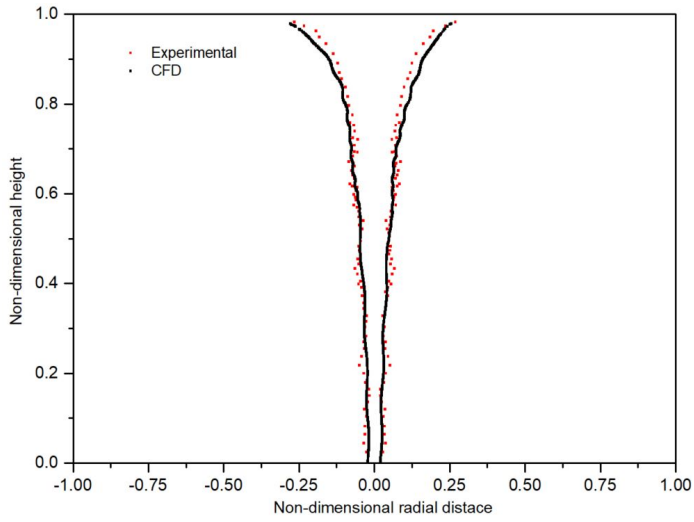

Figure 3-5: Comparison of the air-water interface position between experiments and CFD for the Straight regime (22.5 L/min).

The interface position is well captured by using the SST based k-ω turbulence model with curvature correction as also noted in other research works on vortices by [11, 14]. The air-core diameter varies along the axial direction mimicking the shape of the hyperbolically shaped boundary. This shape is less dominant in the Straight regime due to the higher flow rate of water which results in higher water volume fractions in the *funnel* section.

Figure 3-6 shows a comparison between experimental and numerical results with respect to the air-water interface in the bottom portion of the funnel. It can be seen that the interface looks relatively flat in numerical results in comparison to experiments for both the regimes.

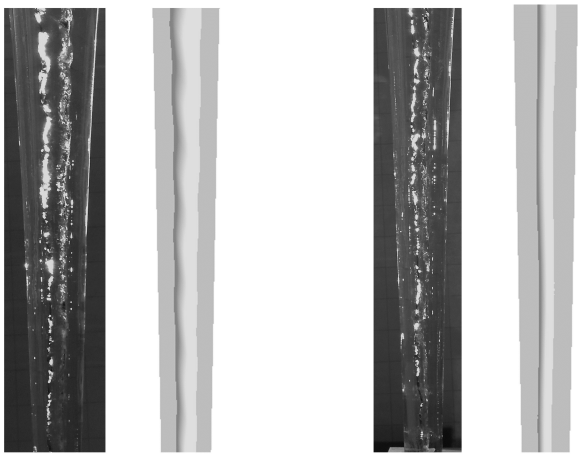

(a) Twisted (b) Straight

Figure 3-6: Air-water interface in the bottom portion of the *funnel* section.

The reason for this may be attributed to using a single outlet tube after the bend section against two tubes in experiments. In order to validate this assumption, the air volume fraction is plotted on a 2D plane in the bottom portion of *funnel* section and a portion of the *extension* region as seen in Figure 3-7 (a). The outlet tube is 2 cm in diameter, and this implies that the Reynolds number in the outlet tube corresponding to a flow rate of 20.9 L/min is around 25000, which is a highly turbulent flow. In order to accommodate for such high mass fluxes, the flow passing through the bend runs into itself, causing the air-core to end abruptly. This creates a pressure differential within the air core, as seen in the static pressure contour of Figure 3-7 (b) (the interface position is shown in white).

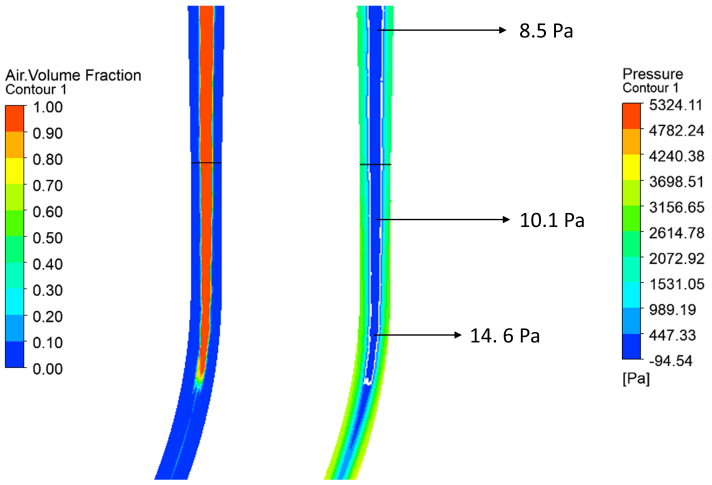

(a) Air-volume fraction (b) Static pressure

Figure 3-7: Contours at the end of air-core on a 2D sectional plane ($r - z$).

Figure 3-8 shows a plot of velocity vectors in water (blue) and air (black) phases at the mid-section (where the helical profile is resolved) and the bottom section (where the interface is flat). Water spirals downwards in both these sections while the vectors in the air core region differ quite significantly.

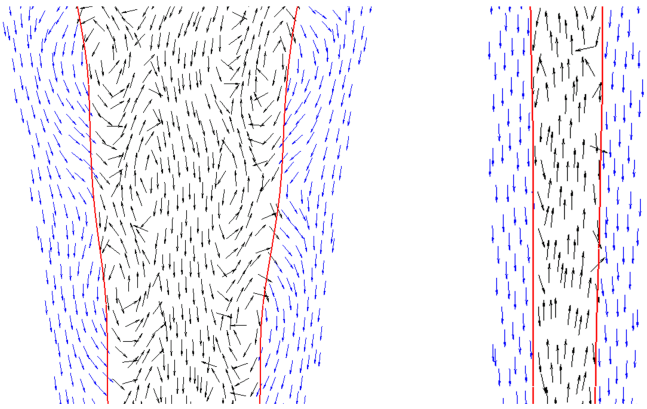

(a) Mid section (b) Bottom section

Figure 3-8: Velocity vectors in water and air phases on a 2D sectional plane ($r - z$).

At the mid-sectional plane, the circulation forces create a favourable pressure differential along the axial direction and hence velocity vectors at the centre of the air-core region travel downwards while the instabilities arising at the interfacial region (to be discussed in Section 3-3-2) lead to the wavy/helical profile of the interface. On the contrary, the pressure differential in the bottom section leads to a net upward motion in the air-core region. The axial velocities at the interfacial region in this section are three times in magnitude as compared to that of mid-section (average axial velocities at the interface are 0.1 m/s downwards and 0.3 m/s upwards in mid and bottom sections, respectively), and this dominates the instabilities smoothening the air core interface in this region rendering it devoid of any helical features. These effects are more dominant in the Straight regime due to higher flow rates (21.5 L/min).

3-3 Flow organisation

3-3-1 Velocity field

The time-average velocity distribution in the water phase is analysed at three non-dimensional heights ($\xi = z/h$) from the exit of *funnel* as shown in Figure 3-9. ξ equals to 1 represents the height of water inlet while ξ equals to 0 represents the end of *funnel*.

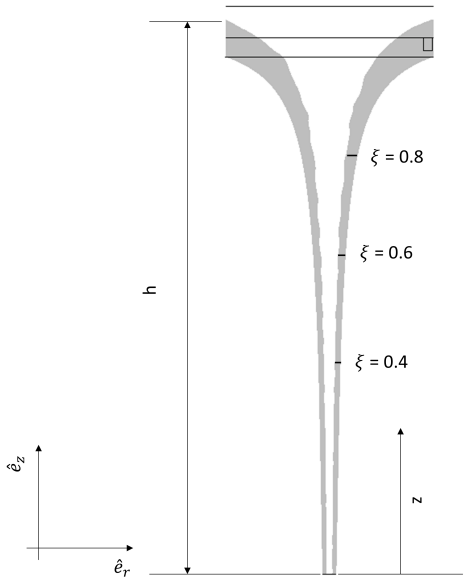

Figure 3-9: Location of non-dimensional heights ξ to analyse the velocity fields.

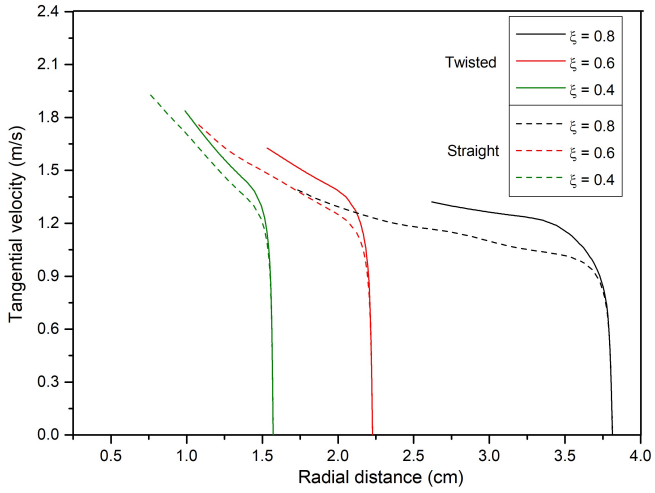

Figure 3-10: Tangential velocity (u_θ) distribution.

The distribution of tangential velocity is shown in Figure 3-10 where the velocity drops to zero in the wall region due to the imposed no-slip condition. With increasing depth from *Water inlet* (i.e. at low ξ), the radius of curvature decreases along the funnel, leading to an increase in the maximum tangential velocity following the conservation of angular momentum. Also,

the absolute values are higher in the Straight than the Twisted regime due to the higher flow rate (or circulation) at the inlet.

The axial velocity distribution for both the regimes is plotted in Figure 3-11. Axial velocities are primarily confined in the near-wall region and to the interface. This is evident in its distribution at $\xi = 0.8$ for the Straight regime, whereas in the far-field region away from the wall, the axial velocity is almost zero and has negligible influence on the flow field organisation. The fluid is driven towards the bottom of the funnel both at the interface and also due to a shear layer developing close to the wall, which is referred to as the Stewartson layer [35]. The fluid in the far-field region is driven by centrifugal force towards the wall after which encountering the Stewartson layer travels downwards.

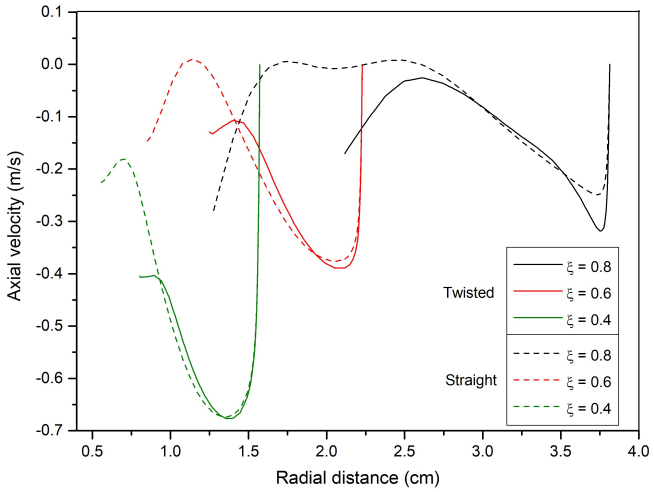

Figure 3-11: Axial velocity (u_z) distribution.

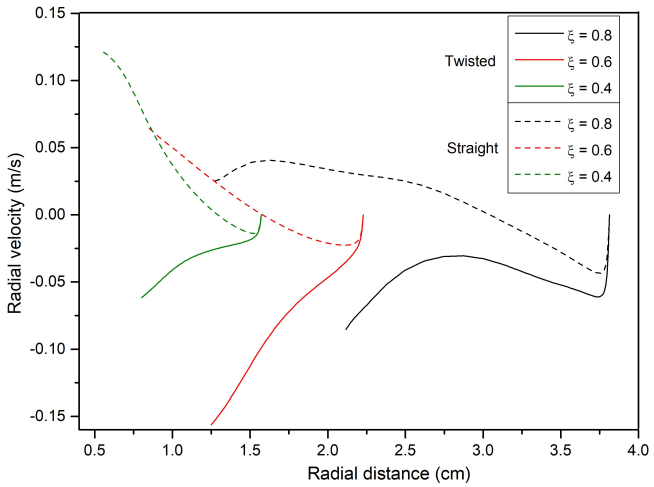

Figure 3-12: Radial velocity (u_r) distribution.

Radial velocities are more predominant near to the interface as seen in their distribution in Figure 3-12, where along with the axial velocities, they provide the necessary energy to sustain an open vortex. Near the funnel's exit, the radial velocities are minimal, and this is

due to the influence of increasing axial velocities in that region, as seen at $\xi = 0.4$. For the Twisted regime, it appears that the fluid tends to flow away from the interface (positive value of radial velocity) while it is the opposite for a Straight regime. This direction depends on the instabilities developed in the secondary flow field, as discussed in the subsequent section.

3-3-2 Instabilities in secondary flow field

As mentioned before, the secondary flow field (radial and axial velocities) needs to be understood on a fundamental level to reason the high gas transfer rates in the system. Plotting the streamlines on a mid-sectional plane for both the regimes as shown in Figures 3-13 and 3-14 shows the presence of *Taylor-like* vortices in water. These streamlines are similar to the ones observed in other studies on the strong vortices by [11], and [18], and hence instabilities do arise in the secondary flow field of both these vortical structures.

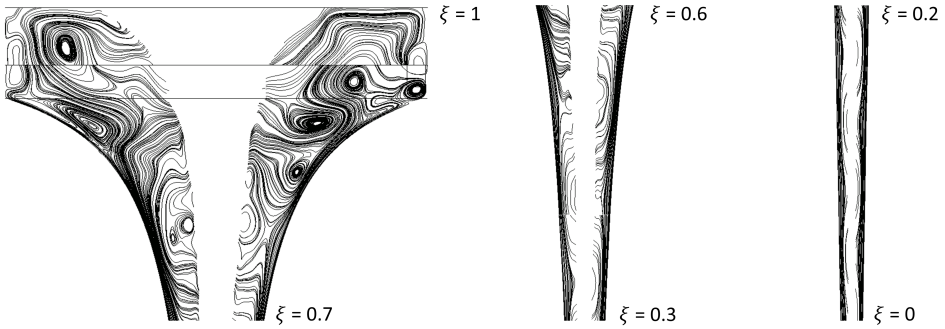

Figure 3-13: Surface streamlines on a 2D sectional plane ($r - z$) for the Twisted regime.

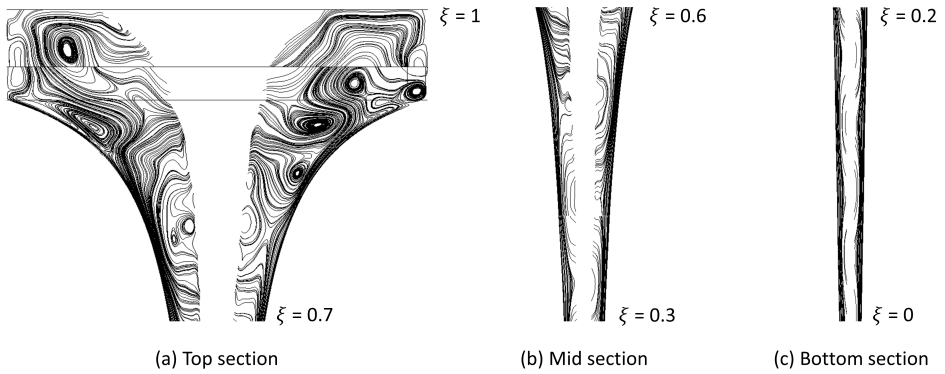

Figure 3-14: Surface streamlines on a 2D sectional plane ($r - z$) for the Straight regime.

The instabilities developed in the flow have a 3D organisation, and the opposite spin direction of Taylor-like vortices in a section can be seen in Figure 3-15 (water in blue). On the interface, downward travelling waves are observed both experimentally and numerically. One such wave is shown in Figure 3-15 where the positions A and B represent its approximate wavelength. Similar waves patterns were also observed in the work of Son et al. [18]. These are attributed to continuous axial translation of Taylor-like vortices due to incoming fluid into the system.

The downward motion of Taylor-like vortices is evident from the velocity vectors at Locations A and B. At the location of such a wave, the interface appears to bulge, and continuous generation of such waves of varying wavelengths produces a 3D wavy profile on the interface.

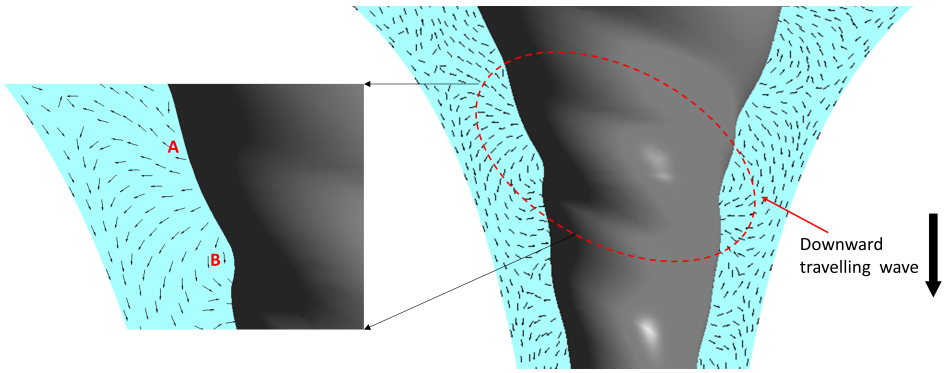

Figure 3-15: Downward travelling wave in the Twisted regime.

3-4 Influence of hydrodynamics on gas transfer

The fundamentals of gas transfer have been discussed in Section 1-2-1 where the overall gas transfer rate was given by

$$RGT_L = [K_L a_L][c_G - c_G^*] \tag{3-1}$$

Equation 3-1 is valid for scenarios where each of these terms is constant across space and time for the whole system, i.e. the liquid side mass transfer coefficient (K_L), the interfacial area (a_L), the equilibrium concentration (c_G) and the bulk concentration (c_G^*). In the case of vortices in the hyperbolic funnel, only c_G can be assumed to be constant (fixed by temperature and pressure) while all the other parameters vary. Therefore, this equation needs to be expressed in a differential form of mass balance, integrated both spatially and temporally to obtain the overall gas transfer rate.

The rate of aeration in a well-mixed elemental control volume dV_L with no biological or chemical reactions with respect to species i is given by [4]

$$\frac{dc_{i,L}^*}{dt} = D_L a_L (c_{i,L} - c_{i,int,L}^*) + K_L \left(c_{i,int,L}^* - c_{i,bulk,L}^*\right) \tag{3-2}$$

Where the term on the left represents the rate of change of concentration of species i in the liquid phase, while on the right-hand side, the first term represents the diffusion of species into the liquid side interfacial area, and the second term represents advection of the diffused species from the interfacial region into the bulk of the fluid. Each of these terms is described in Table 3-3, and a schematic of the aeration process in a 2D sectional plane of the vortex is represented in Figure 3-16 for visualisation.

The variation of interfacial area (a_L) throughout the length of vortex is evident from Figures 1-1, 3-2 and 3-3. Along the length of the vortex, as the species i diffuses and advects,

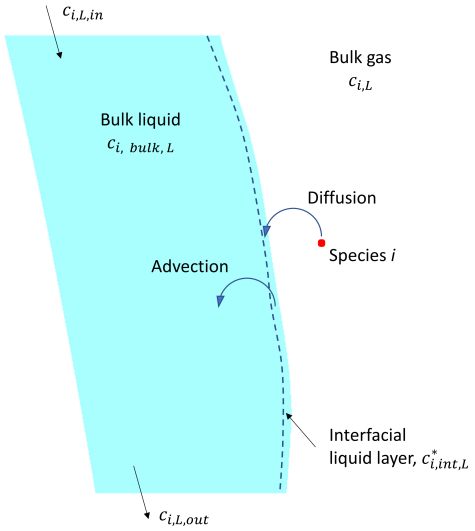

Figure 3-16: Schematic of the aeration process in a 2D sectional plane $(r - z)$ of the vortex.

Table 3-3: Description of terms in Equation 3-16

Term	Description	Variation
D_L	Diffusion coefficient between bulk gas and liquid interface	Constant
a_L	Interfacial area	Variable
$c_{i,L}$	Equilibrium concentration of i	Constant
$c^*_{i,int,L}$	Concentration of species i in the liquid interfacial area	Variable
K_L	Advection coefficient between liquid interfacial area and liquid bulk	Variable
$c^*_{i,L,bulk}$	Concentration of species i in liquid bulk	Variable

its concentration both in the interfacial region ($c^*_{i,int,L}$) as well as the bulk liquid ($c^*_{i,L,bulk}$) changes. The advection coefficient (K_L) is dependent on the mixing in the bulk of liquid [4] which is effected by the turbulence in the form of Taylor-like vortices. The size and distribution of these structures also varies making this term variable.

The rate of gas transfer is dependent on:

1. The average residence of a fluid particle in the system. This is also referred to as the Hydraulic Retention Time (HRT).
2. Interfacial area (a_L).
3. Strength of mixing caused by secondary flow structures.
4. Concentration of species i in the interface and bulk liquid.

It would not be possible to analyse parameter 4 with the current numerical model since mass transfer effects have not been included while parameters 1, 2 and 3 can be qualitatively analysed from the obtained numerical results.

3-4-1 Hydraulic retention time (HRT)

The amount of gas dissolved is directly proportional to HRT, as evident from equation 3-2. As stated before (Section 1-2-2-2), two competing forces are present in this system, namely the circulatory and gravitational forces. The former tends to retain a fluid parcel for a longer time by inducing a circular motion, thus increasing HRT, while the latter decreases HRT by accelerating the fluid out of the *funnel*.

From CFD simulation results, the transient path of streamlines of water from *Water Inlet* to *Outlet* was tracked. Each streamline differs from the other in terms of time (t_i) spent by it in the *funnel* section. This is dependent on the path followed. A streamline travelling close to the walls of the funnel experiences less circulatory forces than gravitational forces leading to very low HRTs. The opposite is true for a streamline travelling close to the air-water interface, which is a region of high tangential velocities and has higher HRTs. Both these scenarios are represented in Figure 3-17 where the spheres on the streamline represent the position of an elemental fluid parcel at an interval of 0.5s.

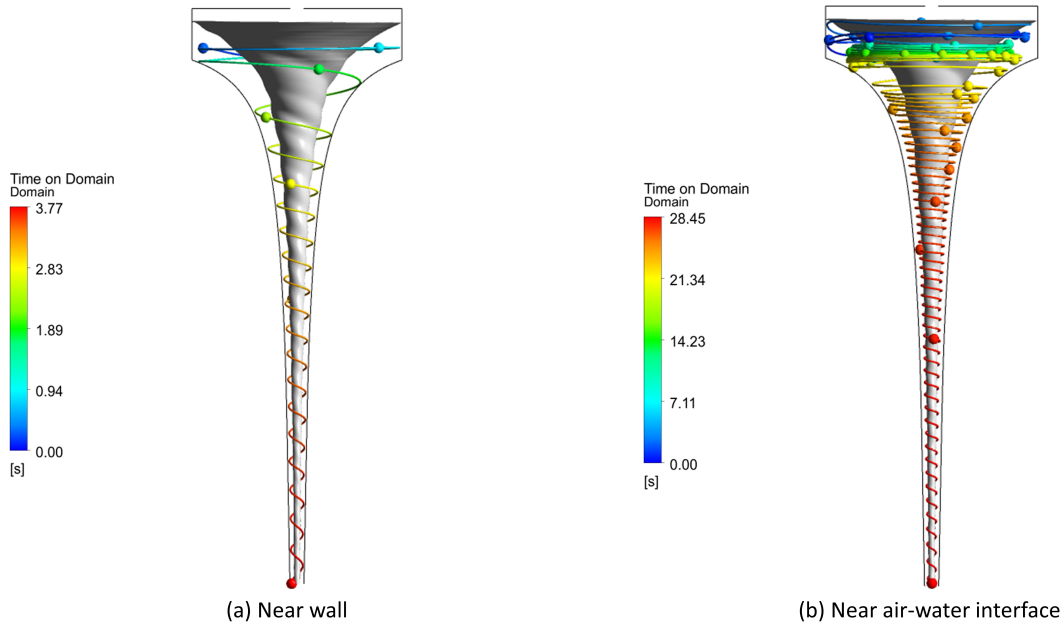

(a) Near wall (b) Near air-water interface

Figure 3-17: Streamline paths in *Twisted* regime with 3D air-core iso-surface in gray and *funnel* wall boundaries in black.

Figure 3-18 shows a plot of non-dimensional time ($\theta = t/t_i$) versus the non-dimensional height (ξ) for streamlines starting from *Water inlet* and exiting at end of *funnel*, i.e. Location I in Figure 2-10. This non-dimensional plot is in the form of an exponential decay function, and using multiple regression analysis, the average path versus time of these streamlines is shown in red. It is observed that a fluid parcel, on average, resides for 90% of its HRT within about half-height of the funnel (i.e. $\xi \geq 0.5$ for $\theta \leq 0.9$) and travels the remaining half in just around 10% of its HRT. Using the same methodology for the Straight regime, it is found that fluid parcel covers just 30% of the depth (i.e. $\xi \geq 0.7$ for $\theta \leq 0.9$) in 90% of its HRT due to higher circulatory forces.

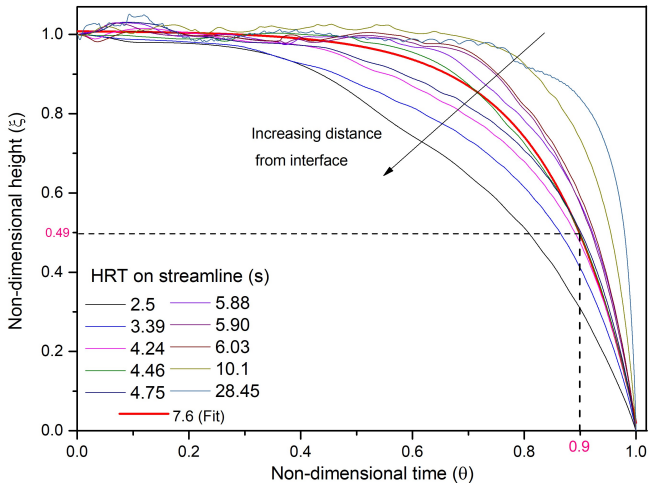

Figure 3-18: Non-dimensional time vs height for streamlines in *funnel* section for the Twisted regime.

Hence, the system can be divided into two sections with respect to HRT, Section I in which fluid resides for most of its duration ($\theta \leq 0.9$) in the *funnel* and Section II ($0.9 < \theta \leq 1$) which is predominantly the region with the least radius where the fluid rapidly accelerates and exits the *funnel*. The average HRTs in Twisted and Straight regimes from experiments are 18s and 29s respectively [1]. Purely based on HRTs, the Straight regime should exhibit more aeration capabilities in comparison to the Twisted regime, but the experimental data indicate the opposite trend [1]. Hence, the other two parameters, i.e. interfacial area and mixing in the bulk of fluid, must be analysed to reason this behaviour. These parameters are analysed in each of these sections of the *funnel* where Section I, the upper 40% height (i.e. $\xi \geq 0.6$ average of Twisted and Straight regimes) while Section II is the remaining portion ($0 \leq \xi < 0.6$).

3-4-2 Interfacial area

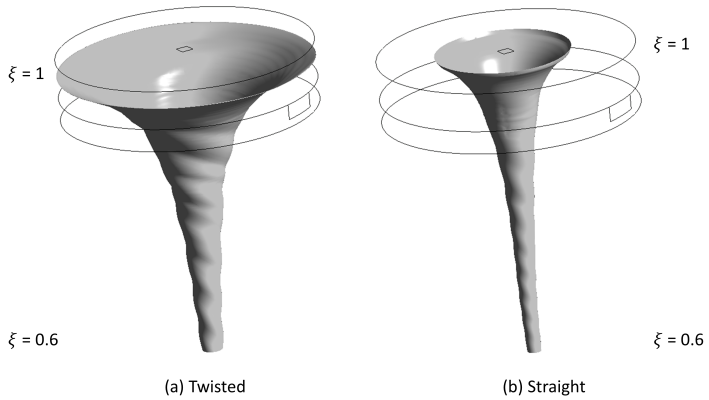

Figure 3-19: Air-water interface in Section I.

The air-water region directly affects the area available for the diffusion of gas molecules. Also,

considering both phases are incompressible at the operating conditions in a fixed volume of *funnel*, more interfacial area implies that less mass of water (m_w) is present in the system. The 3D iso-surface of the interface in Section I for both the regimes is shown in Figure 3-19.

In Section I, the Twisted regime has more than twice the interfacial area in comparison to the Straight regime as tabulated in Table 3-4. Also, in this section where the fluid has higher HRT, the Twisted regime has 44% less mass of water (SOTR varies inversely with the mass of water). In Section II, both the regimes have a comparable mass of water (13% less in the Twisted regime). The added advantages of the higher interfacial area and lower mass of water facilitate higher SOTRs for the Twisted regime.

Table 3-4: Comparison of regimes in terms of parameters governed by air-water interface

Parameter	Regimes	Section I	Section II	Total
A_{int} (m^2)	**Twisted**	0.1213	0.0203	0.1416
	Straight	0.0568	0.0139	0.0708
	Ratio	**2.1**	**1.5**	**2.0**
V_{air} (%)	**Twisted**	50.2	23.6	49.2
	Straight	10.1	11.0	10.2
	Ratio	**5.0**	**2.2**	**4.8**
m_w (kg)	**Twisted**	4.2	0.26	4.4
	Straight	7.5	0.30	7.8
	Ratio	**0.55**	**0.87**	**0.56**

3-4-3 Mixing

Mixing can be qualitatively characterised by vorticity, which represents the local spinning of a fluid parcel. As a preliminary analysis, vorticity is analysed in a 2D sectional plane (r-z plane, and the computed vorticity is normal to this plane, i.e. Ω_θ in equation 1-5). Wide scales of vorticity are observed in the domain. For instance, in the Twisted regime at the end of Section I ($\xi = 0.6$), Ω_θ varies from around 3300 s^{-1} at the wall to around 20 s^{-1} at the interface. The high values near the walls are due to no-slip boundary condition, but this does not contribute to mixing in bulk. The plots of vorticity along with velocity vectors projected onto this plane in both the regimes are shown in Figures 3-20 and 3-21. In these figures, the scales of vorticity are chosen such that they are distinctly visible.

The vorticity has a higher value near the interface due to the difference in velocity of phases at this location. With increasing depth, the magnitude of vorticity also increases, and this can again be attributed to the increase in axial velocities in the regions. The magnitude of volume average vorticity ($|\boldsymbol{\Omega}|$) is higher by 40.6% in in Twisted regime (74.54 s^{-1}) in comparison to the Straight regime (53.03 s^{-1}). Hence, the Twisted regime benefits from higher interfacial areas, less mass of fluid and higher vorticities than the Straight regime leading to higher gas transfer rates.

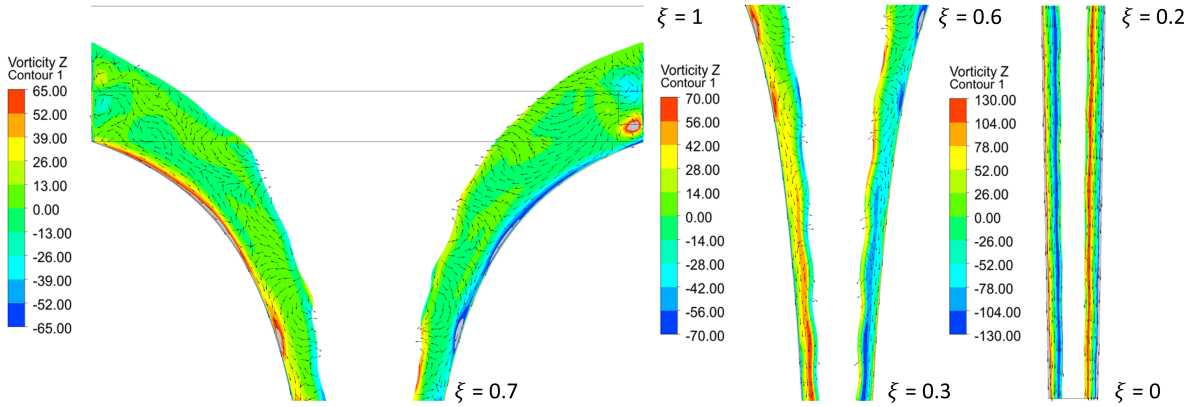

(a) Top section (b) Mid section (c) Bottom section

Figure 3-20: Vorticity (Ω_θ) in 2D sectional plane ($r - z$) for the Twisted regime.

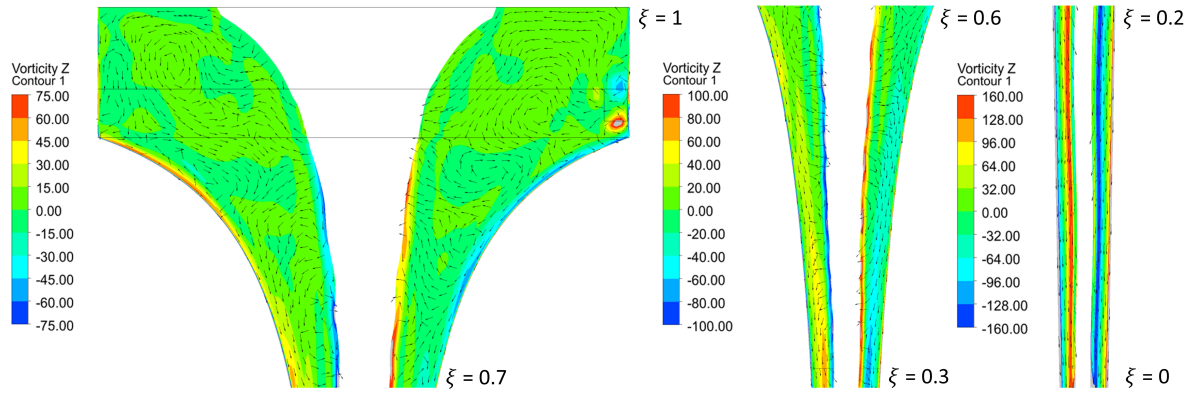

(a) Top section (b) Mid section (c) Bottom section

Figure 3-21: Vorticity (Ω_θ) in 2D sectional plane ($r - z$) for the Straight regime.

3-4-4 Comments on enhancement methods

One of the challenges of the present system is that in spite of such high gas transfer rates, the water exiting the *funnel* is undersaturated with respect to oxygen concentration, i.e. $c_{i,L,out} < c_G$. This implies that more amount of oxygen can be dissolved in it.

The rate of dissolution of a gas component i into a fluid (or solvent) is directly proportional to the partial pressure of that component in the gas stream that is in contact with the fluid. The partial pressure is turn proportion to the percentage concentration of i. Hence increasing the concentration or purity of the component will lead to higher gas transfer rates [4]. Presently atmospheric air, which has an oxygen concentration of around 21%, is entering the system. Instead, the *Air vent* can be connected to a tank filled with oxygen of high purity. Gas transfer rates are also enhanced by increasing the pressure at which the gas stream is supplied, but this is not a controllable parameter in the present system since it is set by the sub-pressures created by the circulatory forces of incoming fluid.

The amount of gas dissolved is also directly proportional to the HRT, and for a given flow

rate, the dimensions of the *funnel* influence HRT. The *funnel* section could be increased in dimensions either by increasing the radius of the upper portion or further elongating the funnel at the exit. These are marked on one half of a 2D sectional plane by A and B in Figure 3-22 respectively. The total volume of the funnel would increase, and this would lead to a decrease in the vortex height h in the top cylindrical portion. However, its influence on the overall structure of the vortex formed is expected to be negligible since the hyperbolically shaped funnel part is unaltered. This would also lead to an increase in interfacial area for gas transfer.

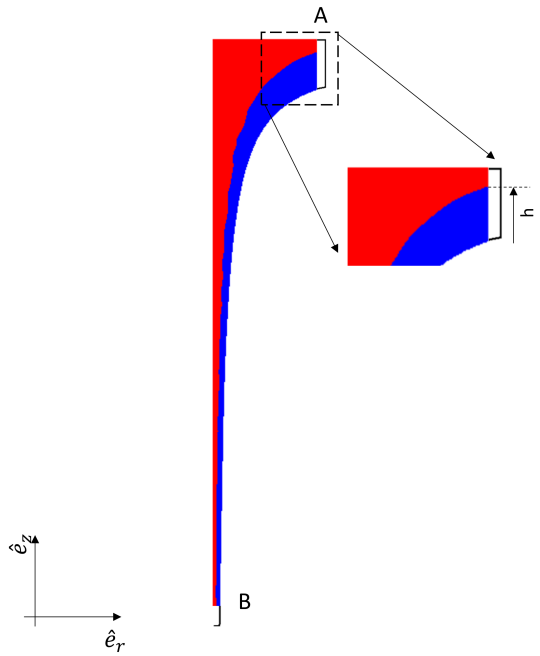

Figure 3-22: Schematic of increasing the volume of *funnel* section by increasing the radius on the top of cylindrical portion (A) or extending on the bottom (b) represented on a air-water volume fraction contour.

The air-water interfacial area is set by the system's circulatory forces, which depends on the inlet mass flow rate. For a given funnel adjusting the mass flow rate would change the vortex regime, which may lead to loss of inherent advantages of the Twisted regime. Another alternative would be to increase the dimensions of the system in such a way that the increased mass flow rate produces a Twisted regime, but this comes at the cost of increased mass in the system, which affects the SOTR.

One way to increase the circulatory forces by maintaining the inlet mass flow rate constant is to decrease the diameter of the inlet tube, which enters the top cylindrical portion tangentially (Figure 2-1). This increases the kinetic energy of fluid entering the system due to increased velocities leading to:

- Higher sub-pressures in the vortex, which in turn increases the pressure differential for atmospheric air to enter the system.
- Increased inlet velocities imply increased overall tangential velocity in the system, which increases HRTs.

- Increased energy content in the fluid also increases the strength of Taylor-like vortices, leading to increased vorticity in the fluid.

Each of these parameters enhances the gas dissolution rates, thereby increasing the concentration of species at the exit of the *funnel* ($c_{i,L,out}$) section.

Chapter 4

Conclusions

4-1 Summary

The present study aimed to simulate vortices in hyperbolic funnels using CFD and thereby analyse their flow field organisation to understand the underlying physical mechanisms responsible for high gas transfer rates.

In Chapter 1, experimental observations concerning strong free-surface vortex regimes and their gas transfer rates were briefly discussed. A thorough literature survey on the gas transfer phenomenon was done to understand and analyse the process's factors. The fundamentals of vortices in terms of their formation, classification and velocity distribution were also reviewed. An important finding in the works of previous researchers was regarding the instabilities that developed in the secondary field of turbulent vortices. These instabilities were similar to the Taylor-vortices that form in a Taylor-Couette system. A turbulent vortex could be visualised as a Taylor-Couette system with a fixed outer cylinder and the rapidly spinning air-core that acts as a virtual inner cylinder. It was then hypothesised that similar instabilities might also be arising in the hyperbolic funnel vortices, which would enhance mixing in the bulk of fluid, leading to higher gas transfer rates. In order to validate this, a numerical approach was chosen for this study to simulate vortices using CFD.

The sequential steps involved in numerical modelling, namely: setting up of the computational domain, meshing, multi-phase modelling and turbulence modelling, are discussed in Chapter 2. Two different computational domains were investigated in the present study, one where the *funnel* section alone is modelled and the other in which the *extension* is also included. The former did not produce a stable vortex since flow conditions at the exit of the system were unknown due to the highly swirling nature of the flow. The suitability of various boundary conditions based on experimental conditions and vortex formation mechanism was comprehensively discussed by analysing the results obtained. The *Outlet* boundary condition needs to be switched from Pressure Outlet in the initial stages of vortex formation to Outflow boundary condition as the flow fully develops at the exit. The procedure and the validity of this methodology have also been discussed in this chapter.

CFD simulations were performed using ANSYS-Fluent 19R3 and the results obtained are the subject matter of discussion in Chapter 3. The mesh independence study was performed for four different mesh densities, and it was observed that as the mesh density increased, the resolution of the helical profile of the interface increased. Based on the available time for the present study, *2mil* mesh was chosen as optimal grid size. The SST based k-ω turbulence model captured the interface location well for both the Twisted and the Straight regimes. In the secondary flow-field, instabilities in the form of counter-rotating *Taylor-like* vortices were observed in both the regimes of the vortices.

These two regimes were compared based on three parameters that influence the amount of gas dissolved into the system. These are (i) HRT, (ii) air-water interface area and (iii) mixing in bulk. The mixing was qualitatively gauged in terms of the average vorticity per unit mass of water. It was observed the retention time of a fluid parcel was dependent on its radial distance from the interface. The closer it is to the interface, the higher the circulatory forces leading to higher retention times and on the other hand, if it is closer to the funnel wall, they have lower retention times due to higher axial forces (gravity) in comparison to the circulatory forces. Any fluid parcel, on average, spends around 90% of its HRT within about 40% of sub-surface depth from *Water Inlet* for both the regimes.

Although the Twisted regime had lower HRT than the Straight regime, the former had much higher interfacial area and average vorticity per unit mass of water compared to the latter (100% and 40.6% higher respectively). These can be attributed to the Twisted regime's lower fluid mass than the Straight regime (50% less). Hence, it was concluded that due to these inherent advantages in the Twisted regime, its gas transfer rates were superior to the Straight regime.

4-2 Limitations of the CFD model

The present study elucidates the methodology to form vortices in hyperbolic funnels using appropriate boundary conditions. However, the simulations in their present form suffer from few drawbacks such as

- **Exit back-pressure:** The use of a single outlet tube at the exit of *funnel* section leads to high reversed flow in the air core region. This affects the structure of the air-water interface that is formed at this location.
- **Mass transfer effects:** The obtained numerical results cannot be directly extended to include mass transfer effects since the Volume-of-Fluid approach does not incorporate species transfer effects. In order to do so, simulations would have to be performed using the Mixture model.
- **Surface roughness:** In wall-bounded turbulent flows as in the present system, the surface roughness of the walls plays a significant role in flow field organisation of the near-wall region. In the simulations performed, the influence of this parameter is not analysed, and wall roughness height is set to zero.
- **Inlet flow conditions:** The inlet tube is modelled as a region on the cylindrical surface in the CFD simulations. Inlet conditions are set at 5% turbulent intensity.

In the experimental setup, the inlet tube bends twice before it tangentially enters the cylindrical portion of the funnel as seen in Figure 4-1. It is possible that this bend already induces a swirl in the flow field at the inlet. This is not taken into account in the present study.

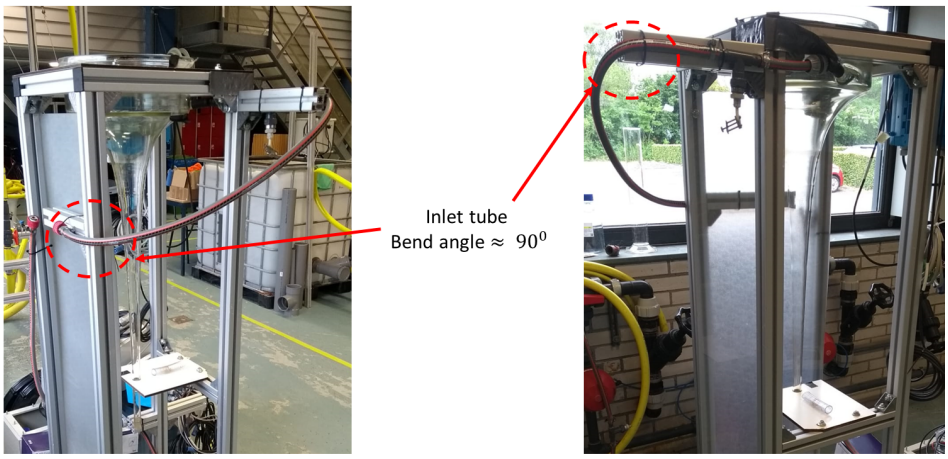

(a) Side view (b) Front view

Figure 4-1: Bending of the inlet tube before it tangentially intersects the cylindrical portion of the *funnel*.

4-3 Recommendations

Simulating a vortex structure in the hyperbolic funnel by choosing appropriate boundary conditions and their locations took longer than anticipated at the start of this study. Due to this, two of the five objectives that were initially agreed upon (Section 1-4) were unfortunately not realised. These are about characterising the vortex regimes using suitable non-dimensional numbers and simulating mass transfer effects using CFD. This must be considered in future studies since the former would help up-scaling the funnel for commercial usage while the latter aids in quantitatively analysing the concentration of species both spatially and temporally. Also, studying mass transport phenomena across a turbulent interface is of importance from a fundamental perspective.

The obtained CFD results were validated with respect to the location of the air-water interface from experimental data. Further validation is necessary by comparing the velocity field with PIV data to assess the mesh and the capabilities of the turbulence model chosen to capture the unsteady dynamics of vortex structures. Although SST based k-ω turbulence model with curvature correction predicts the air-water interface location well, studies have indicated that LES models perform better in predicting the flow field distribution (velocity, vorticity, turbulent kinetic energy etc.) for vortex flows [56, 59, 60]. Performing LES simulations might also help in capturing the instabilities in the flow field better.

Simulations on hyperbolic funnels of different geometric dimensions need to be performed with flow rates adjusted such that Twisted and Straight regimes are formed in them. Firstly, this would provide deeper insights in deducing non-dimensional numbers for the vortical

structures based on funnel geometry and imposed flow conditions. Secondly, these funnels could be assessed based on factors contributing to the gas transfer process (HRT, interfacial area and mixing), leading to the design of an optimised system with higher gas transfer rates and saturation levels concerning the concentration of dissolved species at the exit.

Appendix A

Experimental setup and findings

The schematic of the experimental setup is shown in Figure A-1. The aeration system is a single structure with the cylindrical portion on the top and a hyperbolically shaped funnel section on the bottom. It has a small opening on the top cylindrical portion to facilitate the flow of air into the system due to sub-pressures created by the formation of a vortex (equation 1-12).

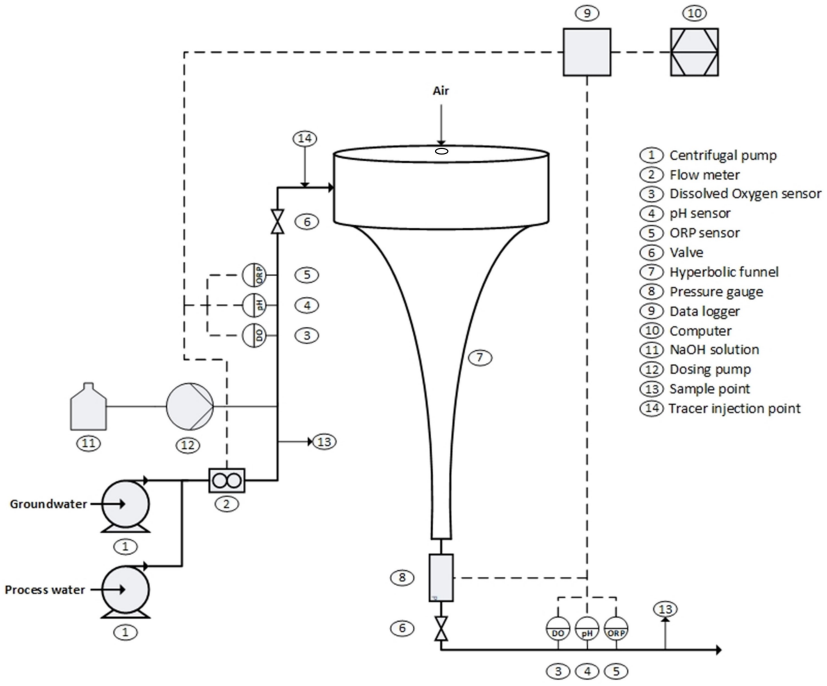

Figure A-1: Schematic of the experimental setup.

Groundwater is pumped by a centrifugal pump, and its flow rate is controlled by a ball valve.

A flow metre measures the inlet flow rate of water supplied to the system. This water enters the cylindrical part of the aeration system tangentially and exits via a tube connected at the bottom of the funnel. At the inlet and outlet tubes, sensors for measuring pH, dissolved oxygen levels and oxygen reduction potential are present, which are connected to a data logger to store their transient values. A pressure sensor was located at the exit of the funnel to measure the static pressure values.

Three different flow regimes (Restricted, Twisted and Straight) are obtained by varying the inlet flow rate of water and applying an outlet pressure restriction. The ball valve controls the former while the latter is achieved by constricting the cross-sectional area of the exit tube at the bottom of the funnel. The flow rate values are summarized in Table A-1.

Table A-1: Characterization of flow regimes [1]

Regime	**Flow Rate (L/min)**		**Volume of water (%)**		**SAE (kg O_2/kWh)**	
	Min	**Max**	**Min**	**Max**	**Min**	**Max**
Restricted	14.7	15.7	44	82	1.9	5.4
Twisted	19.9	20.9	39	65	10	23.1
Straight	22	23	91	95	5.5	5.5

Outlet pressure restriction was applied only for the Restricted regime. As flow rate increases in each individual regime the volume of air core formed decreases and so does the air-water interface area as experimentally seen in Figures A-2 to A-4.

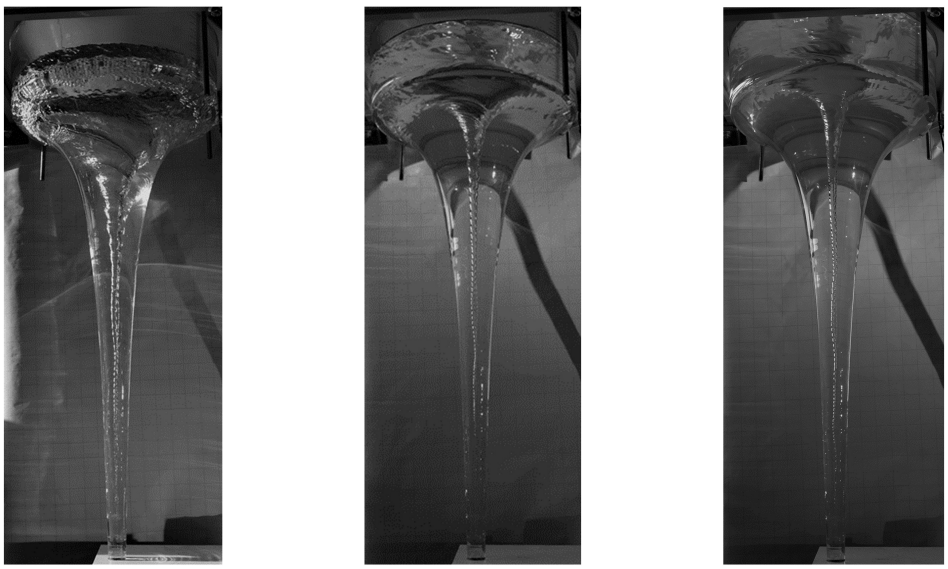

(a) 14.7 L/min (b) 15.2 L/min (c) 15.7 L/min

Figure A-2: Experimental images of the Restricted regime [1].

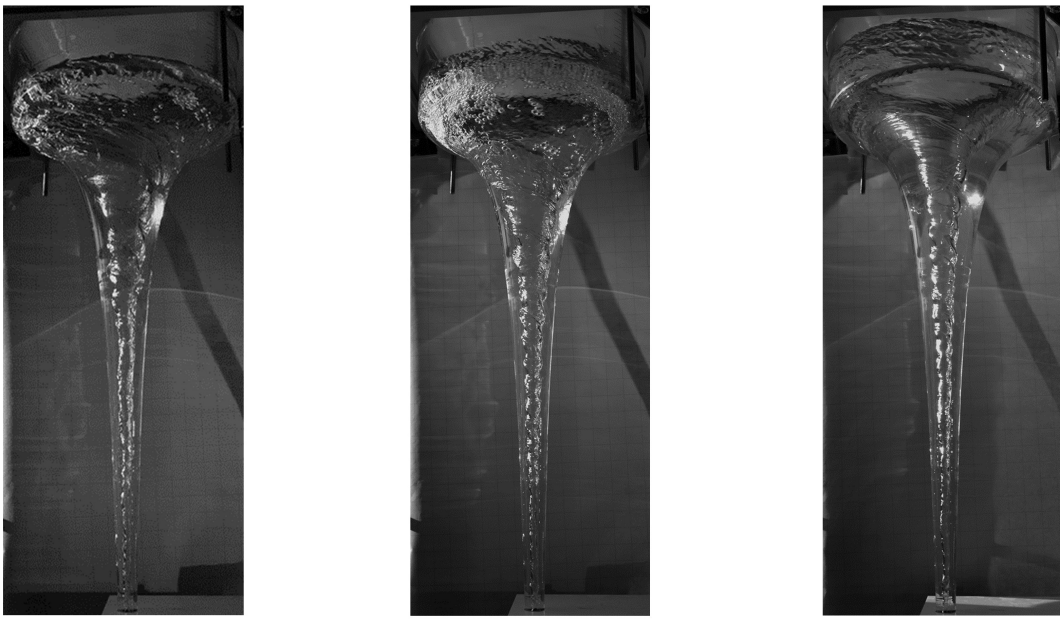

(a) 19.9 L/min (b) 20.4 L/min (c) 20.9 L/min

Figure A-3: Experimental images of the Twisted regime [1].

(a) 22.0 L/min (b) 22.5 L/min (c) 23.0 L/min

Figure A-4: Experimental images of the Straight regime [1].

Appendix B

Eddy viscosity models

This appendix is intended to give a brief theoretical overview of SST based $k-\omega$ model. Hence, rigorous mathematical proofs of the equations are avoided and can be found in [41] and [50].

In turbulent flows, a fluid element experiences shearing due to viscous forces and the turbulent eddies present in the flow. The former is referred to as *Viscous shear* which for a simple 2D flow field is given by

$$\tau = \mu \frac{\partial U}{\partial y} \tag{B-1}$$

while the latter is referred to as the *Reynolds stress tensor* given by

$$\tau = -\rho\overline{u'v'} \tag{B-2}$$

Eddy viscosity models are used to determine the *Reynolds stress tensor* by correlating it to the mean velocity ($\boldsymbol{U}$) field. This is done by assuming that the turbulent motions are random and similar to the Brownian motion of gas molecules. These random motions are then effected by the mean velocity profile $\boldsymbol{U}(\boldsymbol{x}, t)$. Since $\boldsymbol{U}$ varies across space and time, each fluid element differs from its neighbouring element in terms of its associated momentum. Hence, there is a net transport of momentum via the *diffusion* process (i.e. molecular collisions) in the direction of the positive velocity gradient. Boussinesq approximated that the *Reynolds stress tensor* is proportional to the velocity gradient of the mean flow [50]

$$-\rho\overline{u'v'} = \mu_t \frac{\partial U}{\partial y} \tag{B-3}$$

This is referred to as the *Boussinesq hypothesis*. In a 3D case, the shear stress can written as

$$-\rho\overline{u'v'} = \mu_t \left(\frac{\partial U}{\partial y} + \frac{\partial V}{\partial x} \right) \tag{B-4}$$

while the normal stress component (accounting for the turbulent kinetic energy correction) is

$$-\rho\overline{u_i'u_j'} = \mu_t \left(\frac{\partial U_i}{\partial x_j} + \frac{\partial U_j}{\partial x_i} - \frac{2}{3}\frac{\partial U_k}{\partial x_k} \right) - \frac{2}{3}\rho k \tag{B-5}$$

Equations B-4 and B-5 can be combined into a single equation using the Kronecker delta function (i.e. $\delta_{ij} = 1$ if $i = j$ else null value)

$$-\rho\overline{u_i' u_j'} = \mu_t \left(\frac{\partial U_i}{\partial x_j} + \frac{\partial U_j}{\partial x_i} - \frac{1}{3}\frac{\partial U_k}{\partial x_k}\delta_{ij} \right) - \frac{2}{3}\rho k \delta_{ij} \tag{B-6}$$

Substituting the strain-rate tensor (S_{ij}) from equation 2-6 into equation B-6 it results in

$$-\rho\overline{u_i' u_j'} = 2\mu_t \left(S_{ij} - \frac{1}{3}\frac{\partial U_k}{\partial x_k}\delta_{ij} \right) - \frac{2}{3}\rho k \delta_{ij} \tag{B-7}$$

The turbulent viscosity (μ_t) is dependent on the turbulence model chosen.

B-1 $k-\epsilon$ and $k-\omega$ turbulence models

In this model the turbulent viscosity (μ_t) is determined based on the mixing length (l_m).

$$\mu_t = \rho l_m^2 \left| \frac{\partial U}{\partial y} \right| \tag{B-8}$$

Mixing length is analogous to the mean free path used in the kinetic theory of gases and is the average distance that a fluid particle travels before its exchanges momentum with other fluid particles and is a representative of the size of eddies at a given location. Initially, l_m was defined purely based on linear distance from the wall [50]. However, in reality, the size of an eddy is affected due to its diffusion and convection in the flow field, and hence a transport equation needs to be solved. So the *turbulent dissipation rate* (ϵ) is solved for, which is another metric for determining the size of an eddy. Larger is the size of the eddy, smaller is its dissipation and hence dissipation rate. In the viscous sublayer close to the wall, small scale eddies (ϵ is high) are dissipated by viscous forces to thermal energy. The relation between turbulent viscosity (μ_t) and turbulent dissipation rate (ϵ) is given by

$$\mu_t = C_\mu \frac{\rho k^2}{\epsilon} \tag{B-9}$$

The transport equation for turbulent kinetic energy (equation B-10) and turbulent dissipation rate (equation B-11) can be written as

$$\frac{\partial(\rho k)}{\partial t} + \nabla \cdot (\rho \boldsymbol{U} k) = \nabla \cdot \left[(\mu + \mu_t/\sigma_k) \nabla k \right] + \boldsymbol{P_k} + \boldsymbol{P_b} - \boldsymbol{\rho\epsilon} + \boldsymbol{S_k} \tag{B-10}$$

$$\frac{\partial(\rho \epsilon)}{\partial t} + \nabla \cdot (\rho \boldsymbol{U} \epsilon) = \nabla \cdot \left[\left(\mu + \frac{\mu_t}{\sigma_\epsilon} \right) \nabla \epsilon + \boldsymbol{C_1} \frac{\boldsymbol{\epsilon}}{\boldsymbol{k}} \left(\boldsymbol{P_k} + \boldsymbol{C_3 P_b} \right) - \boldsymbol{C_2 \rho} \frac{\boldsymbol{\epsilon^2}}{\boldsymbol{k}} + \boldsymbol{S_\epsilon} \right] \tag{B-11}$$

The symbols in bold represent the sources and sink for k and ϵ while the coefficient in equation B-11 (C_1, C_2 and C_3) depend on the variation of $k-\epsilon$ turbulence model that is chosen [61].

In the viscous sublayer, the mixing length is small (smaller eddies) and in order to include this effect into equation B-11 damping functions $f_i's$ are used on the model constants $C_i's$ (i=

1, 2 and μ). These functions act to increase the dissipation of k (due to viscous action) in the viscous sub-layer and this is achieved by defining f_μ as [62]

$$f_\mu = \exp\left(\frac{-3.4}{(1+(\mathrm{Re}_T/50))^2}\right) \tag{B-12}$$

Re_T represents the turbulent reynolds number which increases with increasing distance from the wall. Far away from the wall f_μ is unity and close to it its value is less than unity mimicking the high dissipation of k near the walls by viscous forces. These are referred to as the *high* and *low-Re formulations* respectively.

Thus, in principle, the $k-\epsilon$ turbulence model with damping functions can be used to resolve the turbulence length scales all the way to the viscous sub-layer. Studies have shown that in the presence of adverse pressure gradient near the walls, this model is not very accurate ([63], [64]). This might be because of the damping functions which have been empirically derived considering flow over flat plates. In contrast, aerofoils and blades used in turbo-machinery have a curving wall profile.

Instead of using turbulent dissipation rate (ϵ) as one of the transport equations (equation B-11), the specific turbulent dissipate rate (ω) can be used [65].

$$\omega = \frac{\epsilon}{C_\mu k} \tag{B-13}$$

This leads to modification of equation B-11 by

$$\frac{\partial(\rho\omega)}{\partial t} + \nabla\cdot(\rho\boldsymbol{U}\omega) = \nabla\cdot\left(\left(\mu+\frac{\mu_t}{\sigma_k}\right)\nabla\omega\right) + \frac{\gamma}{\nu_t}P_k - \beta\rho\omega^2 \tag{B-14}$$

This eliminates the need for damping functions for the $k-\omega$ model making it more suitable for resolving the viscous sublayer. However, this also suffers from being sensitive to free-stream turbulence conditions and the reason for this might be that the model coefficients used in equation B-14 ($\alpha, \beta, \beta^\star, \sigma_k, \sigma_\omega, \sigma_{\omega 2}$) are not entirely accurate [66] .

B-2 $k-\omega$ SST turbulence models

The inaccurate damping terms in the $k-\epsilon$ equation make it unsuitable for use in regions of adverse pressure gradient and $k-\omega$ model is sensitive to the free stream turbulent dependence conditions. This lead to the blending of the two models by Menter [67] by substituting equation B-13 into the transport equation for turbulent dissipation (equation B-11) leading to

$$\frac{\partial(\rho\omega)}{\partial t} + \nabla\cdot(\rho U\omega) = \nabla\cdot\left(\left(\mu+\frac{\mu_t}{\sigma_k}\right)\nabla\omega\right) + \frac{\gamma}{\nu_t}P_k - \beta\rho\omega^2 + \mathbf{2\frac{\rho\sigma_{\omega 2}}{\omega}\nabla k : \nabla\omega} \tag{B-15}$$

The bold term in the end of equation B-15 is an additional term obtained from the $k-\epsilon$ model. A using a suitable blending function F_1 (based on distance from nearest wall) is incorporated such near to the wall ($F_1 = 0$) the $k-\epsilon$ model is used while far way from it ($F_1 = 1$) the $k-\omega$ is solved.

$$\frac{\partial(\rho k)}{\partial t} + \nabla\cdot(\rho U k) = \nabla\cdot\left(\left(\mu+\frac{\mu_t}{\sigma_k}\right)\nabla k\right) + P_k - \rho\epsilon \tag{B-16}$$

$$\frac{\partial(\rho\omega)}{\partial t} + \nabla \cdot (\rho U \omega) = \nabla \cdot \left(\left(\mu + \frac{\mu_t}{\sigma_k} \right) \nabla \omega \right) + \frac{\gamma}{\nu_t} P_k - \beta \rho \omega^2 + 2 (1 - F_1) \frac{\rho \sigma_{\omega 2}}{\omega} \nabla k : \nabla \omega \tag{B-17}$$

These transport equations are referred to as the baseline (BST) $k-\omega$ turbulence models. However, these tend to over predict the wall shear stress [41]. Including the effects of transport of wall shear stresses in turbulent viscosity (μ_t) leads to a viscosity limiter resulting in modification of its definition to

$$\mu_t = \frac{a_1 \rho k}{\max(a_1 \omega, S F_2)} \tag{B-18}$$

Where F_2 is a blending function similar to F_1 and S represents shear stresses. If F_2 (or S) is large, it implies a region close to the wall and μ_t is limited in such cases. This modification leads to the Shear Stress Transport (SST) based $k-\omega$ turbulence models. The model coefficients used by ANSYS Fluent can be found in [41]. A turbulence damping term is also used to accurately model the velocity gradients at the interface in the multi-phase simulation since these are regions of high turbulent intensity.

Appendix C

Euler equation in streamwise coordinates

The Navier-stokes equations 1-9 and 1-12 can be written in cartesian coordinates as

$$\nabla \cdot \boldsymbol{u} = 0 \tag{C-1}$$

$$\rho \left[\frac{\partial \boldsymbol{u}}{\partial t} + \boldsymbol{u}.\nabla \boldsymbol{u} \right] = -\nabla p + \mu \nabla^2 \boldsymbol{u} + \boldsymbol{f} \tag{C-2}$$

Here $\boldsymbol{f}$ represents the body force term. A flow field can be characterized as either a inertial or viscous dominate flow based on its Reynolds number (Re). In case of former the viscous term in equation C-2 is negligible and can be re-written as

$$\rho \left[\frac{\partial \boldsymbol{u}}{\partial t} + \boldsymbol{u}.\nabla \boldsymbol{u} \right] = -\nabla p + \boldsymbol{f} \tag{C-3}$$

Equations C-1 and C-3 together form the *Euler equations* which are the flow governing equations in an inertial dominated flow.

$$\rho \boldsymbol{u}.\nabla \boldsymbol{u} = -\nabla p \tag{C-4}$$

The streamlines in a two-dimensional flow field at steady-state are shown in Figure C-1 (a). The streamline coordinates are defined with unit vectors ($\hat{n}$, $\hat{t}$) such that $\hat{n}$ is normal to the streamlines while $\hat{t}$ is aligned along the streamlines (s). For a steady state flow ignoring the body force term equation C-3 can be re-written as

The velocity field and pressure gradient can be represented as

$$\boldsymbol{u} = \boldsymbol{u}(s,n) \cdot \hat{t} = \begin{bmatrix} u(s) \\ 0 \end{bmatrix}, \quad \nabla p = \begin{bmatrix} \frac{\partial P}{\partial s} \\ \frac{\partial P}{\partial n} \end{bmatrix} \tag{C-5}$$

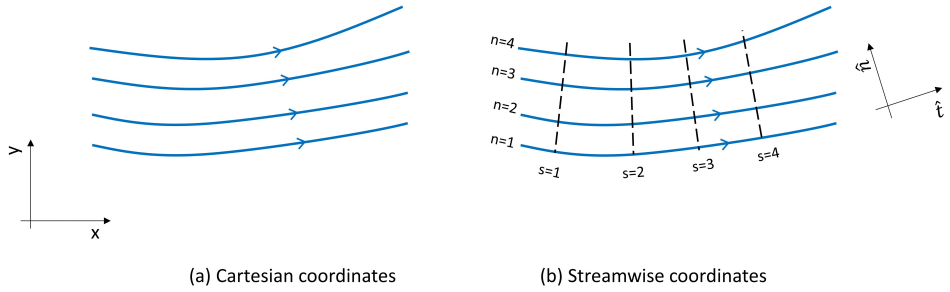

(a) Cartesian coordinates (b) Streamwise coordinates

Figure C-1: Streamlines in a steady-state 2D flow field.

Substituting equation C-5 into equation C-4 yields the Eulers equation in streamwise coordinates which after suitable substitutions [68] can be written as

$$\rho u(s)\frac{d}{ds}(u\hat{t}) = \rho u(s)\left[\frac{\partial}{\partial s}(u(s))\right]\hat{t} + \rho\frac{u^2(s)}{R(s)}\hat{n} \tag{C-6}$$

The first term on the RHS represents the component along the streamwise direction, and this term upon integration along a streamline yields the weak form of Bernoulli's equation. In the second term, which is directed along the normal direction to the streamlines, $R(s)$ represents the radius of curvature of the streamlines. Equation C-6 along this direction can be written as

$$\rho\frac{u^2(s)}{R(s)} = -\frac{\partial P}{\partial n} \tag{C-7}$$

This equation relates the radius of curvature of streamlines to the gradients of pressure normal to those streamlines. Considering different flow scenarios as shown in Figure C-2.

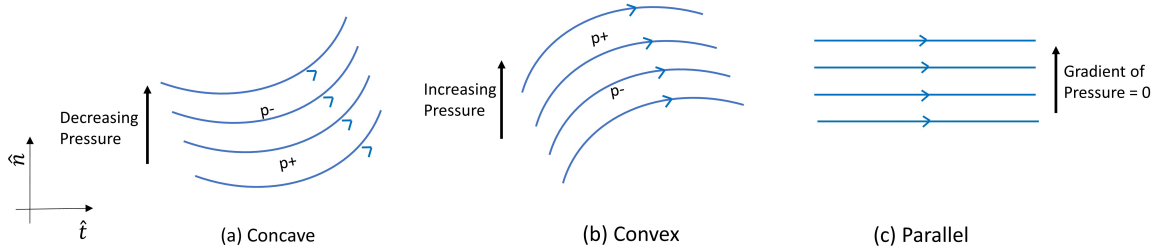

(a) Concave (b) Convex (c) Parallel

Figure C-2: Scenarios for streamlines curvature.

1. **Case A:** In this case the radius of curvature of streamlines is negative (concave) and hence the pressure decreases in the direction of positive $\hat{n}$.
2. **Case B:** Pressure increases in direction of positive $\hat{n}$ due to convex curving streamlines.
3. **Case C:** In this case the radius of curvature is infinity and hence the pressure at a given section is constant along $\hat{n}$.

In the case of parallel streamlines (Case C), the pressure is constant across (i.e. along $\hat{n}$) the streamlines and not along them. The only change in pressure along $\hat{n}$ in such situations is due to the body forces term gradient along that direction, such as hydrostatic pressure.

Appendix D

Fluent settings

The solver settings in ANSYS Fluent 2019R3 are listed in this Appendix.

1. **Solver**
   (a) Type: Pressure-based
   (b) Velocity type: Absolute
   (c) Time: Transient
2. **Models**
   (a) Multiphase: Volume of Fluid
      - Implicit Volume fraction formulation
      - Volume fraction cutoff: 1e -06
      - Interface modelling: Sharp/Dispersed
      - Phases: Air (primary phase) and Water (secondary phase)
   (b) Viscous Model: SST $k-\omega$ with curvature correction
3. **Materials**: Air and water with default properties at 20°C

Table D-1: Air and water properties at 20°C

	Air	**Water**
Phase	Primary	Secondary
Density (kg/m^3)	1.225	998.2
Viscosity (kg/ms)	1.79e-05	1.00e-03

4. **Cell Zone Conditions:**
   - Phase: Fluid (all volumes)

- Operating pressure: 101325 Pa
- Reference pressure location: Air inlet BC
- Operating Density[1]: 0 kg/m^3

5. **Boundary conditions:** explained in Sections 2-2 and 2-12.

6. **Solution methods:**

   - Pressure velocity coupling scheme: Coupled.
   - Spatial discretization:
     (a) Gradient: Least Squares Cell Based.
     (b) Pressure: PRESTO!
     (c) Momentum: Second Order Upwind.
     (d) Volume fraction: Compressive.
     (e) Turbulent kinetic energy: First Order Upwind.
     (f) Specific dissipation rate: First Order Upwind.
   - Transient Formulation: Bounded Second Order Implicit.

7. **Initialization:** Hybrid Initialization with all volumes patched with water initially.

8. **Monitors:**

   - Surface report:
     (a) Average static pressure at exit of *funnel* i.e. at Location I in Figure 2-5-3-1.
     (b) Average static pressure at exit of *extension* i.e. at Location II in Figure 2-5-3-1.
     (c) Area of air-water interface.
   - Flux report:
     (a) Net mass flow rate through *funnel*.
     (b) Net mass flow rate through the whole computational domain.
   - Volume report:
     (a) Average tangential velocity in *funnel*.
     (b) Average air to water volume ratio in *funnel*.
     (c) Average air to volume ratio in whole computational domain.

[1]Setting operating density to 0 is essential to include the effects of hydrostatic forces in the simulation.

Bibliography

[1] S. Mulligan, "Iron oxidation in groundwater using a hyperbolic water vortex system," *Graduation internship Environmental Sciences & Chemical Engineering, Van Hall Larenstein University of Applied Sciences*, April 2021.

[2] T. OpenCourseWare, "Aeration and gas stripping," *<https://ocw.tudelft.nl/wp-content/uploads/Aeration-and-gas-stripping-1.pdf>*.

[3] P. Pal, *Industrial water treatment process technology*. Butterworth-Heinemann, 2017.

[4] M. M. Benjamin and D. F. Lawler, *Water quality engineering: Physical/chemical treatment processes*. John Wiley & Sons, 2013.

[5] J. Sotelo, F. Beltran, F. Benitez, and J. Beltran-Heredia, "Henry's law constant for the ozone-water system," *Water Research*, vol. 23, no. 10, pp. 1239–1246, 1989.

[6] M. Kemp, "Leonardo da vinci's laboratory: studies in flow," *Nature*, vol. 571, no. 7765, pp. 322–324, 2019.

[7] R. D. Anderson, "Plug-hole vortex," CC BY-SA 3.0 <https://creativecommons.org/licenses/by-sa/3.0>.

[8] J. Schmaltz, "Tropical cyclone gillian," March 26, 2014 <https://visibleearth.nasa.gov/source/281/cyclones>.

[9] Hellbuny CC BY-SA 3.0 <https://commons.wikimedia.org/w/index.php?curid=3917656>.

[10] H. J. Lugt, "Vortex flow in nature and technology," *wi*, 1983.

[11] S. Mulligan, "Experimental and numerical analysis of three-dimensional free-surface turbulent vortex flows with strong circulation," *Ireland: Institute of Technology Sligo*, 2015.

[12] H. Rouse, "On the role of eddies in fluid motion," *American Scientist*, vol. 51, no. 3, pp. 274A–314, 1963.

[13] L. L. Daggett, G. H. Keulegan, *et al.*, "Similitude conditions in free-surface vortex formations," 1974.

[14] A. Škerlavaj, L. Škerget, J. Ravnik, and A. Lipej, "Predicting free-surface vortices with single-phase simulations," *Engineering Applications of Computational Fluid Mechanics*, vol. 8, no. 2, pp. 193–210, 2014.

[15] P. K. Dutta and A. K. Ray, "Experimental investigation of taylor vortex photocatalytic reactor for water purification," *Chemical Engineering Science*, vol. 59, no. 22-23, pp. 5249–5259, 2004.

[16] R. Ostilla-Mónico, E. P. Van Der Poel, R. Verzicco, S. Grossmann, and D. Lohse, "Boundary layer dynamics at the transition between the classical and the ultimate regime of taylor-couette flow," *Physics of fluids*, vol. 26, no. 1, p. 015114, 2014.

[17] S. Grossmann, D. Lohse, and C. Sun, "High–reynolds number taylor-couette turbulence," *Annual review of fluid mechanics*, vol. 48, 2016.

[18] J. H. Son, C. H. Sohn, and I. S. Park, "Numerical study of 3-d air core phenomenon during liquid draining," *Journal of Mechanical Science and Technology*, vol. 29, no. 10, pp. 4247–4257, 2015.

[19] S. Mulligan, G. De Cesare, J. Casserly, and R. Sherlock, "Understanding turbulent free-surface vortex flows using a taylor-couette flow analogy," *Scientific reports*, vol. 8, no. 1, pp. 1–14, 2018.

[20] V. Hernandez-Perez, M. Abdulkadir, and B. Azzopardi, "Grid generation issues in the cfd modelling of two-phase flow in a pipe," *The Journal of Computational Multiphase Flows*, vol. 3, no. 1, pp. 13–26, 2011.

[21] "Bericht iiber die voruntersuchnungen mit wendelrohren mit verschniedener wandform internal report," *Institut fur Gesundheitstechnik, Institute of Technology in Stuttgart, 1952.*

[22] J. Drewnowski, A. Remiszewska-Skwarek, S. Duda, and G. Łagód, "Aeration process in bioreactors as the main energy consumer in a wastewater treatment plant. review of solutions and methods of process optimization," *Processes*, vol. 7, no. 5, p. 311, 2019.

[23] A. Bennett, "Wastewater treatment: Bubbling up for major energy saving," *Filtr. Separat*, vol. 48, pp. 42–43, 2011.

[24] W. G. Whitman, "The two-film theory of gas absorption," *Chem. Metall. Eng.*, vol. 29, pp. 146–148, 1923.

[25] M. J. Berry, C. M. Taylor, W. King, Y.-M. Chew, and J. Wenk, "Modelling of ozone mass-transfer through non-porous membranes for water treatment," *Water*, vol. 9, no. 7, p. 452, 2017.

[26] L. Johansson, M. Ovesen, and C. Hallberg, *Self-organizing Flow Technology: In Viktor Schauberger's Footsteps.* Institutet för ekologisk teknik, 2002.

[27] B. T. Lubin and G. S. Springer, "The formation of a dip on the surface of a liquid draining from a tank," *Journal of Fluid Mechanics*, vol. 29, no. 2, pp. 385–390, 1967.

[28] G. Möller, "Vortex-induced air entrainment rates at intakes," *VAW, ETH Zürich, Switzerland, 2013.*

[29] A. Klimenko, "Evolution of vorticity in the bathtub vortex," 1998.

[30] A. Andersen, T. Bohr, B. Stenum, J. J. Rasmussen, and B. Lautrup, "The bathtub vortex in a rotating container," *Journal of Fluid Mechanics*, vol. 556, no. 1, pp. 121–146, 2006.

[31] J. Knauss, *Swirling flow problems at intakes.* Routledge, 2017.

[32] H. A. Einstein and H. Li, "Steady vortex flow in a real fluid," *Proc. Heat Transfer and Fluid Mechanics Institute, Stanford University*, pp. 33–43, 1951.

[33] M. Hall, "The structure of concentrated vortex cores," *Progress in Aerospace Sciences*, vol. 7, pp. 53–110, 1966.

[34] H. O. Anwar, "Flow in free vortex," *Water Power*, p. p. 153, Apr, 1965.

[35] K. Stewartson, "On almost rigid rotations," *Journal of Fluid Mechanics*, vol. 3, no. 1, pp. 17–26, 1957.

[36] M. Escudier, "Confined vortices in flow machinery," *Annual Review of Fluid Mechanics*, vol. 19, no. 1, pp. 27–52, 1987.

[37] B. Eckhardt, S. Grossmann, and D. Lohse, "Torque scaling in turbulent taylor-couette flow between independently rotating cylinders," *Journal of fluid mechanics*, vol. 581, p. 221, 2007.

[38] J. Strutt and L. Rayleigh, "On the instability of cylindrical fluid surfaces," *Phil. mag*, vol. 34, no. 5, pp. 177–180, 1892.

[39] G. I. Taylor, "Viii. stability of a viscous liquid contained between two rotating cylinders," *Philosophical Transactions of the Royal Society of London. Series A, Containing Papers of a Mathematical or Physical Character*, vol. 223, no. 605-615, pp. 289–343, 1923.

[40] M. Dunst, "An experimental and analytical investigation of angular momentum exchange in a rotating fluid," *Journal of Fluid Mechanics*, vol. 55, no. 2, pp. 301–310, 1972.

[41] A. INC, "Ansys fluent 18.2 user's manual," 2017.

[42] L. C. Ho, "Minimization of drainage time of filled pet bottle with initial rotation: A numerical study," *Master Thesis Report, Delft University of Technology* , 2020 <http://resolver.tudelft.nl/uuid:ea1e3c18-8844-42ed-81e2-b7fcef59d100>.

[43] R. L. Sorenson, "The 3dgrape book: Theory, users' manual, examples," 1989.

[44] Y. Fayolle, A. Cockx, S. Gillot, M. Roustan, and A. Héduit, "Oxygen transfer prediction in aeration tanks using cfd," *Chemical Engineering Science*, vol. 62, no. 24, pp. 7163–7171, 2007.

[45] M. Gresch, M. Armbruster, D. Braun, and W. Gujer, "Effects of aeration patterns on the flow field in wastewater aeration tanks," *Water research*, vol. 45, no. 2, pp. 810–818, 2011.

[46] F. Özkan, A. Wenka, E. Hansjosten, P. Pfeifer, and B. Kraushaar-Czarnetzki, "Numerical investigation of interfacial mass transfer in two phase flows using the vof method," *Engineering Applications of Computational Fluid Mechanics*, vol. 10, no. 1, pp. 100–110, 2016.

[47] F. Suerich-Gulick, S. Gaskin, M. Villeneuve, G. Holder, and E. Parkinson, "Experimental and numerical analysis of free surface vortices at a hydropower intake," 2006.

[48] H. Shabara, O. Yaakob, Y. M. Ahmed, and A. Elbatran, "Cfd simulation of water gravitation vortex pool flow for mini hydropower plants," *Jurnal Teknologi*, vol. 74, no. 5, 2015.

[49] U. Manual, "Ansys fluent 12.0," *Theory Guide*, 2009.

[50] S. B. Pope, "Turbulent flows," 2001.

[51] P. W. Egolf and K. Hutter, "Reynold's averaging of the navier–stokes equations (rans)," in *Nonlinear, Nonlocal and Fractional Turbulence*, pp. 13–18, Springer, 2020.

[52] J. Boussinesq, "Theorie de l'ecoulement tourbillant," *Mem. Acad. Sci.*, vol. 23, p. 46, 1877.

[53] Y. Chen, C. Wu, B. Wang, and M. Du, "Three-dimensional numerical simulation of vertical vortex at hydraulic intake," *Procedia Engineering*, vol. 28, pp. 55–60, 2012.

[54] V. Rajendran, S. Constantinescu, and V. Patel, "Experimental validation of numerical model of flow in pump-intake bays," *Journal of hydraulic Engineering*, vol. 125, no. 11, pp. 1119–1125, 1999.

[55] J. Hinze and M. Uberoi, "Turbulence," 1960.

[56] T. Tokyay and S. Constantinescu, "Validation of a large-eddy simulation model to simulate flow in pump intakes of realistic geometry," *Journal of hydraulic Engineering*, vol. 132, no. 12, pp. 1303–1315, 2006.

[57] M. Sussman and E. G. Puckett, "A coupled level set and volume-of-fluid method for computing 3d and axisymmetric incompressible two-phase flows," *Journal of computational physics*, vol. 162, no. 2, pp. 301–337, 2000.

[58] "Webplotdigitizer," *<https://automeris.io/WebPlotDigitizer/>*.

[59] W.-L. Chuang and S.-C. Hsiao, "Three-dimensional numerical simulation of intake model with cross flow," *Journal of Hydrodynamics*, vol. 23, no. 3, pp. 314–324, 2011.

[60] A. Škerlavaj, A. Lipej, J. Ravnik, and L. Škerget, "Turbulence model comparison for a surface vortex simulation," in *IOP Conference Series: Earth and Environmental Science*, vol. 12, p. 012034, IOP Publishing, 2010.

[61] NASA, "Langley research center turbulence modeling resource," <https://turbmodels.larc.nasa.gov/index.html>.

[62] B. E. Launder and B. I. Sharma, "Application of the energy-dissipation model of turbulence to the calculation of flow near a spinning disc," *Letters in heat and mass transfer*, vol. 1, no. 2, pp. 131–137, 1974.

[63] W. Rodi and G. Scheuerer, "Scrutinizing the k-epsilon-model under adverse pressure gradient conditions," in *4th Symposium on Turbulent Shear Flows*, pp. 2–8, 1984.

[64] D. C. Wilcox, "Comparison of two-equation turbulence models for boundary layers with pressure gradient," *AIAA journal*, vol. 31, no. 8, pp. 1414–1421, 1993.

[65] D. C. Wilcox *et al.*, *Turbulence modeling for CFD*, vol. 2. DCW industries La Canada, CA, 1998.

[66] J. C. Kok, "Resolving the dependence on freestream values for the k-turbulence model," *AIAA journal*, vol. 38, no. 7, pp. 1292–1295, 2000.

[67] F. R. Menter, "Two-equation eddy-viscosity turbulence models for engineering applications," *AIAA journal*, vol. 32, no. 8, pp. 1598–1605, 1994.

[68] P. Kundu, I. Cohen, G. Hu, and D. Dowling, "Fluid mechanics 6th ed., waltham, ma," 2015.